Guidance, Navigation, and Control for Munitions

A Thesis

Submitted to the Faculty

of

Drexel University

by

Mark Dean Ilg

in partial fulfilment of the

requirements for the degree

of

Doctor of Philosophy

May 2008

Dedications

To My Loving Wife Nicole

Acknowledgements

I would like to express my sincere gratitude to my advisor, Dr. Bor-Chin Chang, for his guidance, supervision, and mentorship, but most of all for seeing the potential in me.

I would also like to thank my parents, Joyce and Ken, for a lifetime of encouragement and support.

Thanks to my supervisor, David Lyon, and my colleagues at US Army Research Laboratory, Brad Davis, Rex Hall, Thomas Harkins, Dave Hepner, Ryan Letniak, James Maley, Brendan Patton, and Mike Wilson for their insight and assistance.

Finally, I would like to thank my wife, Nicole, for without her inspiration, I would never had finished. It is far too difficult to find the words to express my overwhelming gratitude to her.

Philadelphia, Pennsylvania   Mark Ilg
June 2008

Table of Contents

List of Figures

Abstract

The United States Army is currently looking for new methods of guiding munitions, which would allow the military to employ guided munitions in place of traditional munitions. This will give the US Army an edge on the battle field and also allow the use of munitions in areas where traditional mortars and artillery cannot be used, including dense urban environments where collateral damage is not acceptable.

In this thesis, an innovative approach to Guidance, Navigation, and Control (GN&C) is developed for a spinning projectile that utilizes a single axis canard actuation system. Utilizing the projectiles spin, the controller can provide a full range of aerodynamic forces, over the 360° of rotation, that provides maneuverability using only one actuator. This technique minimizes the need for multiple actuators and maintains the inherent aerodynamic stability provided by the spin.

The GN&C system design described in this thesis consists of a tracking regulator for sinusoidally oscillating the canard system, a nonlinear state estimator for attitude measurement, and a guidance law to guide the projectile to a target. By combining the three components, we can demonstrate a closed-loop guidance system that will hit a target accurately at distances normally not achieved by an unguided projectile.

Chapter 1: Introduction

1.1 History of Guided Weapons

Since the First World War, the United States has been pursuing advancements in weapon design in an effort to more accurately engage targets. Guidance Navigation and Control (GN&C) of missile systems has been the top priority, developed over many years on nearly an unlimited research budget. Several classes of weapons systems have emerged as a result of this extensive research, including Radio Controlled and Laser Guided missile applications. These systems have been used frequently and reliably by the United States Armed Forces.

While the research and technology of smart missiles has been progressive, the development of smart munitions, mainly artillery and mortars, is far behind. Most recently, interest in upgrading artillery for accuracy has led to the development of new programs within the Armed Forces. Driving the cause for artillery upgrade, instead of replacement, is the massive arsenal of "dumb" weapons. The stockpile of traditional munitions imposes a financial restriction on the military, so instead of creating totally new weapon platforms, the military has programs in place to make the "dumb" weapons systems "smart". The Precision Guidance Kit (PGK) and the Precision Guided Mortar Munition (PGMM) are two programs aimed at upgrading the exiting arsenal of artillery to smart systems.

After years of development, smart munitions have yet to be fielded due to their unreliability and extreme cost. In order for the Army to continue to use gun launched

munitions, a GN&C system for a smart round must be developed that is highly accurate, reliable, and low-cost.

1.2 Traditional Weapons Design

Missile systems utilize a closed-loop design for stability, while projectiles are designed with inherent open-loop stability. Typically, munitions are designed by engineers to operate in an open-loop fashion as a "dumb" round. Current open loop design has been utilized for many years, so attempting to redesign an entire projectile and gun system would be impractical. By utilizing current gun systems, and slightly modifying traditional projectiles, the development and integration of a smart projectile would not only economically advantageous but would allow for seamless integration into the current weapons arsenal.

The current open-loop munitions systems allow a field commander the ability to fire and hit a target with an acceptable level of error. If the target is missed on the first attempt, the commander can recalculate and hopefully hit the target on the second shot. Firing tables and software have been developed to provide the commander with a reasonably reliable tool to recalculate for the second shot. This scenario is typical, but has downsides; the first round gives away location, and allows the enemy a chance to retaliate or relocate. It also becomes costly since each round costs a few thousand dollars, increasing mission cost with each missed target.

Improvement of this system would require a "smart" round to not only minimize the error, but do so with a limited budget. The current system works in most instances with limited collateral damage, but still is not as accurate as commanders would like.

1.3   Design Considerations

The delay of with developing cost effective smart munitions, until now, was the result of many factors. They are the inability to find components which survive the gun launch high-g's, the high cost of Inertial Measurement Units (IMUs), and the lack of guidance controllers for artillery rounds. Recent advances in embedded computers and Micro-Electro-Mechanical Systems (MEMS) allow for low cost production of sensors and Digital Signal Processor (DSP) micro-processors which are much smaller than their predecessors. Mass production of those items keeps cost low. The real hurdle is survivability at high-g's. Fortunately, most devices produced today can survive the gun launch using "potting" techniques. This method, coupled with proper structural design, can produce a very reliable system.

For accurate control of an artillery shell, the dynamic model must be fully understood and created for each round that is to be controlled. In order to do this, parameter estimation techniques are used to create a non-linear dynamic model of the projectile. Once the model is obtained, a system must be designed to accurately guide the artillery round as it flies down range. The system should consist of, but is not limited to, a DSP microprocessor, an array of sensors, and an actuation system.

In order to develop a controller for accurately guiding a projectile, the system must be reliable and robust. The controller needs to be designed to account for system uncertainties, disturbances, and failures, such that the smart round does not cause more unintended damage than the dumb round. The constraints on the size, weight, power consumption, and cost of the control system also need to be considered in the design. To accurately estimate the states of the system, an estimator will be designed based on the available sensors and the dynamics model of the system.

Commercially available sensors include magnetometers, rate gyros, accelerometers, thermopiles, solar sensors, and Global Positioning System (GPS) modules. In addition to the above sensors, there are others, that can be utilized for the state estimation. For example, ground based radar and laser range finding devices can be used together with a telecommunication link to the projectile.

For any of the aforementioned sensors to be included in a viable solution, each must undergo a battery of testing to ensure reliability and survivability of the high-g environment. The process is complex and requires a multitude of checks and balances. Each sensor must be calibrated to ensure the accuracy of its measurements. The controller must be programmed to consider sensor nonlinearities including cross-axis effects, bias and offset errors, temperature and electrical drift.

The control system to be designed for munitions is more challenging than that for missiles, since it involves more complicated aerodynamics, more constraint on size, actuation, and cost, and therefore it requires more sophisticated control system design.

1.4 Relevant Work

Current advances in technology have brought a push by the Army to develop smart gun launched weapons. Several development programs in progress attempting are attempting to perform GN&C on a projectile. The Army PGK program utilizes an add-on kit that attaches to the fuse portion of a standard artillery shell to make the "dumb" artillery round smart. The technology used in this program is similar to that in Joint Direct Attack Munition (JDAM) of the United States Air Force. The Army PGMM project utilizes the existing dimensions of M395 artillery shell and gun system

to create a new smart weapon which can seamlessly be used in tactical applications when a smart round is needed. The PGMM round employs a thruster ring about the center of mass to provide its maneuver capability. One current projectile that has been field demonstrated is Excalibur. Excalibur is equipped with an IMU and four canards on the front of the projectile for guidance and flight control. This system has proved promising on the battlefield and is still in the test and evaluation stages.

The projectiles aforementioned are all far from being completed. Each projectile has its own inherent problems. PGK relies on GPS to measure roll orientation and de-spin its nose in order to perform guidance, thus any associated failure in the actuator system or if the GPS signal is jammed, the system may become unstable or uncontrollable. The PGMM round uses a Semi-Active Laser (SAL) seeker to provide target information. This requires a forward spotter for laser designation. PGMM's thrusters also minimize the amount of control authority the projectile has. The Excalibur relies on GPS and has costly IMU system, and very expensive canard actuation system. These high costs make the Excalibur impractical.

To determine the design path towards a GN&C system, extensive literature searches were performed through the journals and proceedings of the Institute of Electrical and Electronics Engineers (IEEE), American Institute of Aeronautics and Astronautics (AIAA), and Army technical reports. These searches turned up little information on projectile GN&C, but applications from missile theory, robotics, sensor signal processing, and space systems can be leveraged.

1.5 Contributions of the Thesis

In this thesis, an innovative approach is presented for the design of a GN&C system that can alter the flight path of a spinning projectile, from the standard ballistic trajectory, which will accurately engage a target. In other projectile guidance systems, the control system de-spins the projectile so it can be flown more like a missile, whereas my thesis addresses the possibility of guiding a projectile as it spins.

By maintaining the projectiles spin, the inherent stability that the spin provides is preserved, thus reducing the requirement that the controller must maintain aerodynamic stability. In order to provide guidance on the spinning projectile, canards placed towards the nose of the projectile would need to oscillate at the spin rate of the projectile. By varying the phase of the oscillation with respect to the projectiles roll angle, a force and moment is imposed on the projectiles body. Since the projectile does not have thrust, this force and moment from the canards are the only means the projectile has to modify the flight path.

With modern advances in microprocessors and sensors, the design of a complicated actuation and guidance system is feasible and practical for guidance of a spinning projectile. The GN&C system described in this thesis uses Multi-Variable Regulator Theory together with H_2 Control Theory to oscillate canards in a sinusoidal motion, an Extended Kalman Filter (EKF) for state estimation, and a guidance law to guide the projectile to a target. These topics can be realized utilizing aerodynamics analysis, nonlinear control theory, and robust control techniques. This thesis explains in detail the entire design cycle for a GN&C system for spinning munitions that includes the actuation system design, a method for determining the angular orientation estimation, and a guidance law for a projectile without thrust.

A regulator is necessary to control the canard system because under flight conditions, the canard system will undergo nonlinear aerodynamic loading as the projectile rotates and the amplitude and phase of the canard will be dynamically updated by the guidance laws. Therefore, aerodynamic theory is developed to provide the necessary background information for the effects of the canard on the body and the aerodynamic torques on the canard surface, so that when designed properly, the regulator can compensate for the undesired effects. The aerodynamic theory using a six degree-of-freedom (6DOF) dynamic model that is developed in this thesis for simulations and hardware in the loop testing.

To provide the regulator with a proper tracking signal, including the roll rate and roll angle of the projectile, an EKF is designed to estimated the attitude, or angular orientation, of the projectile in flight. Traditionally, an EKF design for a 6DOF system would use Euler Angle Notation for attitude estimations, however, in a spinning environment and the projectiles complex dynamics, the EKF will tend to diverge. In this thesis, I will demonstrate that by using quaternions rather than Euler angles in my EKF, the EKF will not diverge and will provide adequate attitude estimation.

The guidance system provides command signals, the phase and amplitude of the tracking signal, to the regulator. Typically in projectile guidance laws, Impact Point Predictors (IPP) are used to estimate where the projectile will impact and the guidance system will compensate for the error between the impact estimation and the target. In my thesis, I develop a new method Modified Proportional Navigation (MPN), which compensates for the projectiles lack of thrust and is more accurate than IPP.

1.6   Organization of the Thesis

The remainder of this thesis is organized as follows. Chapter 2 consists of the projectile aerodynamics background. This chapter will discuss the parameters, including those of canards, that will affect the forces and moments exerting on a projectile. A design and simulation model will be developed and used in the control system design, simulation and Hardware-in-the-Loop (HIL) experimentation for GN&C testing. In Chapter 3, a novel canard actuation and control system is proposed. The actuation and control system is evaluated in both simulation and experimentation via a HIL system that incorporates the flight dynamics of the projectile under test. Chapter 4 addresses the estimation of the projectile attitude, which is crucial in the Guidance, Navigation, and Control of the projectile. Magnetometers, rate gyroscopes, the theory for the quaternion, and the Extended Kalman Filter are employed in the estimation. In Chapter 5, two approaches for the guidance and control of a projectile are presented. One is the IPP approach and the other is the MPN approach. The conclusions and further research are summarized in Chapter 6.

Chapter 2: Flight Dynamics of Projectiles

An accurate flight dynamics model of the projectile is essential to the design of a controller that is both practical and possible. The dynamics of symmetric projectiles are well established, allowing the current dumb rounds to be quite accurate over long ranges in open-loop flight. The underlying dynamics of a projectile are highly non-linear and, to complicate matters, are dependant on numerous non-linear terms. The dynamic equations rely on the angle-of-attack, mach number, air pressure, etc. and the accuracy of the model can only be as good as the environmental model that is used. The following section describes the aerodynamic forces and moments on a projectile that will be used throughout this paper and used in simulations and hardware-in-the-loop experiments.

2.1 Coordinate System

First, a coordinate system must be developed for reference purposes. A typical system is defined as the North-East-Down (NED) coordinate system as described in the Ballistic Research Laboratory Report BRL-1216, [39]. Figure 2.1 shows the NED configuration as the base coordinate system described by x_i and the transformed axes $x_i^{'}$ of the projectile. Let the unit vector in each of the axes systems be described using e_i where $i \in \{1, 2, 3\}$. The NED describes the 1,2,3 sequence of the subscripts for the base coordinate system. Therefore, North is aligned with x_1, East is aligned with x_2,
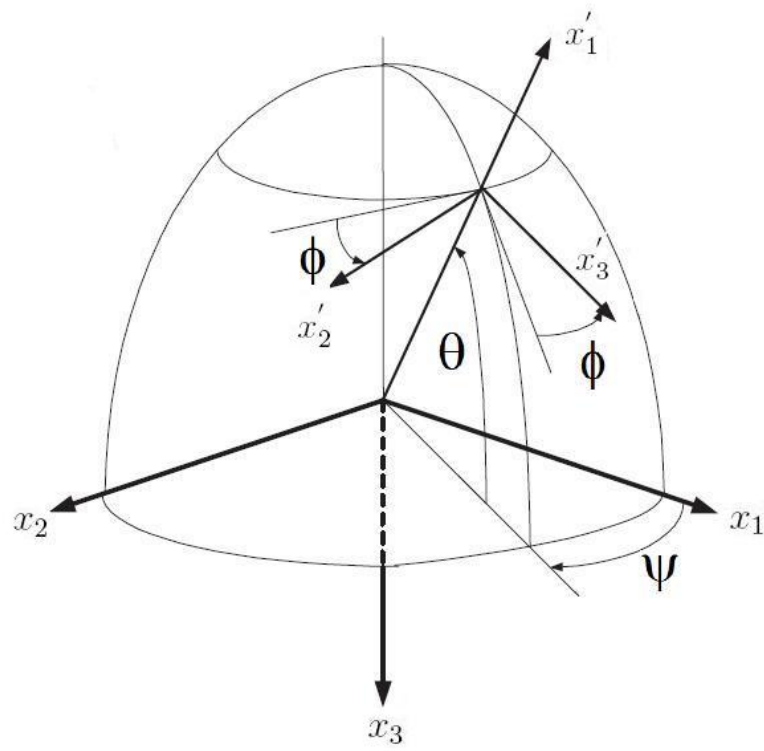
Figure 2.1: Coordinate System Definition

and Down, towards the center of the earth, is aligned with x_3. This typical configuration also can be referred in other texts using the i, j, k notation as in [39, 53].

For simplicity, the axes can be transformed by setting up the rotation matrices using matrix notation and/or tensor notation. The rotational matrix λ, defined as the Direction Cosine Matrix (DCM), describes the rotation from the one coordinate system to a new coordinate system.

$$\lambda = \begin{pmatrix} \lambda_{11} & \lambda_{12} & \lambda_{13} \\ \lambda_{21} & \lambda_{22} & \lambda_{23} \\ \lambda_{31} & \lambda_{32} & \lambda_{33} \end{pmatrix} \tag{2.1.1}$$

Where λ_{ij} represents the cosine of the angle between $x_i^{'}$ and x_j, and the axis transformation can be described by:

$$x_i^{'} = \sum_{j=1}^{3} \lambda_{ij} x_j, i = \{1, 2, 3\} \tag{2.1.2}$$

Which can also be written in matrix notation as

$$x^{'} = \lambda x \tag{2.1.3}$$

The inverse transformation can also be simply described by

$$x_i = \sum_{j=1}^{3} \lambda_{ji} x_j^{'}, i = \{1, 2, 3\} \tag{2.1.4}$$

The angular position of the body frame is represented by Euler angles, ψ, θ, and ϕ, which are the yaw, pitch, and roll angles respectively.

The Euler angles are defined based on a specific rotation sequence. This thesis will use the Yaw-Pitch-Roll (YPR) sequence, a common aerospace industry standard. The YPR sequence defines the rotation matrix, λ, which is obtained by sequentially rotating the body frame from its initial angular position, which is parallel to the earth
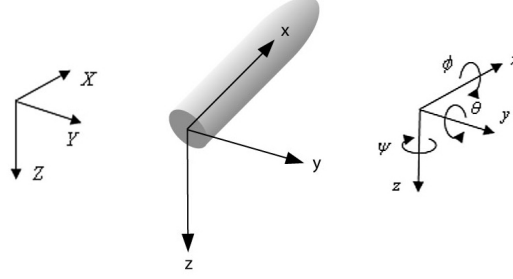
Figure 2.2: Body Fixed Rotations

frame, toward is actual angular position. The notation for the earth fixed and body fixed frames with the corresponding Euler rotations are shown in Figure 2.2, where, XYZ correlate to the NED coordinate system, xyz are the body fixed axis, and the Euler angles are ϕ, θ, ψ. The rotation matrices λ_ψ, λ_θ and λ_ϕ are given as:

$$\lambda_\psi = \begin{bmatrix} \cos\psi & \sin\psi & 0 \\ -\sin\psi & \cos\psi & 0 \\ 0 & 0 & 1 \end{bmatrix} \tag{2.1.5}$$

$$\lambda_\theta = \begin{bmatrix} \cos\theta & 0 & -\sin\theta \\ 0 & 1 & 0 \\ \sin\theta & 0 & \cos\theta \end{bmatrix} \tag{2.1.6}$$

$$\lambda_\phi = \begin{bmatrix} 1 & 0 & 0 \\ 0 & \cos\phi & \sin\phi \\ 0 & -\sin\phi & \cos\phi \end{bmatrix} \tag{2.1.7}$$

The rotation matrix, according to the YPR sequence, $\lambda_{\psi\theta\phi} = \lambda_\phi\lambda_\theta\lambda_\psi$ can be found as follows:

$$\lambda_{\psi\theta\phi} = \begin{bmatrix} \cos\theta\cos\psi & \cos\theta\sin\psi & -\sin\theta \\ \sin\phi\sin\theta\cos\psi - \cos\phi\sin\psi & \sin\phi\sin\theta\sin\psi + \cos\phi\cos\psi & \sin\phi\cos\theta \\ \cos\phi\sin\theta\cos\psi + \sin\phi\sin\psi & \cos\phi\sin\theta\sin\psi - \sin\phi\cos\psi & \cos\phi\cos\theta \end{bmatrix} \tag{2.1.8}$$

For the simplicity of presentation, the trigonometric functions are replaced with the following short-hand notations: $\cos(\bullet) = c_{\bullet}$ and $\sin(\bullet) = s_{\bullet}$, and hence Equation (2.1.8) becomes:

$$\lambda_{\psi\theta\phi} = \begin{bmatrix} c_\theta c_\psi & c_\theta s_\psi & -s_\theta \\ s_\phi s_\theta c_\psi - c_\phi s_\psi & s_\phi s_\theta s_\psi + c_\phi c_\psi & s_\phi c_\theta \\ c_\phi s_\theta c_\psi + s_\phi s_\psi & c_\phi s_\theta s_\psi - s_\phi c_\psi & c_\phi c_\theta \end{bmatrix} \tag{2.1.9}$$

2.2 Projectile Aerodynamics

In order to control a munition in flight, it is essential to have its flight dynamics model. Although the projectiles share similar basic aerodynamics principles as rockets and missiles, their flight dynamics are very different due to the lack of propulsion and the high roll rate. In the following sections, we will investigate the flight dynamics of the projectile and determine a state-space model, which will be used in the design of the control system.

Recall that Newton's second law of motion is:

$$\vec{F} = \frac{\partial \vec{p}}{\partial t} \tag{2.2.1}$$

where $\vec{F}$ is the force on the body and $\vec{p}$ is the momentum of the body. The mass, m, will be assumed constant, so Equation (2.2.1) can be simplified to Equation (2.2.2).

$$\vec{F} = m\frac{\partial \vec{v}}{\partial t} \tag{2.2.2}$$

In Figure 2.3, we are given two coordinate frames: the earth frame and the body frame of the projectile. Assume the vector is moving in the body frame, and the body frame is translating and rotating with respect to the earth frame. Then it can
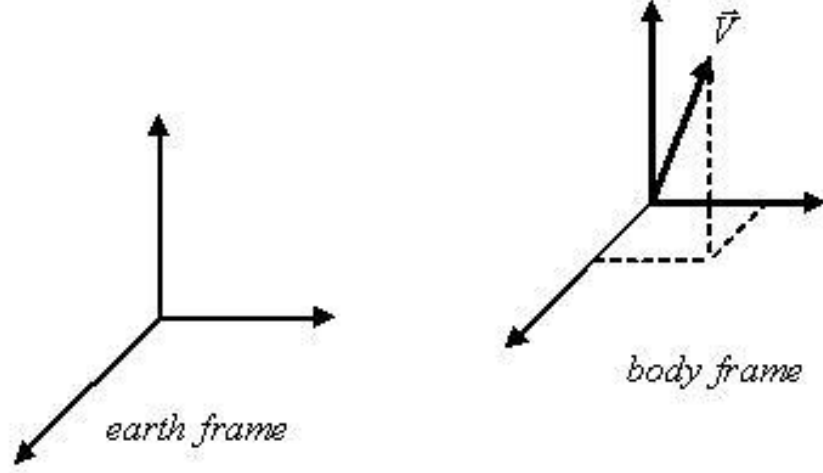
Figure 2.3: Frame Definitions

be found using the Equation of Coriolis [3]:

$$\left(\frac{d\vec{V}}{dt}\right)_e = \left(\frac{d\vec{V}}{dt}\right)_b + \vec{\omega} \times \vec{V} \tag{2.2.3}$$

where $\left(\frac{d\vec{V}}{dt}\right)_e$ and $\left(\frac{d\vec{V}}{dt}\right)_b$ are the time derivatives of $\vec{V}$ in the earth frame and the body frame respectively, and $\vec{\omega}$ is the angular velocity of the body frame with respect to the earth frame. Assume the vector, $\vec{V}$, is the velocity and the net force applied to the projectile is $\sum F_b$, then we have:

$$m\left(\frac{d\vec{V}}{dt}\right)_e = \sum F_b \tag{2.2.4}$$

and therefore,

$$\left(\frac{d\vec{V}}{dt}\right)_b = \frac{1}{m}\sum F_b - \vec{\omega} \times \vec{V} \tag{2.2.5}$$

where m is the mass of the projectile.

The velocity vector, $\vec{V}$, contains the following components $\vec{V} = \{u, v, w\}$ and the angular velocity, $\vec{\omega}$, in component form is $\vec{\omega} = \{p, q, r\}$. The vector definitions are
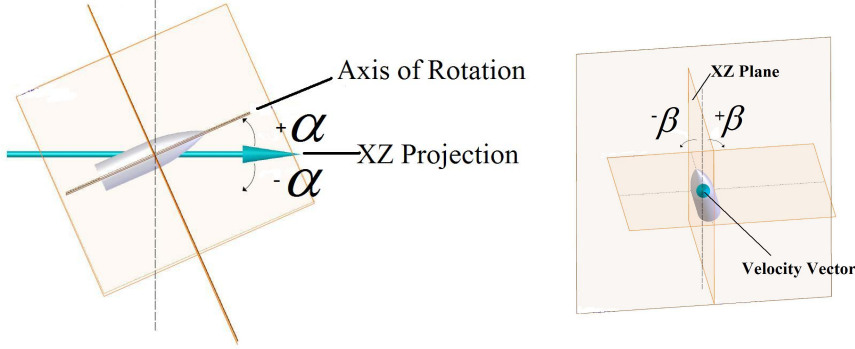
Figure 2.4: Alpha and Beta Definitions

used for compatibility with References [39, 53]. The notation $\left\|\vec{V}\right\| \equiv V$ for the total velocity will be used throughout this thesis. The Angle of Attack, α, as shown in the Figure 2.4, can be described as the angle between the velocity vector's xz projection and the axis of rotation of the body frame, which can be expressed in terms of the velocity components $\{u, v, w\}$:

$$\cos \alpha = \frac{\langle \{u, v, w\}, \{1, 0, 0\} \rangle}{|\{u, v, w\}||\{1, 0, 0\}|} = \frac{u}{\sqrt{u^2 + w^2}} \tag{2.2.6}$$

or,

$$\sin \alpha = \sqrt{1 - \left(\frac{u^2}{u^2 + w^2}\right)} = \frac{w}{\sqrt{u^2 + w^2}} \tag{2.2.7}$$

In the above equation, the sign of α is the same as w, i.e. $Sign[\alpha] = Sign[w]$.

Another term, Angle of Sideslip, β, is defined as the angle of the projection of the velocity vector's xz plane and the velocity vector, $\vec{V}$, and it can be expressed as a function of the velocity components, $\{u, v, w\}$:

$$\cos \beta = \frac{\langle \{u, v.w\}, \{u, 0, w\} \rangle}{|\{u, v, w\}| |\{u, 0, w\}|} = \frac{u^2 + w^2}{\sqrt{u^2 + v^2 + w^2}\sqrt{u^2 + w^2}} \approx \frac{\sqrt{u^2 + w^2}}{\left\|\vec{V}\right\|} \tag{2.2.8}$$

or,

$$\sin \beta = \frac{v}{\left\|\vec{V}\right\|} \tag{2.2.9}$$

In the above equation, the sign of β is the same as v, i.e. $Sign[\beta] = Sign[v]$. Another useful term is the complex yaw, which is defined as follows:

$$\xi = \frac{v + jw}{V} \tag{2.2.10}$$

Based on the equations of 2.2.6 and 2.2.9, it is straightforward to find the following equalities [3].

$$\frac{\vec{V}}{V} = \frac{\{u,v,w\}}{V} = \{\cos\alpha\cos\beta, \sin\beta, \sin\alpha\cos\beta\}$$
$$v = \cos\alpha\cos\beta$$
$$\xi = \sin\beta + j\sin\alpha\cos\beta \tag{2.2.11}$$
$$\delta_{cy} = |\xi| = \sqrt{\sin^2\beta + \sin^2\alpha\cos^2\beta}$$

where δ_{cy} is the magnitude of the complex yaw. Another common term, Total Angle of Attack, α_t, is defined as the angle between the velocity vector, $\vec{V}$, and the spin axis.

$$\cos\alpha_t = \frac{\langle\{u,v,w\},\{1,0,0\}\rangle}{|\{u,v,w\}|\,|\{1,0,0\}|} = \frac{u}{V} \tag{2.2.12}$$

This may also be defined as $\gamma \equiv \cos\alpha_t$ [3] The local Mach Number, M_a, is defined as the ratio of the velocity to the speed of sound, c_a, in the local medium: air.

$$M_a = \frac{\|V\|}{c_a} \tag{2.2.13}$$

The speed of sound varies with both temperature and humidity, but we will only consider temperature in our discussion as it is the dominant variable. The speed of sound can be defined by:

$$c_a = \sqrt{\kappa r_g T} \tag{2.2.14}$$

where r_g is the air gas constant, κ is the adiabatic index, and T is the absolute temperature.

The definitions above provide a mathematical simplicity for describing the motion of the projectile and correlate to the standard terms of aerodynamic theory. Later, in the following sections, we will further discuss their importance.

2.3 Body Forces

The forces acting on a projectile are mainly the normal forces and the axial forces (drag), however, in our discussions, we will include all the body forces. These forces are expressed in terms of the air density, velocity, projectile shape, and diameter and are described by the following equations. The coefficients are functions of both Mach number and angle of attack and are described in the Section 2.2.

$$\vec{F}_{xyz} = \vec{F}_{xyzaero} + \vec{F}_{xyzcanard} + \vec{F}_{xyzgravity} \qquad (2.3.1)$$

The net force, $\vec{F}_{xyz}$, is the summation of the forces acting on the projectile. $\vec{F}_{xyzcanard}$ is the canard force which varies with canard position, $\vec{F}_{xyzgravity}$ is the force of gravity, and $\vec{F}_{xyzaero}$ is the aerodynamic forces on the body. The three components of $\vec{F}_{xyzaero}$ along the body fixed x,y,z directions are given as follows:

$$
\begin{aligned}
F_{xyzaero} &= \{F_{xa}, F_{ya}, F_{za}\} \\
F_{xa} &= -\tfrac{1}{2}\rho V_w^2 A C_X \\
F_{ya} &= -\tfrac{1}{2}\rho V_w^2 A \left[-C_{Y0} - C_{Y\beta}\left(\tfrac{v_w}{V_w}\right) + \left(\tfrac{pd}{2V_w}\right) C_{Yp\alpha}\left(\tfrac{w_w}{V_w}\right) + C_{Y\gamma\alpha}\left(\tfrac{w_w}{V_w}\right) \right] \\
F_{za} &= -\tfrac{1}{2}\rho V_w^2 A \left[-C_{Z0} - C_{Z\alpha}\left(\tfrac{w_w}{V_w}\right) + \left(\tfrac{pd}{2V_w}\right) C_{Yp\alpha}\left(\tfrac{v_w}{V_w}\right) + C_{Y\delta\alpha}\left(\tfrac{v_w}{V_w}\right) \right]
\end{aligned}
\qquad (2.3.2)
$$

where the aerodynamic coefficients, $C_\bullet$, are described in Table 2.1 and they are functions of Mach number. The variable ρ is the air density and A is the reference area of the projectile, related to the reference diameter, d, by $A = \pi d^2/4$. The projectile velocity includes not only the projectile velocity, but also any external wind. The wind in the earth frame can be measured using a meteorological station and in vector

form is $\vec{V}_{wind_e} = \{u_{wind_e}, v_{wind_e}, w_{wind_e}\}$. The wind can be rotated to the body frame using:

$$V_{wind_b} = \lambda_{\psi\theta\phi} V_{wind_e} \tag{2.3.3}$$

where $\lambda_{\psi\theta\phi}$ is defined in Equation (2.1.8). The total velocity including wind is defined as $\vec{V}_w = \vec{V}_{wind_b} + \vec{V}$, or in component form, $V_w = \|\{u_w, v_w, w_w\}\|$. The subscript w is used for velocities that include the wind and shown in the above equations. The forces caused by the canards in the body frame are defined as follows:

$$
\begin{aligned}
\vec{F}_{xyzcanard} &= \{F_{x_c}, F_{y_c}, F_{z_c}\} \\
F_{x_c} &= -\tfrac{1}{2}\rho V_w^2 A C_{N\alpha\_canard} \sin\delta_c \sin\delta_C \\
F_{y_c} &= -\tfrac{1}{2}\rho V_w^2 A C_{N\alpha\_canard} \sin\delta_c \cos\delta_c \cos\phi \\
F_{z_c} &= -\tfrac{1}{2}\rho V_w^2 A C_{N\alpha\_canard} \sin\delta_c \sin\delta_c \sin\phi
\end{aligned}
\tag{2.3.4}
$$

where $\{F_{x_c}, F_{y_c}, F_{z_c}\}$ are the canard force components in the body frame provided by the control surfaces and δ_c is the deflection angle of the canards. Finally, the force due to gravity in the body frame is represented by:

$$\vec{F}_{xyzg} = \{F_{x_g}, F_{y_g}, F_{z_g}\} = \lambda_{\psi\theta\phi}\{0, 0, g\} \tag{2.3.5}$$

where, g is the gravity, which varies with altitude, and λ is the rotation matrix defined in section 2.1.

2.4 Moments

The moments exerted on the projectile can be broken into those due to the aerodynamic forces, the canards, and the center of gravity offset as follows:

$$\vec{M}_{ypr} = \vec{M}_{aero} + \vec{M}_{canard} + \vec{M}_{cgoffset} \tag{2.4.1}$$

where the three components of $\vec{M}_{aero}$ about the x,y,z axis are:

$$\vec{M}_{aero} = \{L_a, M_a, N_a\}$$
$$L_a = \tfrac{1}{2}\rho V_w^2 A d \left[\left(\tfrac{pd}{2V_w}\right) C_{lp} + C_l \right]$$
$$M_a = -\tfrac{1}{2}\rho V_w^2 A \left[C_{m0} + C_{m\alpha}\left(\tfrac{w_w}{V_w}\right) + \left(\tfrac{qd}{2V_w}\right) C_{mq} + \left(\tfrac{pd}{2V_w}\right) C_{np\alpha}\left(\tfrac{v_w}{V_w}\right) + (C_{n\gamma\alpha} + C_{n\alpha})\left(\tfrac{v_w}{V_w}\right) \right]$$
$$N_a = -\tfrac{1}{2}\rho V_w^2 A \left[C_{n0} + C_{n\beta}\left(\tfrac{v_w}{V_w}\right) + \left(\tfrac{rd}{2V_w}\right) C_{nr} + \left(\tfrac{pd}{2V_w}\right) C_{np\alpha}\left(\tfrac{w_w}{V_w}\right) + (C_{n\gamma\alpha} + C_{n\alpha})\left(\tfrac{w_w}{V_w}\right) \right]$$

$$(2.4.2)$$

The aerodynamic moments about the y,z axis due to the canards are described as follows:

$$\vec{M}_c = \{0, M_a, N_a\}$$
$$M_c = \tfrac{1}{2}\rho V_w^2 A F_{zc} \left(CG - CP_{can}\right) d \qquad (2.4.3)$$
$$N_c = -\tfrac{1}{2}\rho V_w^2 A F_{yc} \left(CG - CP_{can}\right) d$$

where CG is the center of gravity, and CP_{can} is the center of pressure of the canard.

The moments due to the center of gravity offset are given as:

$$\vec{M}_{cgoff} = \{L_{cgoff}, M_{cgoff}, N_{cgoff}\}$$
$$L_{cgoff} = \tfrac{1}{2}\rho V_w^2 A \left(C_{N\alpha} \sin \bar{\alpha} \left(CG_{offset} \sin \phi_{cg} \cos \phi' - CG_{offset} \cos \phi_{cg} \sin \phi'\right)\right)$$
$$-C_{m\alpha}\left(r CG_{offset} \sin \phi_{cg} + q CG_{offset} \cos \phi_{cg}\right) \tfrac{d}{V_w}$$
$$M_{cgoff} = \tfrac{1}{2}\rho V_w^2 A C_X CG_{offset} \cos \phi_{offset}$$
$$N_{cgoff} = -\tfrac{1}{2}\rho V_w^2 A C_X CG_{offset} \sin \phi_{offset}$$

$$(2.4.4)$$

where $\phi' = \tan^{-1}\left(\tfrac{v_w}{w_w}\right)$ and $\sin^2 \bar{\alpha} = \tfrac{u_w^2 + v_w^2}{V_w^2}$. For all practical applications, we assume the moment due to CG offset is approximately zero.

Table 2.1: Aerodynamic Coefficient Descriptions

Coefficient	Description
$C_X = C_{X0} + C_{X\alpha_2}\epsilon^2 + C_{X\alpha_4}\epsilon^4$	Body Axial Force Coefficient
$C_{Z\alpha} = C_{Z\alpha 0} + C_{N\alpha_3}\epsilon^2 + C_{Z\gamma\alpha\beta}\epsilon^2\cos{(N\phi')}$	Normal Force Coefficient in the Z direction w/ Rear Fins
$C_{Y\beta} = C_{Y\beta 0} + C_{N\alpha_3}\epsilon^2 + C_{Z\gamma\alpha\beta}\epsilon^2\cos{(N\phi')}$	Normal Force Coefficient in the Y direction w/ Rear Fins
$C_{Yp\alpha}$	Magnus Force Coefficient in Y Direction due to AOA
$C_{Zp\beta}$	Magnus Force Coefficient in Y Direction due to Sideslip
C_{lp}	Roll Damping Coefficient
$C_l = C_{l\delta}\delta + C_{l\gamma\bar{\alpha}_2}\epsilon^2\sin{(N\phi')}$	Roll Torque Moment Coefficient
$C_{m\alpha} = C_{m\alpha 0} + C_{m\alpha_3}\epsilon^2 + C_{m\alpha_5}\epsilon^4 + C_{m\gamma\alpha_3}\epsilon^2\cos{(N\phi')}$	Pitching Moment Coefficient
$C_{n\beta} = C_{n\beta 0} + C_{m\alpha_3}\epsilon^2 + C_{m\alpha_5}\epsilon^4 + C_{m\gamma\alpha_3}\epsilon^2\cos{(N\phi')}$	Yawing Moment Coefficient
$C_{mq} = C_{mq0} + C_{mq\alpha_2}\epsilon^2$	Pitch Damping Moment Coefficient
$C_{nr} = C_{nq0} + C_{nq\alpha_2}\epsilon^2$	Yaw Damping Moment Coefficient
$C_{n\gamma\alpha} = C_{n\gamma\alpha_3}\epsilon^2\sin{(N\phi')}$	Combined AOA and Roll Moment Coefficient due to Fins
$C_{Y\gamma\alpha} = C_{Y\gamma\alpha_3}\epsilon^2\sin{(N\phi')}$	Combined AOA and Roll Force Coefficient due to Fins
$C_{n\alpha}$	Side Moment Coefficient
$C_{np\alpha}$	Magnus Moment Coefficient due to AOA
$C_{np\beta}$	Magnus Moment Coefficient due to Sideslip
$C_{N\alpha canard}$	Canard Normal Force Coefficient
$C_{y0}, C_{z0}, C_{m0}, C_{no} = 0$	Force and Moment Coefficient due to Trim

Note: $\epsilon = \cos\alpha$ and N is the number of rear fins.

2.5   State-Space Model

Now that we have described how the forces and moments relate to the aerodynamics and the control surfaces, it is straightforward to determine the state equations for the system. The state equations comprise the forces, moments, and rigid body dynamics equations. Utilizing Equation (2.2.5), it is straightforward to derive the following equation:

$$
\begin{bmatrix} \dot{u} \\ \dot{v} \\ \dot{w} \end{bmatrix} = \frac{1}{m} \begin{bmatrix} F_x \\ F_y \\ F_z \end{bmatrix} - \{p, q, r\} \times \{u, v, w\} = \frac{1}{m} \begin{bmatrix} F_x \\ F_y \\ F_z \end{bmatrix} - \begin{bmatrix} 0 & -r & q \\ r & 0 & -p \\ -q & p & 0 \end{bmatrix} \begin{bmatrix} u \\ v \\ w \end{bmatrix}
$$

$$(2.5.1)$$

where $\{F_x, F_y, F_z\}$ are the components of the force vector, $\vec{F}_{xyz}$, along the x,y,z directions as described in Section 2.3. With $\vec{V}$ replaced by the angular momentum $H = I\omega$, Equation (2.2.3) becomes:

$$
\left(\frac{dI\vec{\omega}}{dt} \right)_e = \left(\frac{dI\vec{\omega}}{dt} \right)_b + \vec{\omega} \times I\vec{\omega} \tag{2.5.2}
$$

Since,

$$
\left(\frac{dI\vec{\omega}}{dt} \right)_e = M_{ypr} \tag{2.5.3}
$$

we have:

$$
I \left(\frac{d\vec{\omega}}{dt} \right)_b = M_{ypr} - \vec{\omega} \times I\vec{\omega} \tag{2.5.4}
$$

The inertia matrix, I, in the above equations is described by the following equation:

$$
I = \begin{bmatrix} I_{xx} & -I_{xy} & -I_{xz} \\ -I_{yx} & I_{yy} & -I_{yz} \\ -I_{zx} & -I_{zy} & I_{zz} \end{bmatrix} = \begin{bmatrix} I_{xx} & 0 & 0 \\ 0 & I_{yy} & 0 \\ 0 & 0 & I_{yy} \end{bmatrix} \tag{2.5.5}
$$

The $I_{yy} = I_{zz}$ simplification of the inertia matrix can be made because the projectile is symmetric about the axis of rotation. Then from, Equation (2.5.4) we have the

following:

$$\begin{bmatrix} \dot{p} \\ \dot{q} \\ \dot{r} \end{bmatrix} = \begin{bmatrix} \frac{L}{I_{xx}} \\ \frac{M}{I_{yy}} + (I_{xx} - I_{yy})\, pr \\ \frac{N}{I_{yy}} + (I_{yy} - I_{xx})\, pq \end{bmatrix} \tag{2.5.6}$$

Where $\{L, M, N\}$ are the components of the moment, $\vec{M}_{ypr}$, about the x, y and z axes. The aerospace sequence, YPR, is used to relate rate of change of the Euler angles to the body fixed angular rates in Equation (2.5.7).

$$\begin{bmatrix} p \\ q \\ r \end{bmatrix} = \begin{bmatrix} \dot{\phi} \\ 0 \\ 0 \end{bmatrix} + \begin{bmatrix} 1 & 0 & 0 \\ 0 & c_\phi & s_\phi \\ 0 & -s_\phi & c_\phi \end{bmatrix} \left(\begin{bmatrix} 0 \\ \dot{\theta} \\ 0 \end{bmatrix} + \begin{bmatrix} c_\theta & 0 & -s_\theta \\ 0 & 1 & 0 \\ s_\theta & 0 & c_\theta \end{bmatrix} \begin{bmatrix} 0 \\ 0 \\ \dot{\psi} \end{bmatrix} \right)$$
$$= \begin{bmatrix} 1 & 0 & s_\theta \\ 0 & c_\phi & c_\theta s_\phi \\ 0 & -s_\phi & c_\theta c_\psi \end{bmatrix} \begin{bmatrix} \dot{\phi} \\ \dot{\theta} \\ \dot{\psi} \end{bmatrix} \tag{2.5.7}$$

and by inverting the equations, an equation for the rate of change of the Euler angles is found to be:

$$\begin{bmatrix} \dot{\phi} \\ \dot{\theta} \\ \dot{\psi} \end{bmatrix} = \begin{bmatrix} 1 & -s_\phi t_\theta & -c_\phi t_\theta \\ 0 & c_\phi & -s_\phi \\ 0 & \frac{s_\phi}{c_\theta} & \frac{c_\phi}{c_\theta} \end{bmatrix} \begin{bmatrix} p \\ q \\ r \end{bmatrix} \tag{2.5.8}$$

We will define the remaining states as the earth based location of the projectile, X_e, Y_e, Z_e. The rate of change of the position states can be described by rotating the body fixed velocities according to the aerospace sequence back to the earth frame as shown in Equation (2.5.9).

$$\begin{bmatrix} \dot{X}_e \\ \dot{Y}_e \\ \dot{Z}_e \end{bmatrix} = \lambda_{\psi\theta\phi}^{-1} \begin{bmatrix} u \\ v \\ w \end{bmatrix} \tag{2.5.9}$$

The state vector is defined as $x = \{u, v, w, p, q, r, \phi, \theta, \psi, X_e, Y_e, Z_e\}$ and the state equations can be summarized in:

$$
\begin{aligned}
\dot{x}_1 &= \frac{Fx}{m} + x_6 x_2 - x_5 x_3 \\
\dot{x}_2 &= \frac{Fy}{m} - x_6 x_1 + x_4 x_3 \\
\dot{x}_3 &= \frac{Fz}{m} - x_5 x_1 - x_4 x_2 \\
\dot{x}_4 &= \frac{L}{I_{xx}} \\
\dot{x}_5 &= \frac{M}{I_{yy}} + (I_{xx} - I_{yy}) x_4 x_6 \\
\dot{x}_6 &= \frac{N}{I_{yy}} + (I_{yy} - I_{xx}) x_4 x_5 \\
\dot{x}_7 &= x_4 - s_{x_8} t_{x_8} x_5 - c_{x_7} t_{x_8} x_6 \\
\dot{x}_8 &= c_{x_7} x_5 - s_{x_8} x_6 \\
\dot{x}_9 &= \frac{c_{x_7}}{c_{x_8}} x_5 + \frac{c_{x_7}}{c_{x_8}} x_6 \\
\dot{x}_{10} &= c_{x_8} c_{x_9} x_1 + c_{x_8} s_{x_9} x_2 - s_{x_8} x_3 \\
\dot{x}_{11} &= (s_{x_7} s_{x_8} c_{x_9} - c_{x_7} s_{x_9}) x_1 + (s_{x_7} s_{x_8} s_{x_9} - c_{x_7} c_{x_9}) x_2 + s_{x_7} c_{x_8} x_3 \\
\dot{x}_{12} &= (c_{x_7} s_{x_8} c_{x_9} - c_{x_7} s_{x_9}) x_1 + (c_{x_7} s_{x_8} s_{x_9} - s_{x_7} c_{x_9}) x_2 + c_{x_7} c_{x_8} x_3
\end{aligned}
\tag{2.5.10}
$$

Now that a model has been developed for the system, the system is simulated using Mathworks^{TM} Simulink®. For reference, the following plots have been assembled to show the typical open loop response of the system using the Simulink® [1] 6DOF model. The simulation utilizes the ode23 solver with maximum step size of 2s. The initial conditions are

$$
\begin{aligned}
x0 &= \{u0, v0, w0, p0, q0, r0, \phi0, \theta0, \psi0, X0, Y0, Z0\} \\
&= \{300, 0, 0, 0.0001, 0, 0, 0, -0.3491, 0.0000, 0, 0, 0, 0\}
\end{aligned}
\tag{2.5.11}
$$

Where, $\vec{V}$ is measured in $\frac{m}{s}$, $\vec{\omega}$ is measured in $\frac{rad}{s}$, the Euler angles, $\{\phi, \theta, \psi\}$, are measured in radians, and position, X_e, Y_e, Z_e is measured in meters.

The initial conditions vector contains the gun information and the charge, or amount of explosive, for the projectile. we can see from the aforementioned initial

---

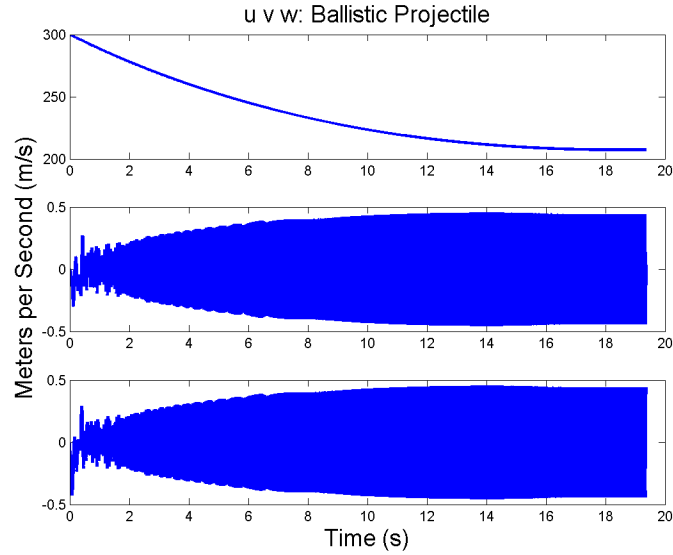[1]Simulink ® is a Registered Trademark of Mathworks^{TM}, Inc.

Figure 2.5: Velocity of Projectile in Ballistic Flight

conditions, the projectile is fired at 300m/s initial velocity, a small initial spin rate of 1e-4 rad/s, and a gun elevation of approximately -20 deg in the North-East-Down coordinate frame. In standard ballistic terms, the gun elevation would have a +20 degree Quadrant Elevation, QE, to correspond to the -20deg $\theta 0$ initial condition. The following Assumptions are made for simulation purposes: no tip-off (gun effect on projectile's initial rates) or wind in this simulation. The simulation terminates when the projectile impacts the ground. The estimated flight time for the given initial conditions and gun orientation is ≈ 19 seconds.

Figure 2.5 shows the body fixed velocities of the projectile as it flies through the air. The plot shows that the dominant velocity is in the axial direction as one would expect. The plot also shows that the velocity of the projectile will slow down with drag as time progresses. The velocities, v and w will vary slightly as the projectile flies due to the small coning motion of the projectile. Figure 2.6 shows the body fixed angular
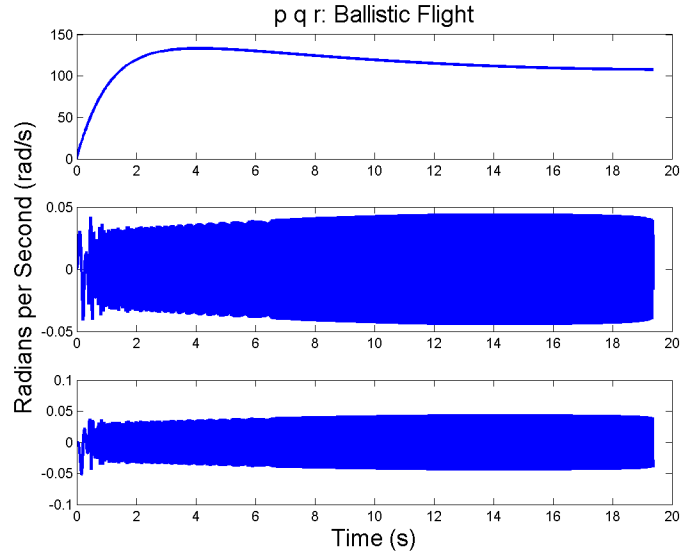
Figure 2.6: Angular Rates of Projectile in Ballistic Flight

rates for the projectile. The roll rate, p, will increase when the projectile comes out of the gun. This roll rate increase is due to the tail fins on the projectile, inducing a roll moment. The maximum spin rate is a design parameter chosen by the aerodynamic engineer to remove instability and to maintain a spin frequency well above the yawing frequency. The larger spin rate ensures that the system does not enter a yaw-spin lock. The yaw-spin lock causes the system to become aerodynamically unstable when the spin frequency and the yaw frequency are the same. The plots show the maximum spin rate of $\approx 133\frac{rad}{s}$ or $\approx 21Hz$ is achieved. Not only are the pitching and yawing rates less than the spin rate, they are very minimal. This is a good design since the system will not have any added drag due to high coning motion. Figure 2.7 shows the Euler angles of the projectile. The unwrapped roll angle, ϕ, is always increasing, the pitch angle, θ, varies from $\pm 20\deg$ and the variation in the yaw angle, ψ, is relatively small. The projectile's position is shown in Figure 2.8. The down range
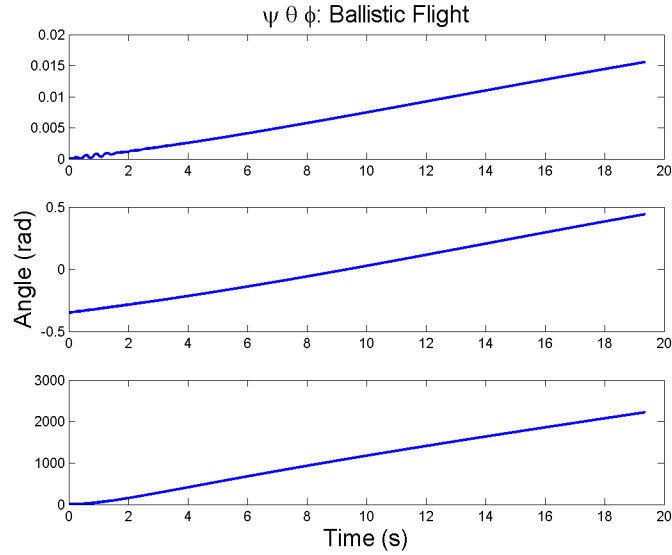
Figure 2.7: Euler Angles of Projectile in Ballistic Flight

position, X_e, shows an impact $\approx 4.4Km$ from the gun. The cross range, Y_e shows the impact at $\approx 23m$ to the left of the gun's pointing axis. The overall altitude of the projectile, Z_e, can be seen in the Z_e plot. The maximum altitude of $\approx 460m$ is seen in the projectile as it flies its' parabolic trajectory. It is important to ensure that the round will be stable. One measure of stability is a plot of α vs. β. The limit cycle behavior in Figure 2.9 shows where the system slightly oscillates with a small pitch/yaw rate through the flight with a maximum angle of $\leq 2e^{-3}$ degrees for both α and β. Typically, the α vs. β plot will be rounder, the octagonal shape is due to the solver step size and would become more circular as the step size decreased. The plot allows us to assume that the projectile is open loop stable and will maintain a prescribed flight path in ideal environmental conditions.
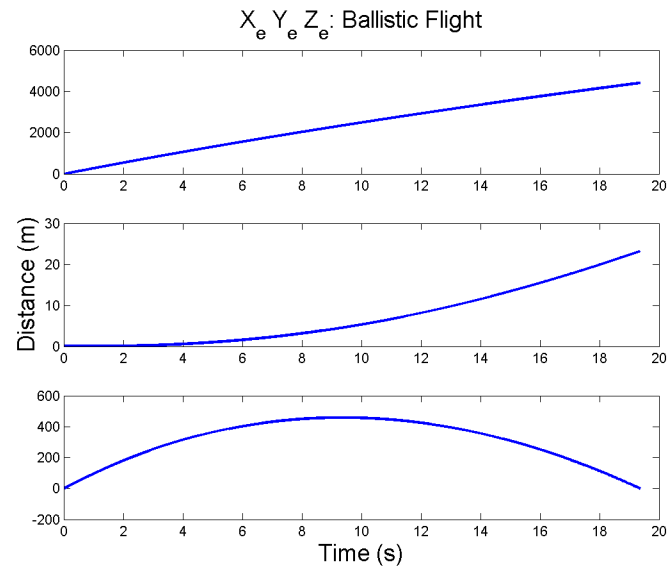
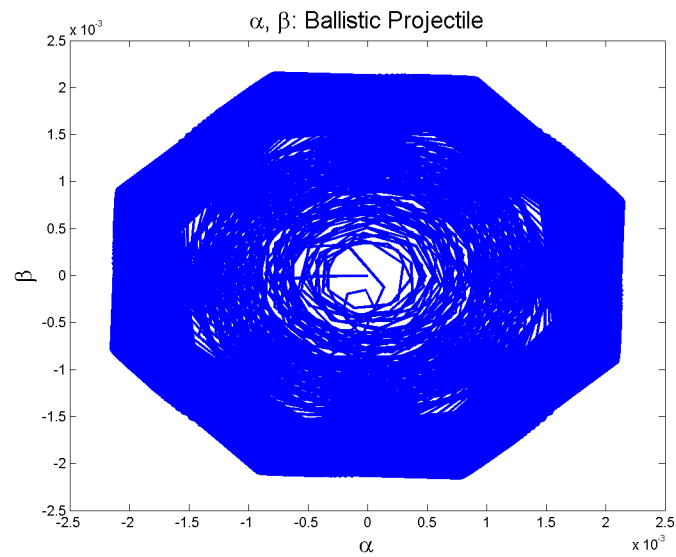Figure 2.8: Coordinates of Projectile in Ballistic Flight

Figure 2.9: Coordinates of Projectile in Ballistic Flight

Chapter 3: Canard Control Surfaces

To control the flight of a projectile using canards, a controller must be designed so that the canards can accommodate the sinusoidal disturbances caused by the spin of the projectile. The sinusoidal modulation allows the controller to give a net force via the canards in the body fixed yz plane. In order to provide this force in a desired direction, the frequency of the canard motion must match the frequency of the spin of the projectile. A regulator system will be designed to track a sinusoidal signal as is described in the following sections.

3.1 Multivariable Tracking Regulator and H_2 Control Design

The tracking signal is described in Equation (3.1.1) where a_r, the deflection of the canard, is related to the magnitude of the flight-path change, ω_r is the frequency, and ϕ_r is determined by both the pases of the spinning projectile and the direction of flight path change.

$$\bar{y}(t) = a_r sin(\omega_r t + \phi_r) \tag{3.1.1}$$

Utilizing Reference [6], the control problem can be defined as a regulator problem. The plant of the canard system can be represented by the following state-space equations:

$$\begin{aligned} \dot{x} &= A_p x + B_{p1} u_p + B_{p2} w_p + E_p \omega \\ y &= C_p x + F_p \omega + v_p \end{aligned} \tag{3.1.2}$$

where x represents the states of the plant model, u_p is the control input to the plant system, w_p is disturbance, ω represents the states of a system that generates the

sinusoidal tracking signal, and v_p is the measurement noise. We will assume that the noise, w_p, v_p, is white with the following covariance.

$$E(w_p w_p^T) = Q_p, \; E(w_p w_p^T) = R_p, \; E(w_p v_p^T) = N_p \qquad (3.1.3)$$

The sinusoidal tracking signal, ω_t can be considered as the output generated by the following system:

$$\dot{\omega}_t = A_r \omega_t + B_{r1} u_r + B_{r2} w_r$$
$$\bar{y} = C_r \omega_t + v_r \qquad (3.1.4)$$

where ω_t is the state vector of the system that generates sinusoidal signal, u_r is the reference signal input, assumed to be an impulse, and both w_r and v_r are white noises.

It is assumed that (A_p, B_{p1}) is controllable, (A_p, C_p) is observable, and B_{p1} and C_p are of full rank. It is also assumed that the composite pair as defined by Equation (3.1.5) is detectable.

$$\left\{ [C_p \; (F_p - C_r)], \begin{bmatrix} A_p & E_p \\ U & A_r \end{bmatrix} \right\} \qquad (3.1.5)$$

Another necessary condition for the existence of a solution to the regulator problem, described in References [6, 33], is that a unique solution exists to the relations described by:

$$A_p W - W A_r + B_{p1} U = -E_p$$
$$C_p W = F_p - C_r \qquad (3.1.6)$$

The composite system can now be defined as:

$$
\begin{bmatrix} \dot{x}_1 \\ \dot{x}_2 \\ \dot{\omega}_{t_1} \\ \dot{\omega}_{t_2} \end{bmatrix} = \begin{bmatrix} A_p & 0 \\ 0 & A_r \end{bmatrix} \begin{bmatrix} x_1 \\ x_2 \\ \omega_{t_1} \\ \omega_{t_2} \end{bmatrix} + \begin{bmatrix} B_{p1} \\ 0 \end{bmatrix} u_r + \begin{bmatrix} B_{p2} & 0 \\ 0 & B_{r2} \end{bmatrix} \begin{bmatrix} w_p & w_r \end{bmatrix}
$$

$$
y_c = \begin{bmatrix} C_p & 0 \\ 0 & C_r \end{bmatrix} \begin{bmatrix} x_1 \\ x_2 \\ \omega_{t_1} \\ \omega_{t_2} \end{bmatrix} + \begin{bmatrix} 1 & 0 \\ 0 & 1 \end{bmatrix} \begin{bmatrix} v_p & v_r \end{bmatrix}
$$

(3.1.7)

For this particular system that the following matrices are assumed to be zero, E_p and F_p. For ease of notation, Equation (3.1.7) is rewritten in the following:

$$
\dot{x}_c = A_c x_c + B_c u_r + E_c w
$$
$$
y_c = C_c x_c + Iv
$$

(3.1.8)

The composite state vector is composed of the system states and tracking signal states, $x_c = \begin{bmatrix} x_1 & x_2 & \omega_{t_1} & \omega_{t_2} \end{bmatrix}$, the input noise is now composed of the plant model noise and the reference signal noise, $w = \begin{bmatrix} w_p & w_r \end{bmatrix}$, the combined measurement noise, $v = \begin{bmatrix} v_p & v_r \end{bmatrix}$, and the output vector is comprised of the measured plant output and the measured noise output, $y_c = \begin{bmatrix} y & \bar{y} \end{bmatrix}$. The identity matrix notation, I, in Equation (3.1.8) will be used further for identity matrices.

The error of the system, z, is defined as the difference between the output, y, and the tracking signal, $\bar{y}$, or $z = \bar{y} - y$.

$$
z = \begin{bmatrix} z_1 \\ z_2 \end{bmatrix} = \begin{bmatrix} C_r \omega_t - y \\ W_i u_p \end{bmatrix} = \begin{bmatrix} -C_p \\ 0 \end{bmatrix} x + \begin{bmatrix} C_r \\ 0 \end{bmatrix} \omega_t + \begin{bmatrix} 0 \\ W_i \end{bmatrix} u_p
$$

(3.1.9)

Where, W_i, is the control input constraint on the system. Defining new variables to incorporate the disturbance into the plant yields $\bar{x} = x - W\omega_t$ and $\bar{u}_p = u_p -$

$U\omega_t$. Substituting these equations into Equation (3.1.9), we have the following for z_1

becomes:

$$\begin{aligned} z_1 &= -C_p(\bar{x} + W\omega_t) + C_r\omega_t \\ z_1 &= -C_p\bar{x} + (C_r - C_pW)\omega_t \end{aligned} \quad (3.1.10)$$

Substituting Equation (3.1.6) into Equation (3.1.10), we can conclude $z_1 = -C_p\bar{x}$. $\bar{x}$

is defined in in Equation (3.1.12). The error vector, z is written:

$$z = \begin{bmatrix} z_1 \\ z_2 \end{bmatrix} \begin{bmatrix} -C_p \\ 0 \end{bmatrix} \bar{x} + \begin{bmatrix} 0 \\ W_i \end{bmatrix} u_p \quad (3.1.11)$$

$$\begin{aligned} \dot{\bar{x}} &= \dot{x} - W\dot{\omega}_t \\ &= A_px + B_{p1}u_p + B_{p2}w_p + E_p\omega_t - W(A_r\omega_t + B_{r1}u_r + B_{r2}w_r) \\ &= A_p\bar{x} + (A_pW + E_p - WA_r + B_{p1}U)\omega_t + B_{p1}\bar{u}_p + B_{p2}w_p - W(B_{r1}u_r + B_{r2}w_r) \end{aligned}$$
$$(3.1.12)$$

Substituting Equation (3.1.6) into Equation (3.1.12):

$$\begin{aligned} \dot{\bar{x}} &= A_p\bar{x} + (A_pW + E_p - WA_r + B_{p1}U)\omega_t + B_{p1}\bar{u}_p + B_{p2}w_p - W(B_{r1}u_r + B_{r2}w_r) \\ \dot{\bar{x}} &= A_p\bar{x} + B_{p1}\bar{u}_p + B_{p2}w_p - W(B_{r1}u_r + B_{r2}w_r) \end{aligned}$$
$$(3.1.13)$$

The composite noise is assumed to be white gaussian with the following covariance

matrices

$$E(w_rw_r^T) = Q, E(v_rv_r^T) = V, E(w_rv_r^2) = N_0 \quad (3.1.14)$$

Therefore, an observer can be defined to minimize the steady state covariance

$$\lim_{t\to\infty} E(\{x - \hat{x}\}\{x - \hat{x}\}^T) \quad (3.1.15)$$

The observer is designed as follows:

$$\dot{\hat{x}} = [A_c - LC_c]\hat{x} + E_c\omega_t + Ly \quad (3.1.16)$$

where the composite observer gain L is:

$$L = YC_c^TV^{-1} \quad (3.1.17)$$

and Y is the positive semi-definite solution of the following Ricatti Equation.

$$(A_c-E_cN_0V^{-1}C_c)Y+Y(A_c-E_cN_0V^{-1}C_c)^T-YC_c^TV^{-1}C_c^TV^{-1}C_cY+E(I-NV^{-1}N^T)E^T = 0$$

$$(3.1.18)$$

Next, the state feedback gain, F, can be found using multivariable regulator design. From the error defined in Equation (3.1.11):

$$Q = (-Cp)^T(-Cp), R = W_i^TW_i \qquad (3.1.19)$$

$$F = -R^{-1}B_pX \qquad (3.1.20)$$

where X is a positive semi-definite stabilizing solution of the Algebraic Ricatti Equation (ARE):

$$A_p^TX + XA - XB_pR^{-1}B_p^TX + Q = 0 \qquad (3.1.21)$$

In order to break this composite system down and form the controller, the system is connected as shown in Figure 3.1.

$$\dot{x}_k = A_kx_k + B_ky_c$$
$$u_p = C_kx_k \qquad (3.1.22)$$

Where,

$$C_k = \begin{bmatrix} F & U - FW \end{bmatrix}$$
$$B_k = L \qquad (3.1.23)$$
$$A_k = [A_c - LC_c + B_cu_rC_k]$$

Now that a method has been described for the controller design, the technique can be applied to the actual system.

3.2 Canard System Modeling

The canard assembly is shown in Figure 3.2. The actuator consists of a voice-coil, a linkage to translate motion to the canards, and an optical sensor to measure position.
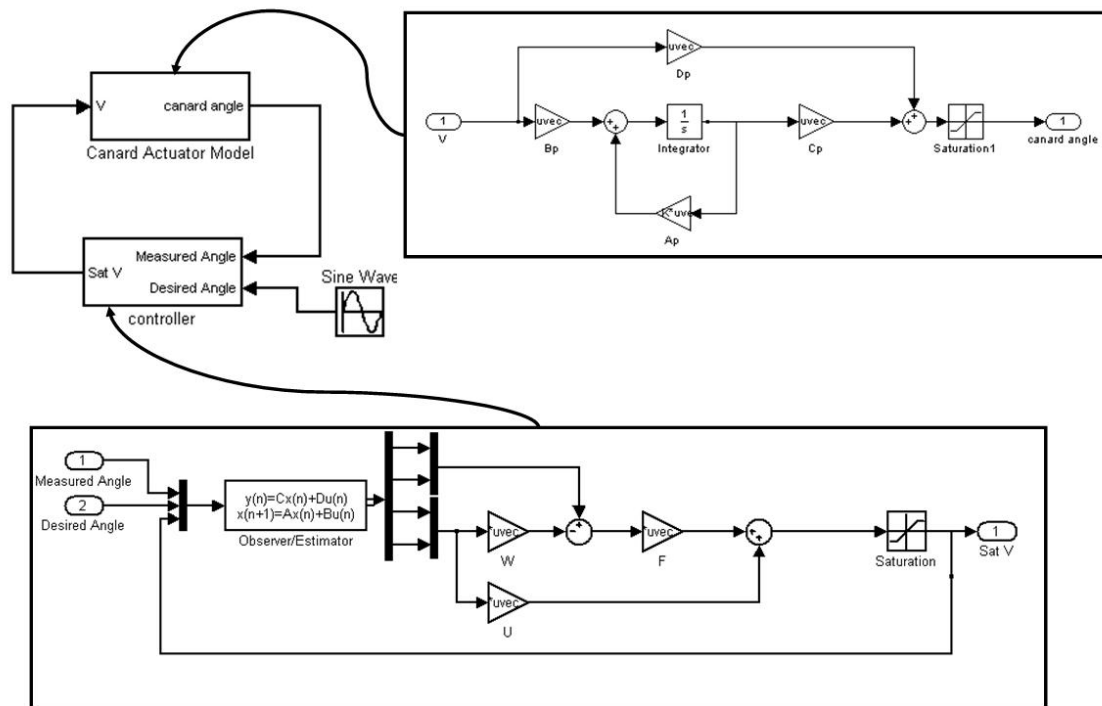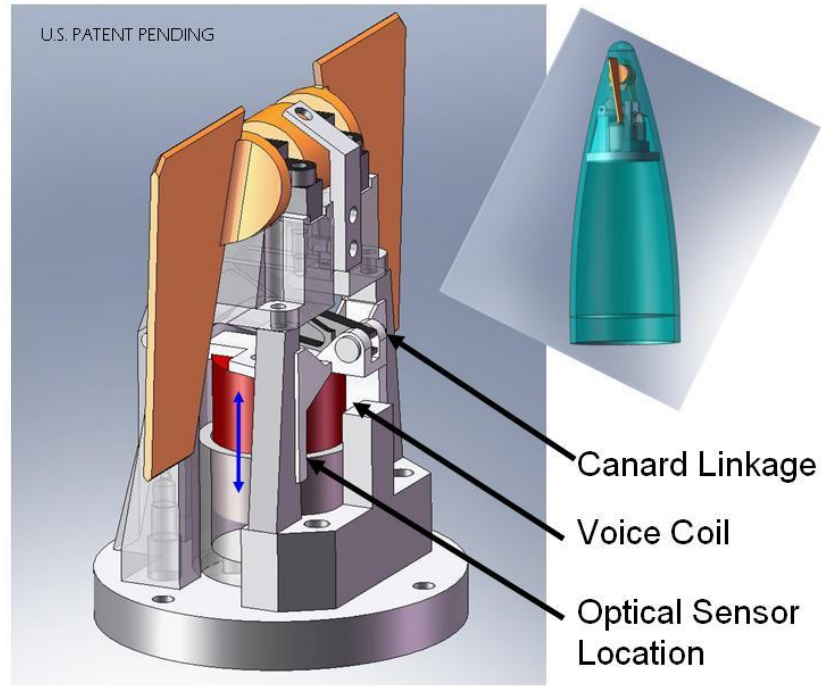
Figure 3.1: Controller System

Figure 3.2: Actuator Assembly

The voice-coil motor assembly utilizes the attached lever arm linkage to connect to the canards. The lever arm translates the linear motion of the voice-coil to rotational motion about the canard hinge. The voice-coil canards system is described by the following state space model.

$$
\begin{aligned}
\dot{x} &= \begin{bmatrix} 0 & 1 \\ \alpha_m & \beta_m \end{bmatrix} x + \begin{bmatrix} 0 \\ \gamma_m \end{bmatrix} u \\
y &= \begin{bmatrix} 1 & 0 \end{bmatrix} x
\end{aligned}
\tag{3.2.1}
$$

where α_m, β_m, and γ_m are defined by the system's electrical and mechanical dynamics. The state variables x_1, x_2 are the canard angle and angular velocity, respectively. Since the system has been augmented with the canard assembly, it is easier to lump the entire system together rather than to separate the system into multiple equations and gains. The "canard system" can now be characterized using system identification
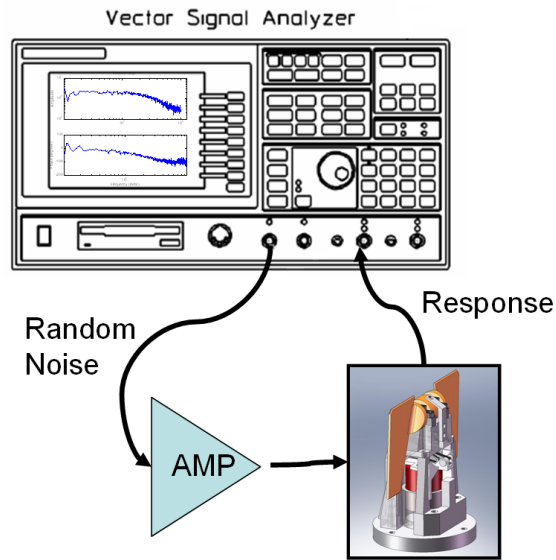
Figure 3.3: Signal Analyzer Setup

methods so the mathematical model will behave similarly to the actual hardware.

The system was connected to an HP vector signal analyzer to obtain frequency response data. The setup is shown in Figure 3.3. The signal analyzer produces a white noise signal that is connected through a power amplifier to the canard assembly. The power amplifier has its own characteristic frequency response, so the power amplifier's response was modeled prior to connecting to the canard assembly. A potentiometer was utilized for canard angle deflection measurements to interface the analog vector signal analyzer. The next step in system identification is to utilize step response data that will be incorporated into the actual drive electronics. In the real system the canard assembly will be controlled via Pulse Width Modulation (PWM). The reason for using PWM will be evident later in this section. Multiple step response data sets were obtained for the system using various PWM duty cycles and the measured canard angle deflection was obtained using an oscilloscope. The setup is shown in
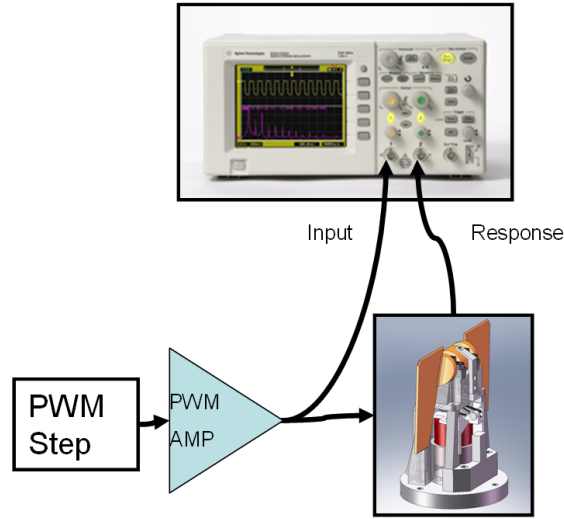
Figure 3.4: Step Response Setup

Figure 3.4. The step response data and the frequency response data were employed to create a model that fits the prototype of Equation (3.2.1). There are several methods for obtaining the unknown variables in the state equations which include Numerical Algorithms for Subspace State Space System Identification (N4SID) and the recursive Prediction Error Method (PEM). Utilizing both of these tools, it was found that with the PEM and a good initial guess of the system parameters, α_m, β_m, and γ_m, we could obtain a system model that truly represented the physical system. Figure 3.5a shows the step response of the physical system with respect to the predicted step response of the model, while Figure 3.5b shows the magnitude of the frequency response of the model vs. the experimental data. A good model has been found, utilizing the PEM technique, for the system which is utilized to design the regulator of Section 3.1. The regulator design parameters were chosen to track a sinusoidal signal with a frequency range from 10 to 30 Hz, an amplitude of 0 to ± 10 degrees, and phase error of zero. These constraints were placed on the design as the result of aerodynamic stability
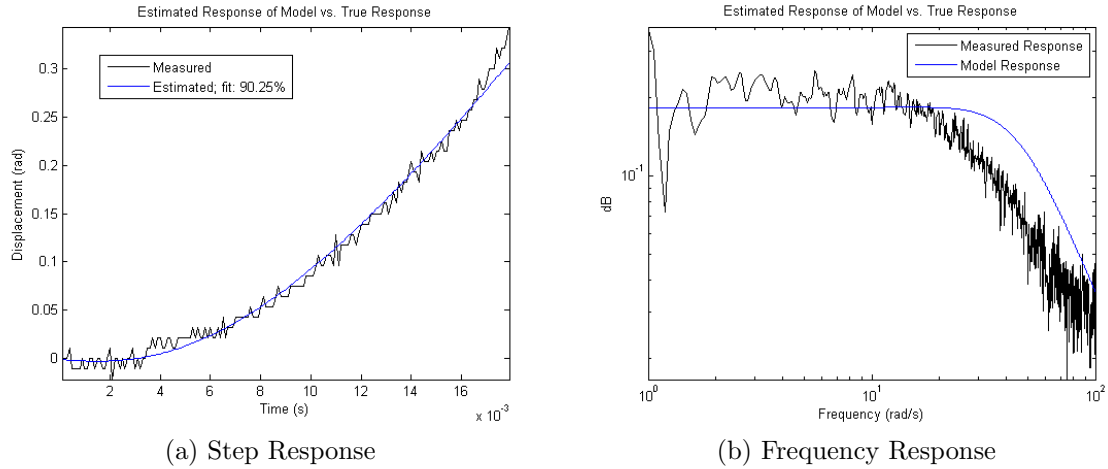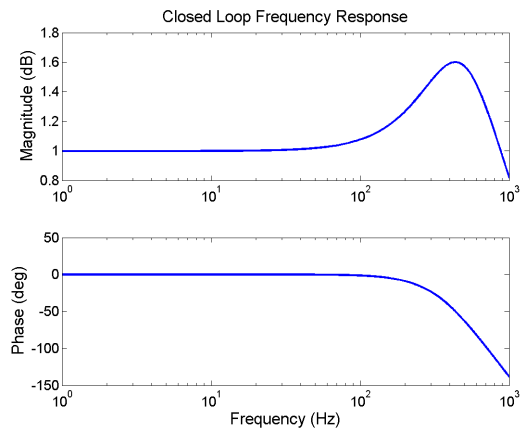
(a) Step Response (b) Frequency Response

Figure 3.5: Model Response

analysis. The input control constraint on the system limits the voltage to the battery voltage, which was set at 16 Volts. The tracking regulator was designed and Figure 3.6a shows the closed loop frequency response of the system. Figure 3.6b also shows the designed frequencies of interest for this system; where the maximum amplitude error is bounded by {0.9979,1.0346} [dB] and the maximum phase error is bounded by {0.0087,-0.4291} [rad]. The system was designed in a Matlab$^{©}$ [1] m-file, however we also use the Simulink$^{®}$ environment. The Simulink$^{®}$ block diagram is shown in Figure 3.7.

3.3 Aerodynamic Loading

The next step in the controller design was to test the system with the proper loading the canards would experience during flight. The moments on the canard themselves will be governed by the aerodynamic loading, which is proportional to the canard aerodynamic coefficients in Chapter 2. We can state that the angle of attack of the

---

[1]Matlab $^®$ is a Registered Trademark of Mathworks^{TM}, Inc.

(a) Close Loop Frequency Response
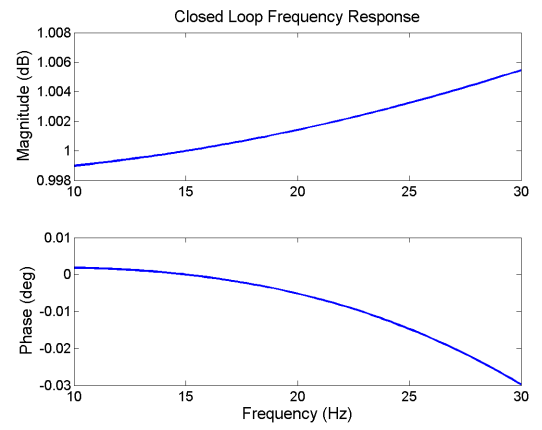
(b) Closed Loop Frequency Response 10 to 30 Hz

Figure 3.6: Closed Loop Response

Figure 3.7: Simulink® Block Diagram

canard, α_{tc} is the combined sum angle of attack of the body, α_t and the angle of deflection of the canard δ_c.

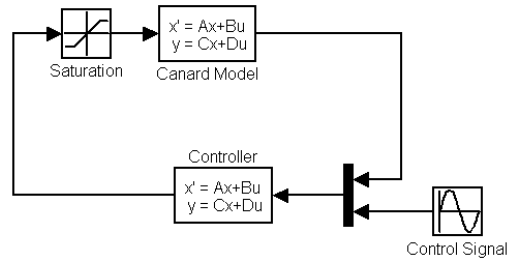In order to properly simulate the loading on the canards, the plant of Section 3.1 is augmented to match the dynamics associated with an aerodynamic loading. Using a torque sensor, we are able to understand the effect of a torque loading on the plant and modify the system parameters α, β, and γ. This technique has been validated by using a spring with a known spring constant and connecting the spring to the canard system to produce a spring damping. By knowing the spring constant, the canard system dynamics are adjusted to reflect the added force as well as the spring damping. The spring/canard system hybrid experimental response validated the predicted response determined by the Simulink$^®$ model of Figure 3.7.

Knowing that we can properly model the system is key to ensuring that when an applied aerodynamic torque is added to the system, the system will respond as predicted and maintain stability. Figure 3.8 is the new Simulink$^®$ model that provides inputs for the torque, caused by the aerodynamics, on the canard system.

Now that we have a representative relationship between the torque applied and the model response, we can use use the aerodynamics described in Chapter 2 to perform an aerodynamic study on the nominal control system. It is noted that a typical ballistic flight for the model was run to estimate the Angle of Attack (AOA) that a projectile might undergo. This will feed into our lookup tables for the aerodynamic coefficients which were obtained through Computational Fluid Dynamics (CFD) analysis. This effect on the system is shown in Figure 3.9 as an input noise to the original state space model.

A Monte-Carlo simulation was performed to analyze the effect of the aerodynamic

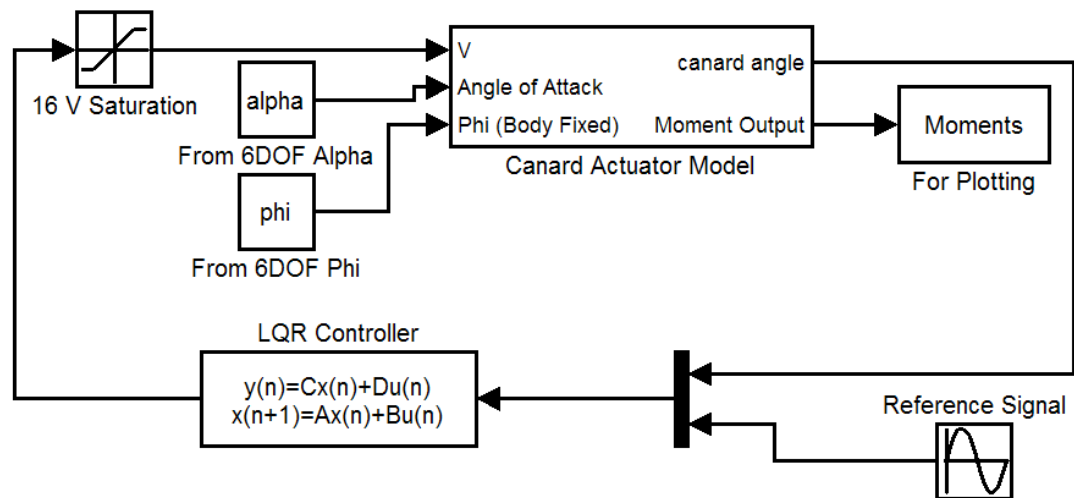Figure 3.8: Simulink® Block Diagram with Aerodynamics

Figure 3.9: Simulink® Block Diagram of Canard Actuator Model with Aerodynamics
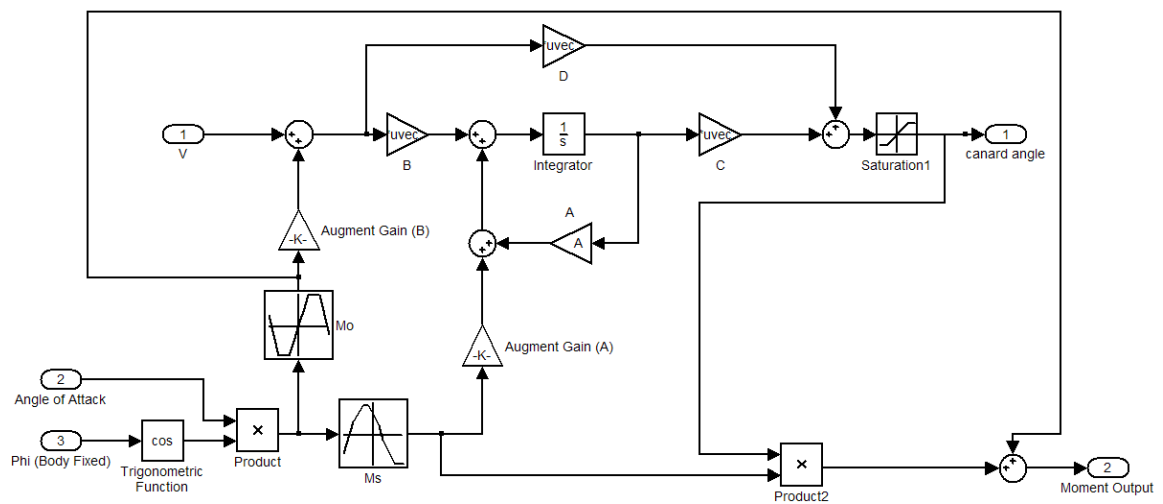
Figure 3.10: Monte Carlo Simulation 16V Saturation, 12Hz Oscillation
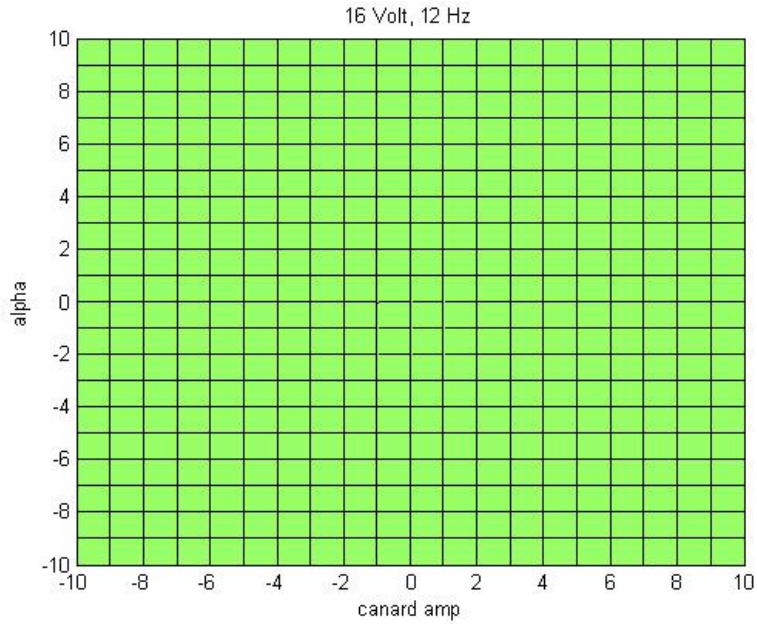
load and also to check the ability of the controller to maintain tracking of the sinu-soidal signal. Figure 3.10 shows the effective range of the controller across AOA of ± 10 degrees and canard actuation of ± 10 degrees with a spin rate of 12Hz.

In Figure 3.10, the green area shows the regions where the controller tracks the commanded signal correctly and maintains stability. The regulator will perform through all the commanded regions across a flight. Figure 3.11a shows the response of the system to a 18 Hz spin rate and Figure 3.11b shows the response of the system to a 25 Hz spin rate.

Figure 3.11b regions of stability are in blue and the various other colors indicate the regions where the system became unstable, either the canard becomes stuck to one extreme (+10 degrees or -10 degrees) or the sinusoidal tracking is inhibited. The torque applied to this particular voice-coil actuation system cannot exceed ≈ 0.6
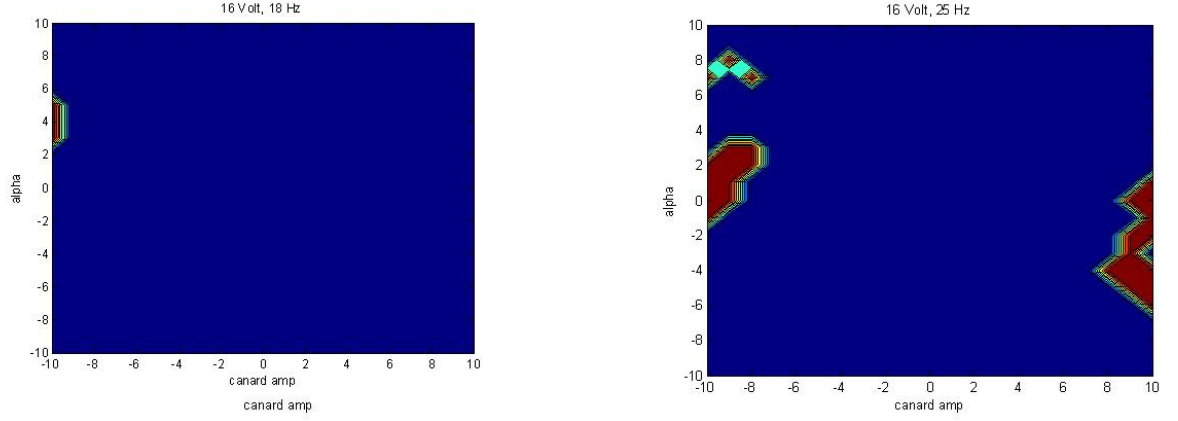
(a) Canard Response to 18 Hz Signal ±10 deg deflection

(b) Canard Response to 25 Hz Signal ±10 deg deflection

Figure 3.11: Canard Response to 18 and 25 Hz Signals

Nm. When this limit is exceeded, the power required to move the canard cannot be supplied by the battery, thus the canard will be driven to one side. To ensure the effects of spin rate and AOA on the torque are under the threshold, the aerodynamic coefficients must be accurately modeled. A CFD model was used to solve for the canard aerodynamic coefficients which is more reliable than standard prediction tools. As a result of the canard torque studies, the operation of the canard actuator will be limited to the regions of stability and the battery is selected accordingly.

To ensure that the canard system will be able to work throughout a full flight, the aerodynamics from Section 2.5 are coupled to the actuator model of Figure 3.12. The regulator/canard system is replaced with an "ideal" signal for the canard angle:

$$\delta_{can} = a_i \sin\left(\phi + \phi_i\right) \tag{3.3.1}$$

where δ_{can} is the canard angle, a_i is the commanded displacement, and ϕ_i is the phase difference between the roll angle, ϕ, and the y-axis. The ideal regulator was turned on after 1 second into the flight with an amplitude, $a_i = 10$ and $\phi_i = 0$.
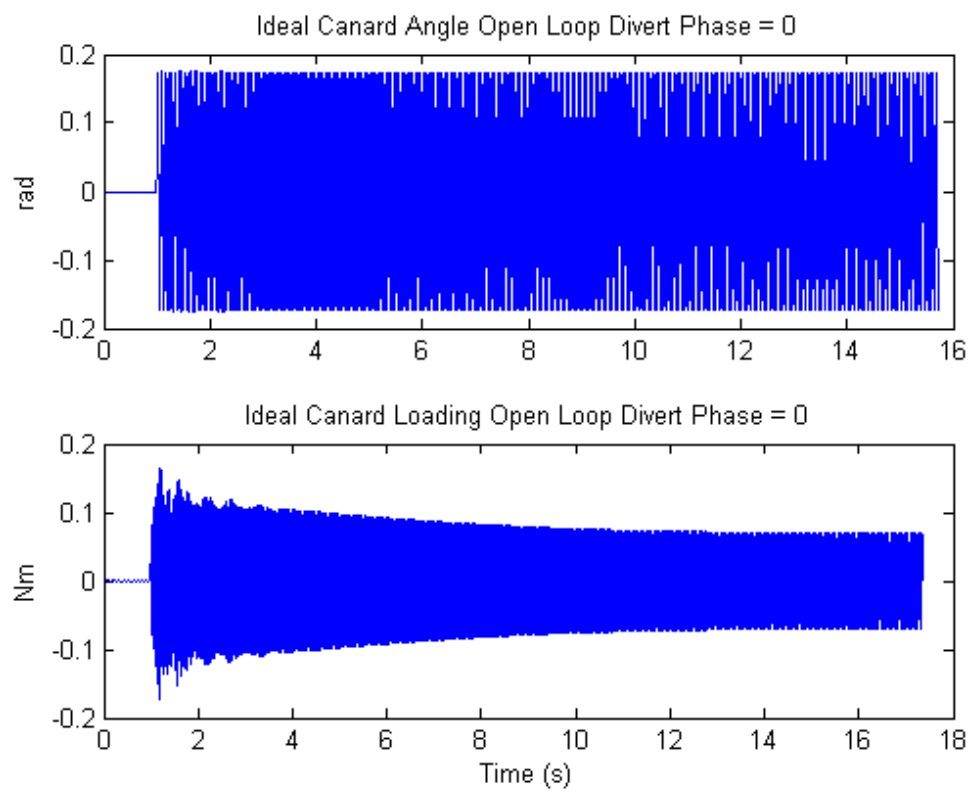
Figure 3.12: Ideal Canard Deflection

As shown in Figure 3.12, the loading on the canard never exceeds 0.5 Nm, therefore a 16V supply will work. It is also noted that the spin rate for this particular initial condition never exceeds 20Hz, and in a practical situation, guidance would not occur until the spin rate has reduced to approximately 15Hz. The plot of the spin rate is located in Figure 2.6 for the open loop ballistic flight.

3.4   Open Loop Divert

As mentioned, the canard actuation system has been designed to guide the projectile by oscillating at the spin rate. By controlling a phase difference between the canard angle and the roll angle, a net force can be generated to alter the flight path. The force is proportional to the canard angle and the AOA of the projectile. Figure 3.13 shows the relationship between the canard tracking angle, ϕ_r, and the net force direction on the body. The coordinate frame shown is when the roll angle, $\phi = 0$. To clarify, if the current projectile roll angle, $\phi = 0$, and the canards need to apply a lifting force or "go Up", the canard tracking phase must be $\phi_r = \frac{\pi}{2}$. Therefore, the tracking phase equals $\phi_r = \frac{\pi}{2} + \phi$, because the coordinate frame in 3.13 is rotating with angle ϕ.

The ballistic model of Chapter 2 will now be used in a closed loop simulation with the regulator. This demonstrates the tracking ability of the controller under the aerodynamic loading of a real flight. Figures 3.14 and 3.15 show the response of the system with the controller of Section 3.2 implemented in a Simulink® block diagram. Across the full flight, the moments about the canard never exceed the ≈0.6Nm threshold. The zoomed-in plot of Figure 3.15 shows the bimodal response of the canard moments as it rotates. This is due to the aerodynamic effects on the canard loading and the movement of the center of pressure, CP_{canard}. As the center of
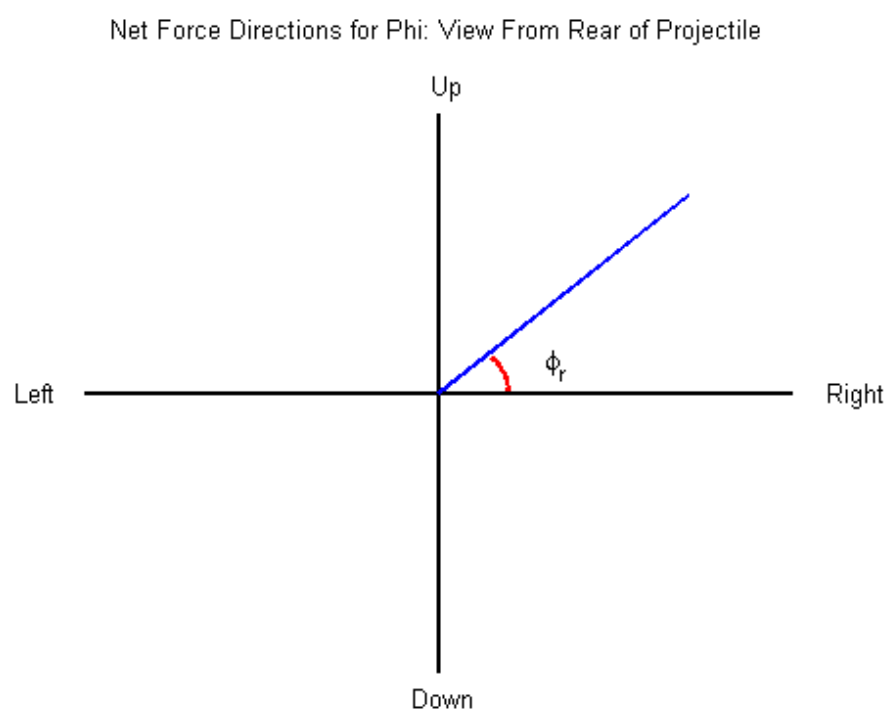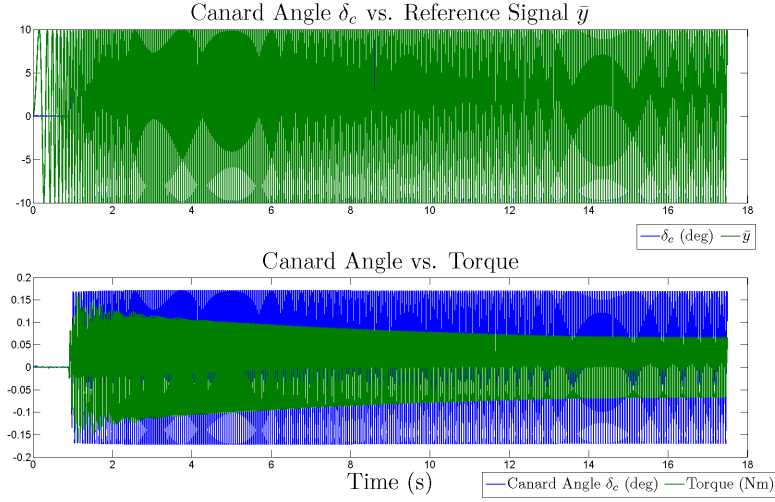
Figure 3.13: Command Maneuver Phase Relationship

Figure 3.14: Full Canard Loading Full Flight

pressure moves across the face of the canard, the Toque will vary due to the moment arm generated between CP_{canard} and the canard pivot point. The top plot in Figure 3.14 shows the canard displacement vs. the tracking signal. Figure 3.15 shows how closely the phase and frequency of the projectile phase angle command match the canard displacement angle.

The regulator is simulated in the 6DOF of Chapter 2 to show the performance of the system under an open-loop divert. The canard tracking angle, ϕ_r, is chosen to be 0 degrees, which would give a divert to the right. The relationship between the canard angle and the net force on the projectile is shown in Figure 3.13. The initial conditions for the projectile are the same as those in Section 2.5, the maximum deflection of the canard is $\pm 10 deg$, and the solver is Matlab® ode23 with $1e^{-4}$ maximum step size. Figures 3.16- 3.19 show the divert capability of the canard open loop maneuver with the ideal controller versus the regulator controlled canard.

Figure 3.16 shows the body velocities of the projectile. The plot of the velocity,
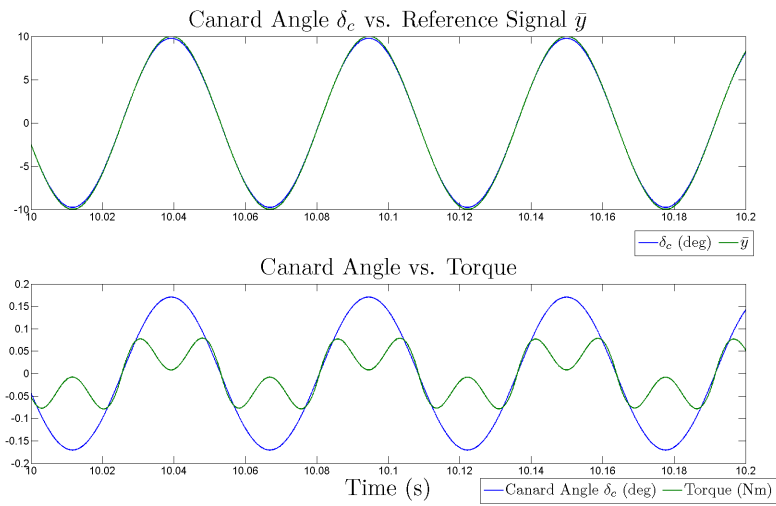
Figure 3.15: Full Canard Loading Zoomed In
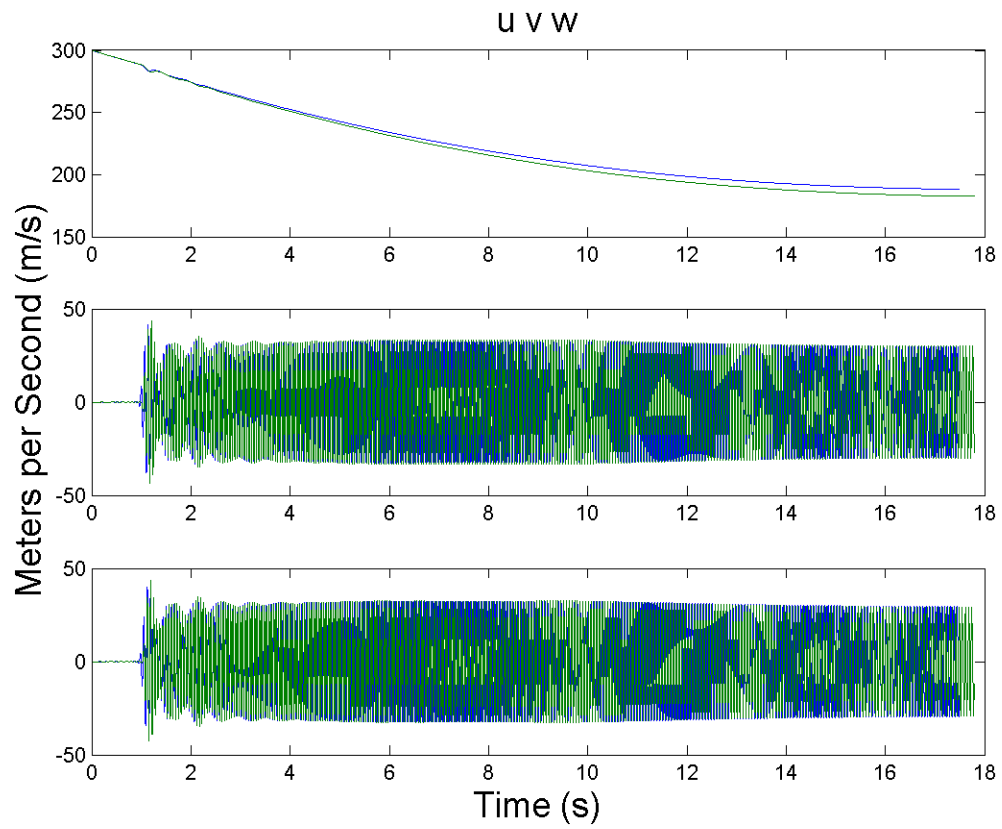
Figure 3.16: u,v,w Ideal Controller (green) vs. Designed Controller (blue)
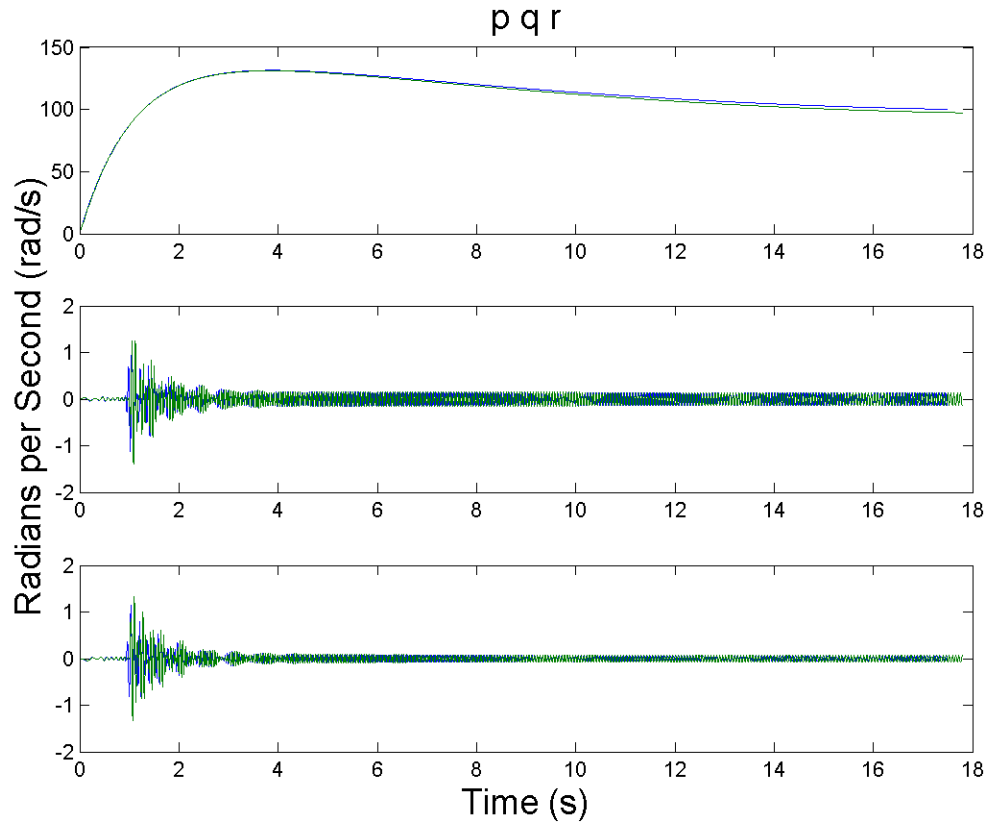
Figure 3.17: p,q,r Ideal Controller (green) vs. Designed Controller (blue)

u, shows how the the added drag due to canard motion will affect the overall velocity of the projectile. Comparing to the ballistic trajectory of Figure 2.5, the canards will introduce larger v and w components of the velocity vector which gives the projectile its divert capability. From the plots, the conclusion can be made that the regulators effects match closely to the ideal controller on the body velocities.

Figure 3.17 shows the effect of the canard system on the angular rates. When the canards begin oscillating, they induce larger angular rates than the typical ballistic flight shown in Figure 2.6. The effect of the canard will slowly damp out due to the rear tail fins providing the damping moment. The spin rate, p, is only slightly affected
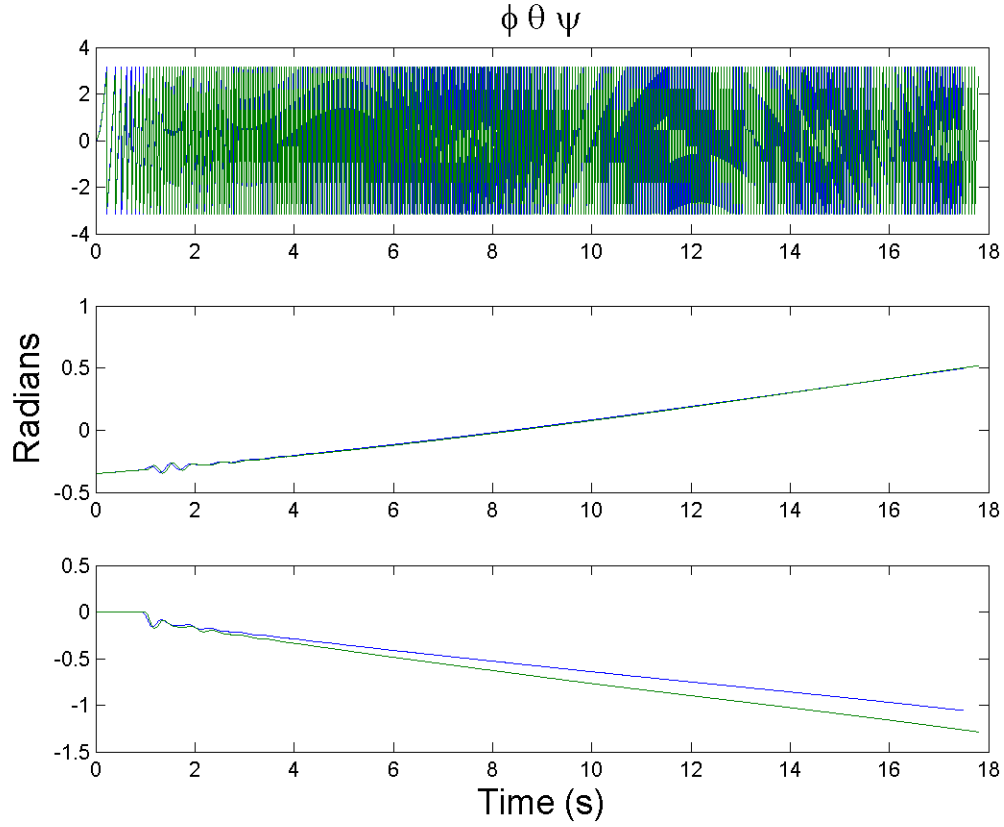
Figure 3.18: ϕ, θ, ψ Ideal Controller (green) vs. Designed Controller (blue)

by the regulator as shown in the top plot of Figure 3.17 and comparing to the top plot of Figure 2.6. The plots show that the regulator controller matches similarly to the ideal controllers affect on the angular rates.

Figure 3.18 shows the plots of the Euler angles vs. time. The initiation of the canard system at time, t=1, shows how θ and ψ will oscillate and damp out. The ideal tracking signal response matches very closely to the regulator results. The ψ plot shows the divert capability of the projectile as it moves to the right. The ψ plot can be compared to the ballistic flight plot in Figure 2.7 where the projectile slightly drifted to the left.
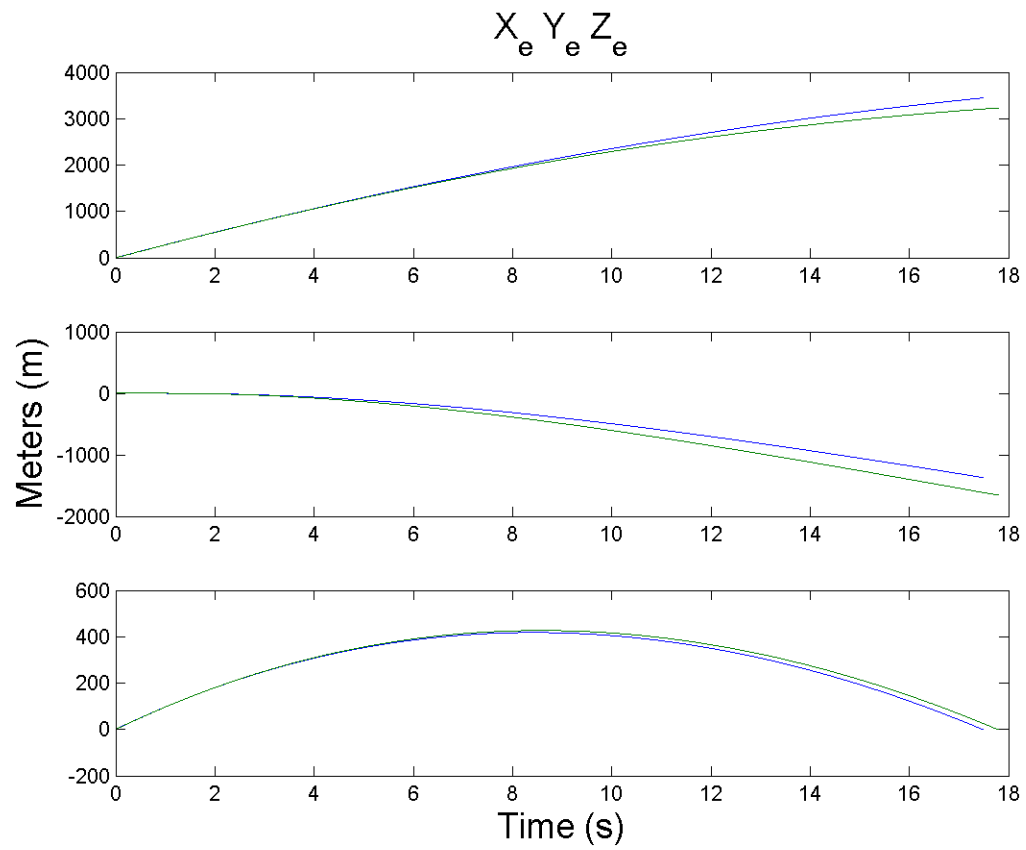
Figure 3.19: X,Y,Z Ideal Controller (green) vs. Designed Controller (blue)

(a) α, β vs. Time (b) α, β
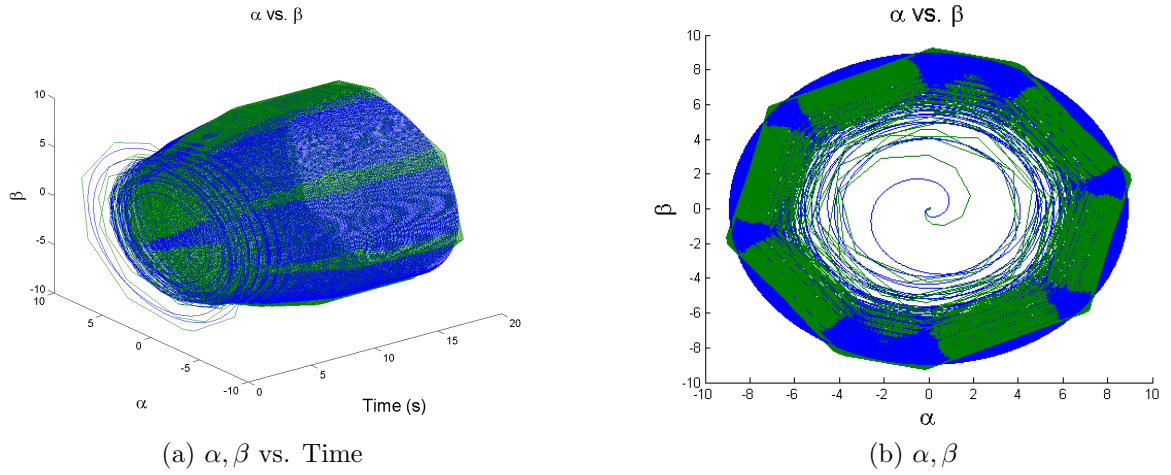
Figure 3.20: α, β Ideal Controller (green) vs. Designed Controller (blue)

Figure 3.19 compares the ideal divert capability to the regulator divert capability. The tracking controller extends the range as shown in the top plot, but this was not the goal, the intent was to divert to the right. The divert to the right is not as significant as the ideal controller as shown in the Y_e plot. The divert difference is due to small perturbations in the canard tracking phase. These perturbations attribute to some component of the force vector in the up direction, creating a lift force, shown in the Z_e plot.

Figure 3.21 shows the error between the canard angle and the perfect tracking signal in degrees. The plot shows that for the first second, the canard is held at 0 degree canard deflection and the error has no meaning. Throughout the rest of the flight, the tracking error of ϕ_r is below 0.5 degrees which is an acceptable error.

The conclusion can be made that the projectile remains stable as the yawing motion caused by the actuation reaches a limit cycle as shown in Figure 3.20a. The limit cycle is shared between the ideal signal and the regulator, which shows the regulator does not introduce any more instability than a perfect signal.
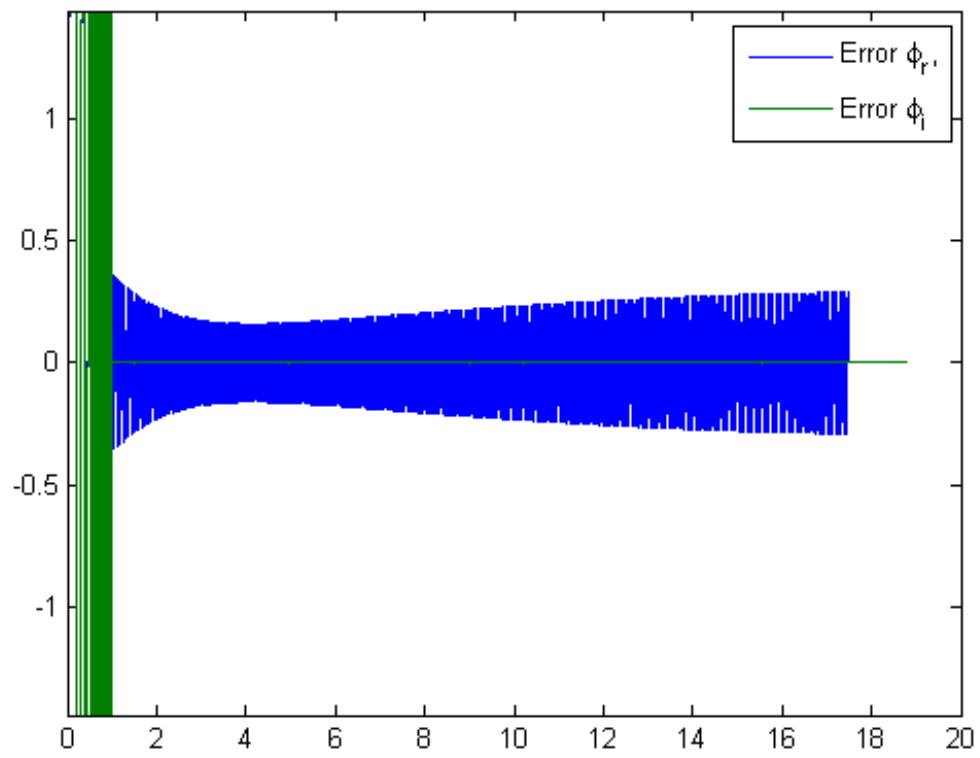
Figure 3.21: Ideal Controller (green) vs. Designed Controller (blue)
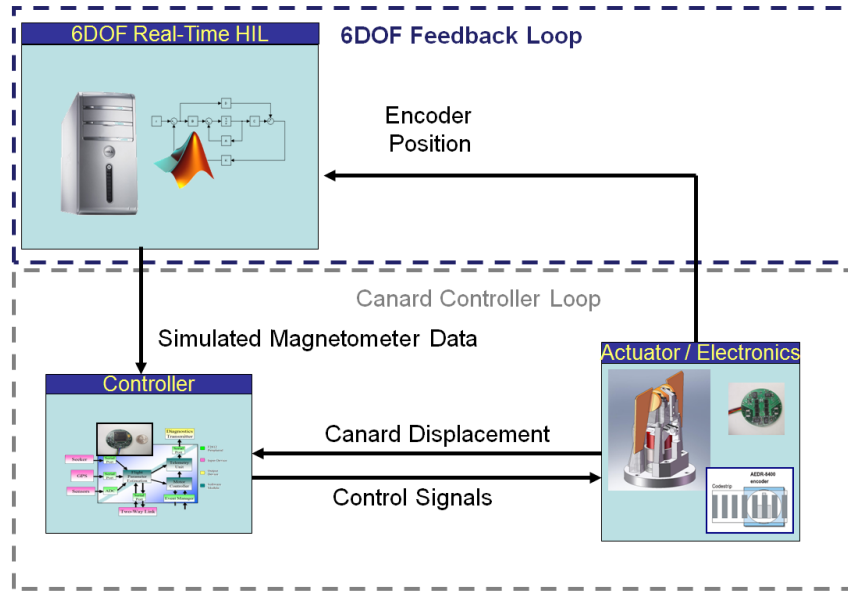
Figure 3.22: HIL Setup

3.5   Hardware-In-The-Loop

Now that the system was modeled correctly and we are obtaining the same response as expected (our response matches CFD analysis and the prediction tools), we will load the controller onto an onboard processor and test the response of the system. The configuration for the Hardware-in-the-Loop (HIL) is shown in Figure 3.22.

The PC running the 6DOF model has been developed using xPC Target^{TM} from Mathworks^{TM}. The PC utilizes a 3GHz Pentium 4 Processor with 2GB of RAM and contains a National Instruments Digital-to-Analog Converter (DAC) model number PCI-6733. The PC is running the Simulink® block diagram of Figure 3.23 at a loop rate of 5kHz. The 6DOF Simulink® model has been optimized to run at such a high rate in real-time because the 6DOF engine utilizes a fixed-plane model for the plant. The development of this model has been studied extensively in References [3, 39, 38, 30, 29, 28]. The fixed plane equations of motion are shown in the Appendix

A.1.

The controller we are using is the Texas Instruments, TI^{TM}, TMS320F2812 DSP, on a custom designed flight controller board. The Magnetometers, described in detail in Chapter 4, are simulated in the 6DOF Real-Time PC and ported through the DAC to the DSP's Analog-to-Digital Converter(ADC) which are updated in real-time. The controller's embedded software is generated from the Simulink® block diagram Figure 3.24 using Mathworks^{TM} Target Support Package^{TM} TC2 (for TIs C2000^{TM} DSP).

Figure 3.23: HIL 6DOF Setup

Figure 3.24: HIL DSP Controller

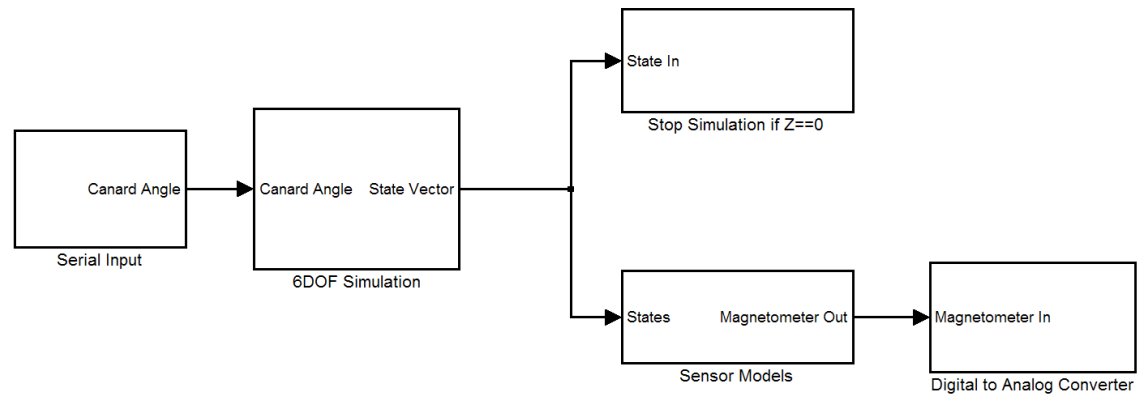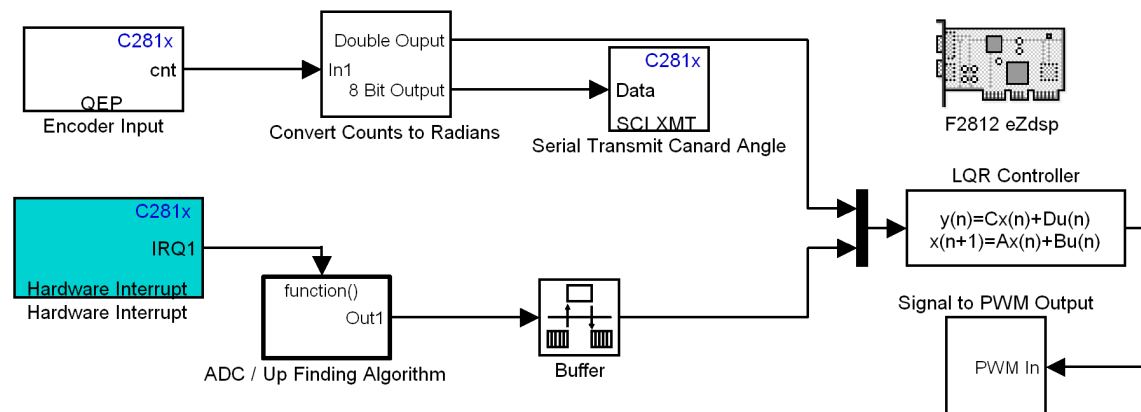The optical sensor, shown in Figure 3.2 is connected to the DSP via digital lines which can give a position measurement accurate to 0.0316 degrees. The voice-coil is driven with a power H-Bridge through a PWM signal from the DSP which is on a custom designed Printed Circuit Board (PCB).

The entire HIL experiment consists of two feedback loops, the regulator controller designed in this section as well as the 6DOF Real-Time Simulation utilizing the flight dynamics model of Chapter 2 which uses the canard angle as feedback. This information is streamed digitally via serial port from the DSP to the Personal Computer (PC). The loop rates are 10kHz for the DSP processor and 5kHz for the 6DOF. The canard feedback signal is connected to the 6DOF through a Zero-Order-Hold (ZOH).

The HILs setup is pictured in Figure 3.22. Since the information of the roll angle is required by the regulator, a simple estimate of the roll angle is performed at each regulator update. The solution for the roll angle, ϕ, is found using the following simplified equation using the magnetometer measurements:

$$\hat{\phi} = \tan^{-1} \frac{M_j}{M_k} \tag{3.5.1}$$

where M_j and M_k are defined later in Chapter 4 in more detail and $\hat{\phi}$ is the estimated roll angle. The detailed mathematics behind Equation (3.5.1) are explained in the appendix B. The reason for the simplified computations was not to demonstrate roll estimation, but the maneuver authority of the projectile. To ensure that the HIL system responds closely to the simulations, a baseline test was performed to ensure the HIL system solver was correctly updating the states. Figures 3.25- 3.27 show the 6DOF ballistic trajectory versus simulation.

As shown in Figures 3.25 and 3.27 the simulation matches the state propagation of the HIL system. Figures 3.28- 3.30 show the result of the flight controller response to
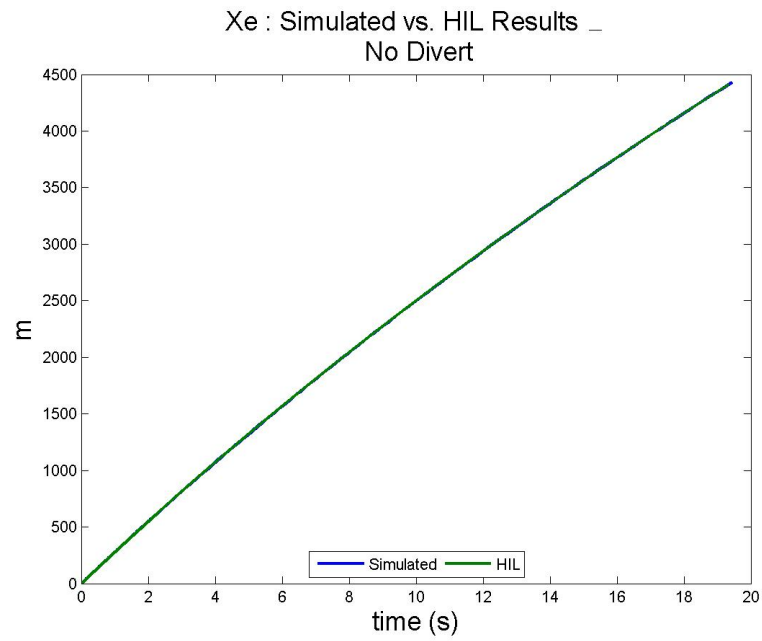
Figure 3.25: X_e Ballistic Trajectory
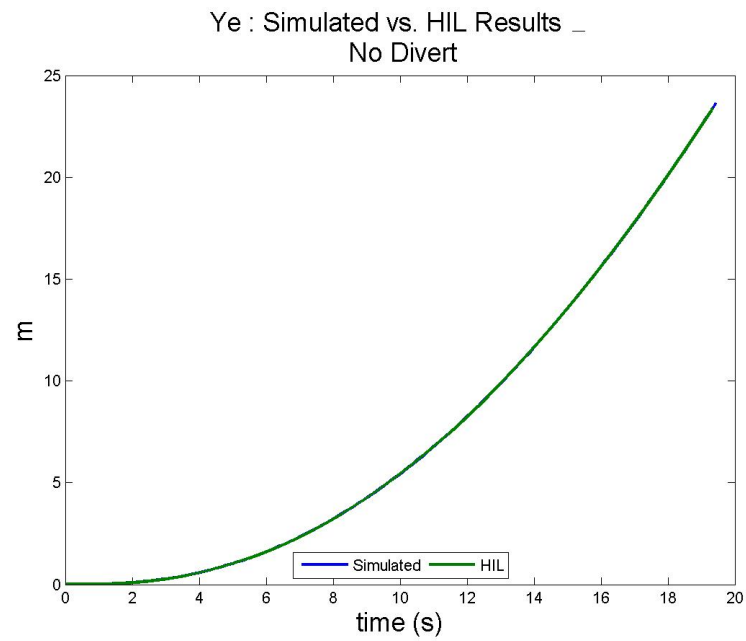
Figure 3.26: Y_e Ballistic Trajectory
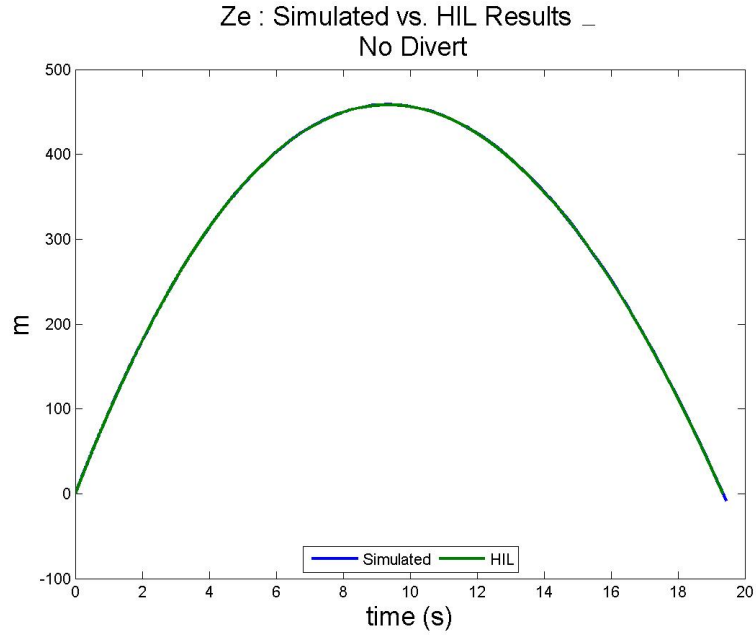
Figure 3.27: Z_e Ballistic Trajectory

a canard deflection of ± 6 degrees in the "up" direction. This displacement was chosen because of the physical constraints of the test setup on the canard. The controller was initialized using a "fire pulse" and did not begin the canard oscillation control until 2 seconds into the flight. As a reference, the ideal controller of the Section 3.4 is shown as a reference.

The same HIL experiment was performed with a start time of 9 seconds into the flight and the results are presented in Figures 3.31- 3.33.

From the HIL experiments, we can see that the controller is giving the lift in the correct direction, we do have some of the force "bleeding" over in to the cross range. This can be due to a phase lag on the controller, small error in amplitude, and estimation errors for the roll angle. The multiple runs were used to compare the results of turning on the controller during the up-leg of the flight (2 seconds), near
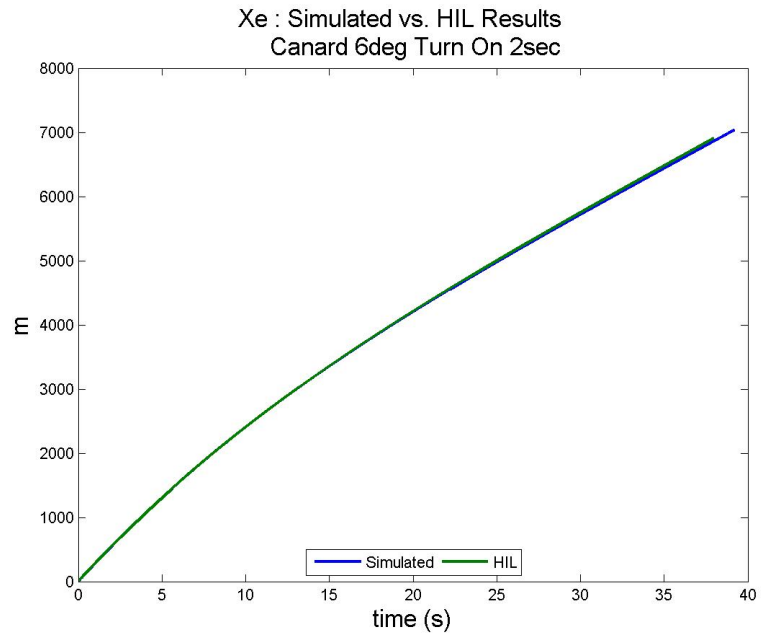
Figure 3.28: $X_e \pm 6$ degree deflection, 2 second turn-on
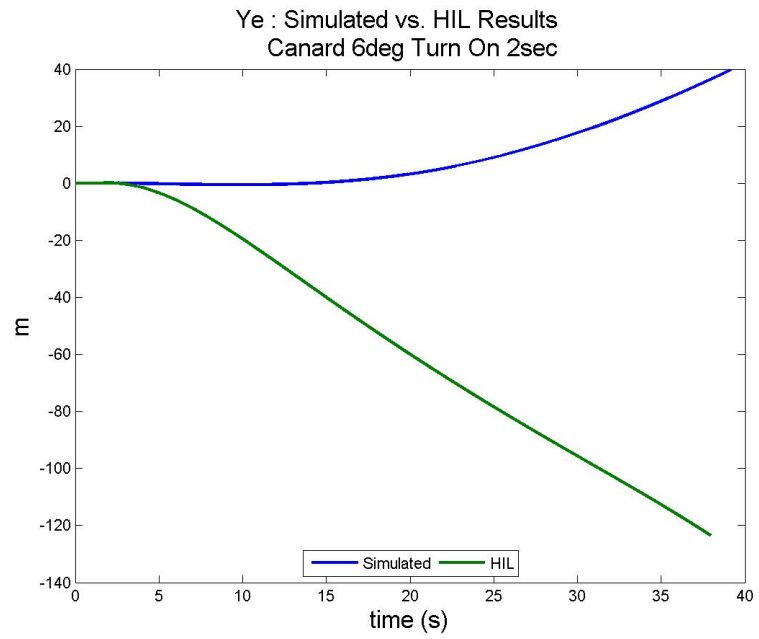
Figure 3.29: $Y_e \pm 6$ degree deflection, 2 second turn-on
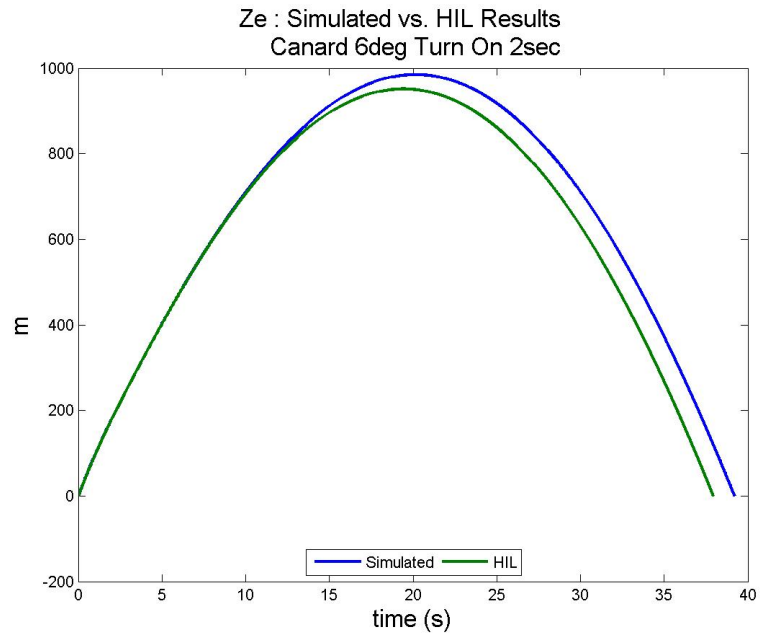
Figure 3.30: Z_e±6 degree deflection, 2 second turn-on
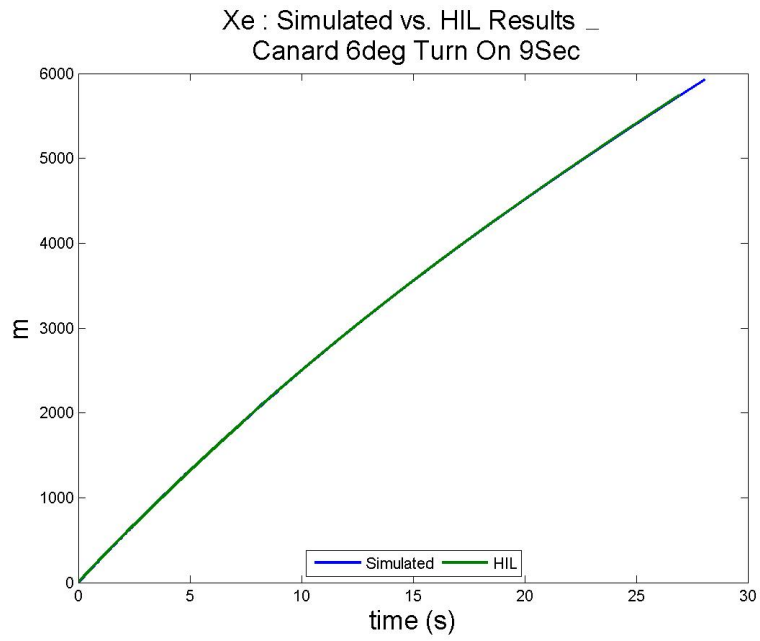
Figure 3.31: X_e±6 degree deflection, 9 second turn-on
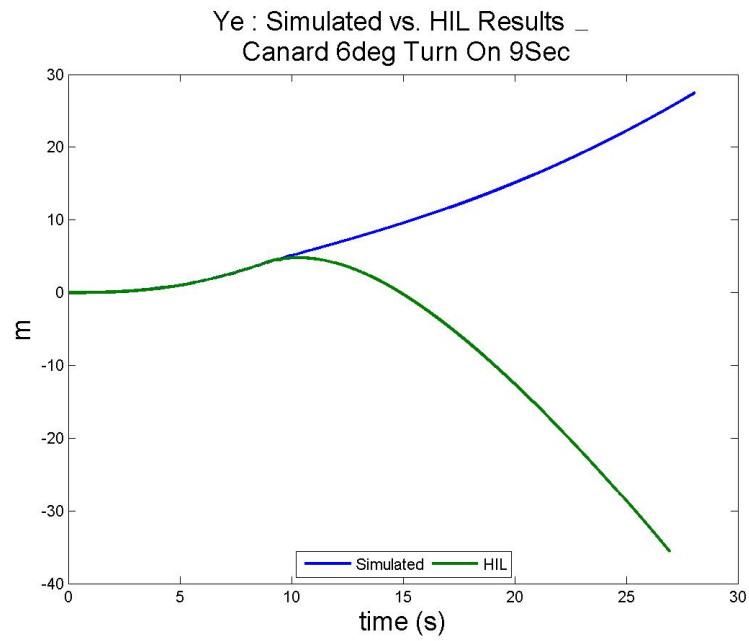
Figure 3.32: $Y_e \pm 6$ degree deflection, 9 second turn-on
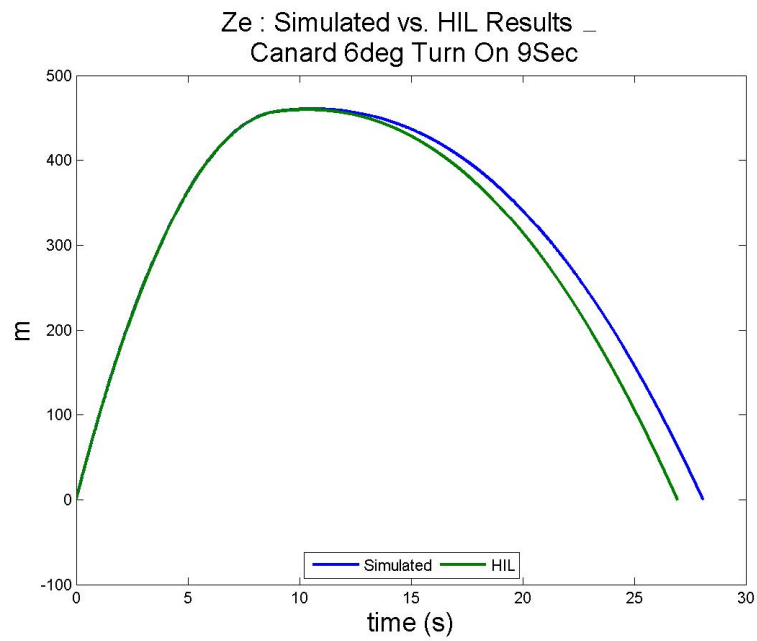
Figure 3.33: $Z_e \pm 6$ degree deflection, 9 second turn-on

apogee (9 seconds), and the no-divert case. Figures 3.28 and 3.31 show that turning the canard system on earlier in the flight will give the projectile more range, as one would expect. This comes at a price, as the maximum canard angle increases, the associate drag will begin to limit the range extension capabilities. Figures 3.29 and 3.32 show how the errors explained above have a much more dramatic effect on the projectile, the cross range component is much larger the longer the system is being actuated. Figures 3.30 and 3.33 demonstrate how the projectile will achieve a much higher flight profile when actuation begins at 2 seconds rather than 9 seconds.

The results are repeatable and the controller is acting similarly between simulations and HIL experiments. It should also be noted that the system does not have any aerodynamic loading on the canards. In order to compensate for the loads, we have added mass to the canard assembly to better resemble aerodynamic loading. The added load is not directly related to the response in flight because of the inability to add a bimodal effect. The aerodynamic inconsistency may also be attributing to the small mismatch between simulation and experiments. We can assume the bimodal effect of the aerodynamic loading will not have a significant effect in practice[1]. We can assume the controller will respond well during flight because the simulations are very similar to the HIL results. Now that the controller has been designed for the canard system, we can focus on possible estimation methods for the attitude.

---

[1]The controller will be validated with full aerodynamic loading in an upcoming wind tunnel test.

Chapter 4: Attitude Estimation

The information of the attitude of the projectile is required for the controller designed in Chapter Chapter 3 to work. The attitude of the projectile is also known as the angular orientation of the projectile. For practicality purposes, it is assumed that the sensors utilized to measure the attitude would be low-cost and preferably Commercial-Off-The-Shelf (COTS). Some sensors that are currently used in Inertial Measurements Units (IMUs) for projectiles include Accelerometers, Magnetometers, Rate Gyroscopes, and Solar Sensors. Since the body is in free-fall and dominated by acceleration greater than 1g, accelerometers are not practical for means of attitude measurement. The solar sensors that are currently used for attitude measurement are the most reliable of the four sensors types available, however, they are not practical for use in a tactical situation since they require the sun to be visible. The two remaining sensors that are available for use are magnetometers and rate gyroscopes which have been extensively utilized and studied at the US Army Research Laboratory as gun-launch survivable sensors.

4.1 Magnetometers

Extensive research has been conducted by the Army Research Laboratory (ARL) in the last decade to utilize low-cost magnetometers for attitude measurement in projectiles. The focus of the research is primarily in Anisotropic Magnetoresistive (AMR) Magnetometers which are extremely sensitive, solid-state magnetic sensors

designed to measure direction and magnitude of Earths magnetic fields. Magnetometers have been used for attitude estimations in spacecraft and other vehicles. References [41, 36, 2, 47, 27, 16, 10] include magnetometers for magnetic navigation purposes, however most of the techniques are difficult to implement in a projectile and have large time sampling period. References [23, 8, 8, 22, 25] explain the details associated with utilizing magnetometers onboard projectiles.

In order to develop the magnetometer as a viable sensor, we must create a model for the sensor that can be utilized in simulations and is practical for our application of attitude determination. For all purposes, we will assume that the AMR magnetometer that will be used has 3 sensitive axes which are perpendicular to each other. We can assume there is some bias to the magnetometer and scale factor from the embedded electronics and surrounding materials. The equation can be written to relate the magnetometer output, $\vec{m}$, to the applied magnetic field $\vec{B}$ by:

$$\vec{m} = \mathbf{D}\vec{B} + \vec{b} \qquad (4.1.1)$$

Where $\mathbf{D}$ is defined as off-axis and misalignment effects and $\vec{b}$ is a bias on the output measurements from any supporting circuitry. Each of these parameters can be predetermined or calibrated using methods described in References [25, 11, 12, 54, 44]. The magnetic field can be represented by:

$$\vec{B} = \mathbf{D^{-1}}(\vec{m} - \vec{b}) \qquad (4.1.2)$$

4.2 Rate Gyros

Rate gyroscopes are now available in small packages which allow them to be used in projectile attitude estimation. These newer MEMS based sensors are designed to

measure angular rate using the Coriolis force. MEMS sensors have the advantage of solid-state technology and are much more reliable than mechanical gyroscopes because they have no moving parts. Rate gyroscopes have also been proven over the years to be able to survive high-g gun launch, making them ideal at measuring both yaw and pitch rates. Futhermore, by modifying the dynamic range of commercial sensors as in Reference [48], we can measure roll rate with rate gyroscopes.

4.3   Quaternion Notation

In order to eliminate divergence problems using the Direction Cosine Matrix of Equation (2.1.9) and to reduce computation times required by the multiple trigonometric functions, we will use quaternion math. The quaternion is described by Equation (4.3.1)

$$\mathbf{q} = q_0 + q_1 i + q_2 j + q_3 k$$
$$\mathbf{q} = q_0 + \vec{q}$$

$$(4.3.1)$$

where,

$$i^2 = j^2 = k^2 = ijk = -1$$
$$\vec{q} = \{q_1, q_2, q_3\}$$

$$(4.3.2)$$

The addition of quaternions is defined by:

$$\mathbf{q} = q_0 + \vec{q}$$
$$\mathbf{p} = p_0 + \vec{p}$$
$$\mathbf{p} + \mathbf{q} = (q_0 + p_0) + (q_1 + p_1)i + (q_2 + p_2)i + (q_3 + p_3)k$$

$$(4.3.3)$$

The multiplication of quaternions $\mathbf{p}, \mathbf{q}$ can be defined by:

$$\mathbf{p} * \mathbf{q} = r_0 + \vec{r}$$
$$r0 = q_0 * p_0 - \vec{p} \cdot \vec{q}$$
$$\vec{r} = q_0 \vec{p} + p_0 \vec{q} + \vec{p} \times \vec{q}$$

$$(4.3.4)$$

The complex conjugate of a quaternion $\mathbf{q}$ is defined by:

$$\mathbf{q}^* = q_0 - \vec{q} \tag{4.3.5}$$

and its inverse is defined by:

$$\mathbf{q}^{-1} = \frac{\mathbf{q}^*}{\|\mathbf{q}\|^2} \tag{4.3.6}$$

where the norm, $\|\mathbf{q}\|$, is defined as $\sqrt{\mathbf{q}^*\mathbf{q}}$.

We can associate the quaternion with rotation using the following equation:

$$\vec{v}' = \mathbf{q}\vec{v}\mathbf{q}^* \tag{4.3.7}$$

as derived in [32]. The above equation can be written in matrix notation as:

$$\vec{v}' = R(\mathbf{q})\vec{v}$$

$$R(\mathbf{q}) = \begin{bmatrix} q_0^2 + q_1^2 - q_2^2 - q_3^2 & 2(q_1q_2 - q_0q_3) & 2(q_1q_3 - 2q_0q_2) \\ 2(q_1q_2 + q_0q_3) & q_0^2 + q_2^2 - q_1^2 - q_3^2 & 2(q_2q_3 - q_0q_1) \\ 2(q_1q_3 - 2q_0q_2) & 2(q_2q_3 + q_0q_1) & q_0^2 + q_3^2 - q_1^2 - q_2^2 \end{bmatrix} \tag{4.3.8}$$

which can be found in many texts.

This rotation is defined about the unit vector $\vec{u}$, or the axis of rotation, through the angle α, where $\mathbf{q} = cos\alpha + \vec{u}sin\alpha$ and $v \in R^3$. For $\mathbf{q}$ to be utilized as a rotational operator, it must be a unit quaternion, that is $\|\mathbf{q}\| = 1$. This requirement allows us to show that the inverse of the quaternion equals the conjugate, $\mathbf{q}^{-1} = \mathbf{q}^*$

We can now relate a quaternion to a rotation sequence. As an example we will use the standard aerospace sequence, YPR or Equation (2.1.9), and use the trigonometric notation of Section 2.1. Equation (4.3.10) defines the unit quaternion for the YPR rotation sequence. Where we can relate Equation (2.1.3) to the quaternion operator.

$$x' = \lambda x$$

$$x' = \mathbf{q}^* x\mathbf{q} = R(\mathbf{q})x \tag{4.3.9}$$

From the above definitions and relating the YPR sequence to Equation (4.3.10), we can find a relationship between Euler angles and a unit quaternion,**q**.

$$\psi_2 = \frac{\psi}{2}, \theta_2 = \frac{\theta}{2}, \phi_2 = \frac{\phi}{2}$$
$$q_0 = c_{\psi_2}c_{\theta_2}c_{\phi_2} + s_{\psi_2}s_{\theta_2}s_{\phi_2}$$
$$q_1 = c_{\psi_2}c_{\theta_2}s_{\phi_2} - s_{\psi_2}s_{\theta_2}c_{\phi_2}$$
$$q_2 = c_{\psi_2}s_{\theta_2}c_{\phi_2} + s_{\psi_2}c_{\theta_2}s_{\phi_2} \qquad (4.3.10)$$
$$q_3 = s_{\psi_2}c_{\theta_2}c_{\phi_2} - c_{\psi_2}s_{\theta_2}s_{\phi_2}$$

And to convert back to Euler angles,

$$tan\psi = \frac{q_1q_2+q_0q_3}{q_0^2+q_1^2-\frac{1}{2}}$$
$$\frac{1}{2}sin\theta = q_0q_2 - q_1q_3$$
$$tan\phi = \frac{q_2q_3+q_0q_1}{q_0^2+q_3^2-\frac{1}{2}} \qquad (4.3.11)$$
$$cos\theta > 0$$

4.4   Quaternion Extended Kalman Filter

In order to determine the attitude of the projectile, we can utilize the quaternion notation described in Section 4.3 to implement a Extended Kalman Filter. By coupling the measurement of the local Earth magnetic field in the body frame with rate sensors, we can estimate the attitude of the projectile. The following notation will be used:

Notation	Description
x	State Variable
$\hat{x}$	Estimate of State x
$\bar{x}$	Error Between State x and Estimate x
$\tilde{x}$	Measurements of States

Given Equation (4.3.8), we can state that the measurement of a reference field in the fixed coordinate system can be measured in the the rotation field by:

$$\vec{M}_b = R\left(\mathbf{q}\right)\vec{M}_e \tag{4.4.1}$$

Where M_b is the magnetic field measurement in the body fixed rotating frame, M_e is the local magnetic field, and $R\left(\mathbf{q}\right)$ is from Equation (4.3.8). Since there is noise on the system, we can rewrite Equation (4.4.2) to include noise on both the body and the reference measurements.

$$\vec{M}_b = R\left(\mathbf{q}\right)\left(\vec{M}_e + n_{\vec{M}_b}\right) + n_{\vec{M}_b} \tag{4.4.2}$$

Where n_{M_b} is the noise on the measurement and n_{M_e} is the noise on the reference vector. Using the components of $\mathbf{q} = \{q0, q1, q2, q3\}$ and $\vec{\omega} = \{p, q, r\}$, the rate of change of the quaternion is defined by:

$$\dot{\mathbf{q}} = \Omega\mathbf{q} \tag{4.4.3}$$

where,

$$\Omega = \begin{bmatrix} 0 & -p & -q & -r \\ p & 0 & r & -q \\ q & -r & 0 & p \\ r & q & -p & 0 \end{bmatrix} \tag{4.4.4}$$

Because we are using rate sensors, we have a measurement of $\{p, q, r\}$, however, this measurement contains noise, n_ω. n_ω is assumed zero mean Additive White Gaussian Noise (AWGN). Writing the measurements with noise:

$$\tilde{\omega} = \omega + \bar{\omega} \tag{4.4.5}$$

where, $\tilde{\omega}$ is the measurement for each of the rates, $\bar{\omega}$ is the error between the measurement and the true rates. Similarly, $\tilde{\Omega}$ is defined with elements $\tilde{\omega}$. The quaternion

can be estimated by:

$$\Omega = \tilde{\Omega} - \bar{\Omega}$$
$$\dot{\mathbf{q}} = \left(\bar{\Omega} - \bar{\Omega}\right)\mathbf{q} \tag{4.4.6}$$

$\bar{\Omega}$ is defined with the elements of $\bar{\omega}$. To find the the quaternion error $\bar{\mathbf{q}}$ we can subtract the estimate of the quaternion, $\hat{\mathbf{q}} = \tilde{\Omega}\hat{\mathbf{q}}$.

$$\dot{\mathbf{q}} - \dot{\hat{\mathbf{q}}} = \left(\tilde{\Omega} - \bar{\Omega}\right)\mathbf{q} - \tilde{\Omega}\hat{\mathbf{q}}$$
$$\dot{\bar{\mathbf{q}}} = \tilde{\Omega}\bar{\mathbf{q}} - \bar{\Omega}\mathbf{q} \tag{4.4.7}$$

And with matrix algebra, we can rearrange the last term $\bar{\Omega}\mathbf{q} = B\bar{\omega}$.

$$B\left(\mathbf{q}\right) = \frac{1}{2}\begin{bmatrix} q_1 & q_2 & q_3 \\ -q_0 & q_3 & -q_2 \\ q_3 & q_0 & q_1 \\ q_2 & -q_1 & -q_0 \end{bmatrix} \tag{4.4.8}$$

Equation (4.4.7) is now represented as

$$\dot{\bar{\mathbf{q}}} = \tilde{\boldsymbol{\Omega}}\bar{\mathbf{q}} + B\left(\mathbf{q}\right)\bar{\omega} \tag{4.4.9}$$

The error propagation for the quaternion is in continuous time, however, the EKF will be solved on an onboard processor, therefore, we require a discrete system. We can descretize the Equation (4.4.7) to yield:

$$\bar{\mathbf{q}}_{\mathbf{k+1}} = \Phi_k\mathbf{q}_{\mathbf{k}} + B_k\bar{\omega}_k \tag{4.4.10}$$

Where,

$$\Phi_k = e^{\tilde{\Omega}t_s} \tag{4.4.11}$$

The sampling time, t_s, would be defined by the dynamics of the system. We can ensure proper propagation with a sampling time $t_s \geq 10kHz$ for this particular application. The following equations are the summary of the Discrete Time Extended

Kalman Filter routine:

_____

Using the above state equations, we will assume the process noise, w_k, and measurement noise, v_k, to be zero mean AWGN:

$$w_k \approx (0, Q_k)$$
$$v_k \approx (0, R_k)$$
<div align="right">(4.4.12)</div>

We will Initialize the filter using:

$$\mathbf{q_0^+} = E\left(\mathbf{q_0}\right)$$
$$P_0^+ = E\left[\left(\mathbf{q_0} - \hat{\mathbf{q}}_0^+\right)\left(\mathbf{q_0} - \hat{\mathbf{q}}_0^+\right)^T\right]$$
<div align="right">(4.4.13)</div>

Next, we perform the state estimation update and the estimation error covariance update:

$$\Phi_{k-1}^- = e^{\tilde{\Omega}_{k-1}t_s}$$
$$B_{k-1}^- = B\left(\hat{\mathbf{q}}_{\mathbf{k-1}}\right)$$
$$\hat{\mathbf{q}}_{\mathbf{k}}^- = \left\|\Phi_{k-1}^- \mathbf{q_{k-1}}\right\|$$
$$P_k^- = \Phi_{k-1}^- P_{k-1}^+ \Phi_{k-1}^{-T} + B_{k-1}^- Q B_{k-1}^{-T}$$
<div align="right">(4.4.14)</div>

It should be noted that $e^{\tilde{\Omega}_{k-1}t_s}$ can be simplified utilizing spectral decomposition since the matrix is full rank and square:

$$\tilde{\Omega}_{k-1}t_s = VDV^{-1}$$
$$e^{\tilde{\Omega}_{k-1}t_s} = V(e_i^d I)V^{-1}$$
<div align="right">(4.4.15)</div>

Where D is the diagonal matrix composed of the eigenvalues of $\tilde{\Omega}_{k-1}t_s$, V is the corresponding eigenvalues, $d_i i \in \{1, 2, 3, 4\}$ are the diagonal elements of D, and I is the $4x4$ identity matrix.

Computing the partial derivatives with the priori estimate we obtain:

$$H_k^- = \left\{ \left.\frac{\partial R(\mathbf{q})}{\partial q_0}\right|_{\hat{\mathbf{q}}_k^-}, \left.\frac{\partial R(\mathbf{q})}{\partial q_1}\right|_{\hat{\mathbf{q}}_k^-}, \left.\frac{\partial R(\mathbf{q})}{\partial q_2}\right|_{\hat{\mathbf{q}}_k^-}, \left.\frac{\partial R(\mathbf{q})}{\partial q_3}\right|_{\hat{\mathbf{q}}_k^-} \right\} M_b$$
<div align="right">(4.4.16)</div>

The new measurements are used to update the state estimate, which is normalize to ensure rotation properties are maintained, and finally, the gain matrix is updated:

$$
\begin{aligned}
K_k &= P_k^- H_k^{-T} \left(H_k^- P_k^- H_k^{-T} + R_k \right)^{-1} \\
\bar{\mathbf{q}}_\mathbf{k} &= K_k \left[M_b - D_k M_e \right] \\
\hat{\mathbf{q}}_\mathbf{k}^+ &= \left\| \hat{\mathbf{q}}_\mathbf{k}^- + \bar{\mathbf{q}}_\mathbf{k} \right\|
\end{aligned}
\tag{4.4.17}
$$

The covariance matrix with a posterior data and another normalization is performed:

$$
\begin{aligned}
H_k^+ &= \left\{ \left. \frac{\partial R(\mathbf{q})}{\partial q_0} \right|_{\hat{\mathbf{q}}_k^+}, \left. \frac{\partial R(\mathbf{q})}{\partial q_1} \right|_{\hat{\mathbf{q}}_k^+}, \left. \frac{\partial R(\mathbf{q})}{\partial q_2} \right|_{\hat{\mathbf{q}}_k^+}, \left. \frac{\partial R(\mathbf{q})}{\partial q_3} \right|_{\hat{\mathbf{q}}_k^+} \right\} M_b \\
v_k^+ &= D_k^+ M_b \\
R_k &= R_{Me} + D_k^+ R_{Mb} \\
P_k^+ &= \left(I - K_k H_k^+ \right) P_k^- \left(I - K_k H_k^+ \right)^T + K_k R_k K_k
\end{aligned}
\tag{4.4.18}
$$

Now that we have a definition for the EKF, we can analyze the response.

4.5 Quaternion Extended Kalman Filter Results

As an example, we will use the system simulated in Chapter 2 for the attitude estimation.

$$
x0 = \{300, 0, 0, 0.0001, 0, 0, 0, -0.3491, 0.0000, 0, 0, 0, 0\}
\tag{4.5.1}
$$

We use Equation (4.3.10) to convert the initial condition Euler angles to the initial conditions for the quaternion.

$$
\mathbf{q0} = \{0.9848, 0.0000, -0.1736, 0.0000\}
\tag{4.5.2}
$$

The noise for the rate sensors and magnetometers is based on experimental results and determined to be $n_\omega = [0, 0.0698\rangle$ and $n_{Mb} = n_{Me} = [0, 0.0038\rangle$. It should be noted that this information is collected using properly calibrated sensors. We will

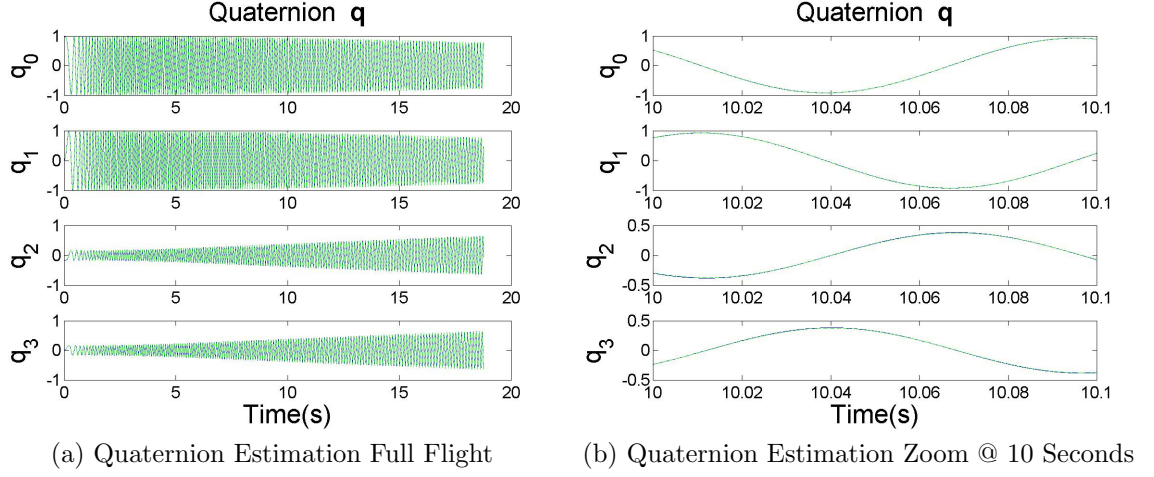(a) Quaternion Estimation Full Flight (b) Quaternion Estimation Zoom @ 10 Seconds

Figure 4.1: Quaternion Estimation (green) and True Quaternion (blue)

initialized the EKF using the following:

$$
\begin{aligned}
P_0 &= 1000 I_{4x4} \\
Q_{k0} &= .1 I_{3x3} \\
R_{M_{e0}} &= 30 I_{3x3} \\
R_{M_{b0}} &= 30 I_{3x3}
\end{aligned}
\tag{4.5.3}
$$

The 6DOF trajectory utilizes the ideal controller and not the designed controller of Chapter 3 to reduce simulation complexity, however, this substitution could easily be made. The controller is turned on at 1 second in and commanded to perform a right turn maneuver.

Figures 4.1a and 4.1b show the quaternion estimation for the full flight and a zoomed in region of flight, respectively. As shown, the EKF's estimated quaternion, $\hat{\mathbf{q}}$, tracks the true quaternion, $\mathbf{q}$, very well and does not deviate as the flight progresses. The quaternion error, plotted as $\mathbf{q} - \hat{\mathbf{q}}$, is shown in 4.2a and 4.2b. Though this plot gives no graphical meaning to the attitude error, it shows that the errors are very small.

(a) Quaternion Estimation Error Full Flight

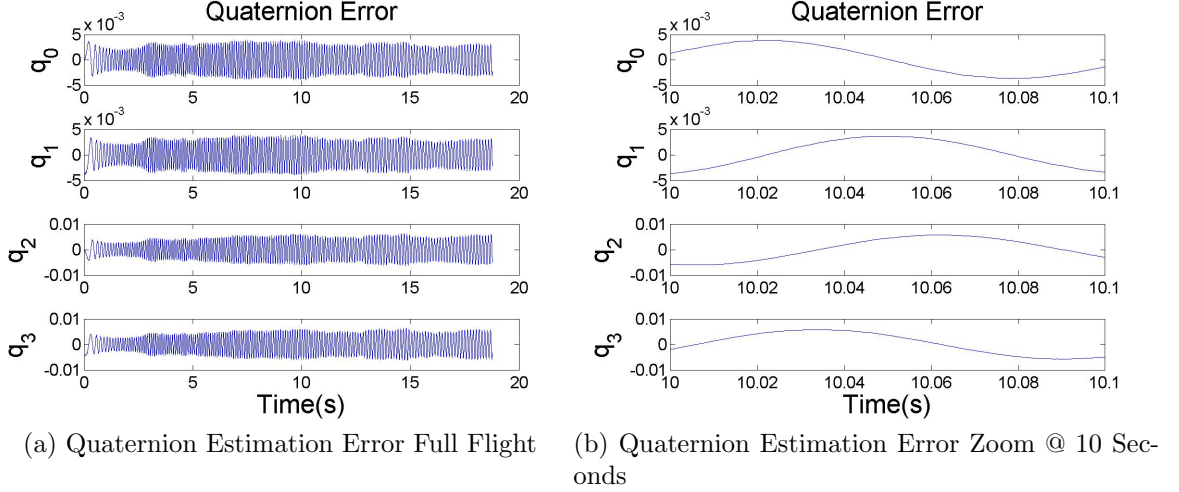(b) Quaternion Estimation Error Zoom @ 10 Seconds

Figure 4.2: Quaternion Estimation Error

In order to obtain a physical representation of the error, we can convert the quaternion to Euler angles using Equation (4.3.11). The Euler angles for the projectile are shown in Figures 4.3a and 4.3b. The angles are plotted in degrees, where we can see that ψ varies from $\approx 0 \rightarrow -75$, θ varies from $\approx -20 \rightarrow 30$ degrees, and the roll angle ϕ is bounded by ± 180 degrees. The Euler angles track very well and there is minimal error, as shown in Figure 4.3a. The projectile is making a right turn, as indicated by the psi angle, and we can see the overturning of the projectile in θ where apogee occurs at $\approx 9.7s$. Apogee can be defined as $\theta \rightarrow 0$. This attitude estimate will aid in the guidance system in Chapter 5. The Euler errors, in degrees, are plotted in Figures 4.4a and 4.4b, and are all $\leq .8 degrees$. This accurate estimate of the roll orientation will allow for us to control the projectile using the regulator of Chapter 3. It is also advantages to see how well the EKF will recreate our sensor measurements to gauge the performance of the EKF. Figures 4.5a and 4.5a show the magnetometer data recreation and how closely the EKF will track the true magnetometer sensors

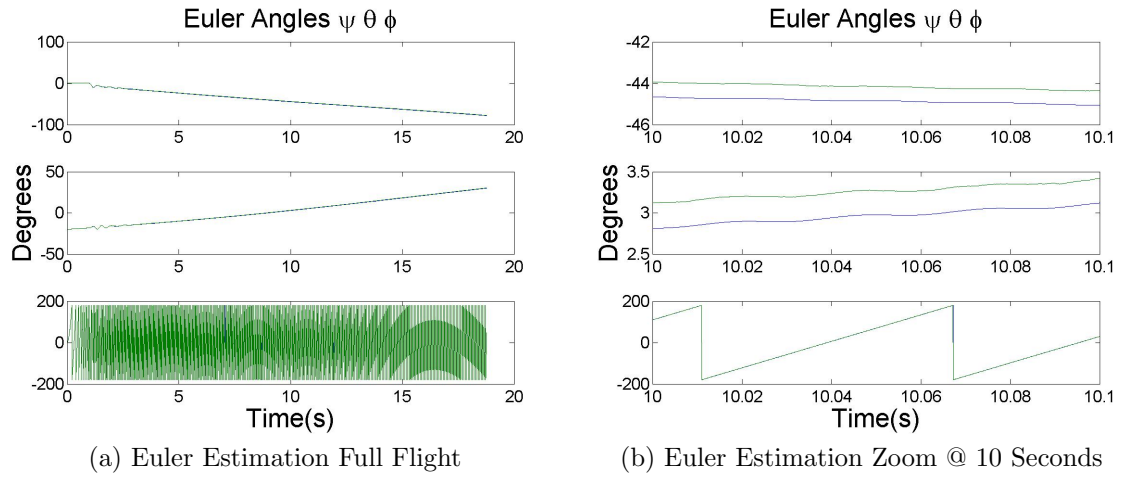(a) Euler Estimation Full Flight

(b) Euler Estimation Zoom @ 10 Seconds

Figure 4.3: Euler Estimation (green) and True Euler Angles (blue)

(a) Euler Estimation Error Full Flight

(b) Euler Estimation Error Zoom @ 10 Seconds

Figure 4.4: Euler Estimation Error

(a) Magnetometer Recreation Full Flight

(b) Magnetometer Recreation Zoomed @ 10 Seconds
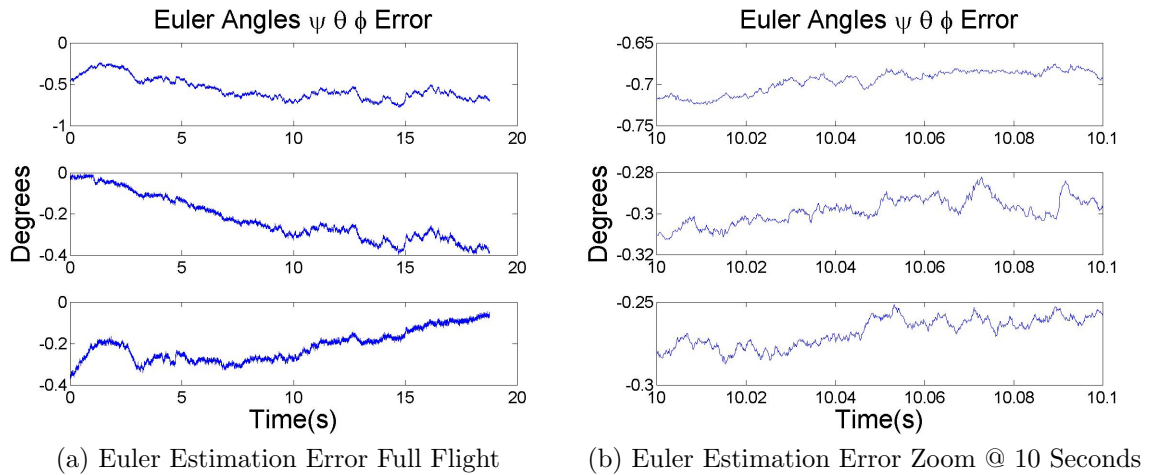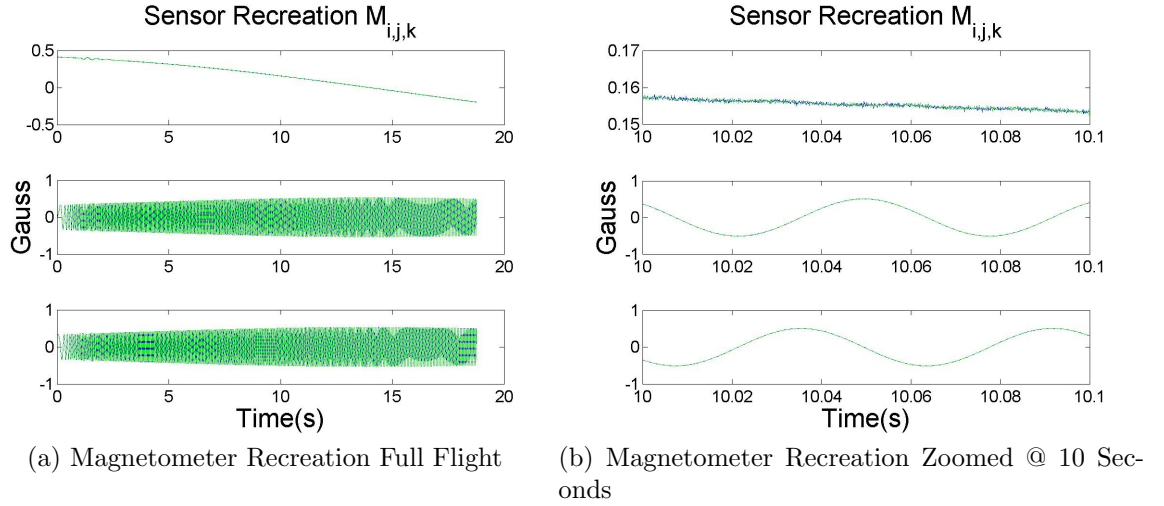
Figure 4.5: Magnetometer Recreation (green) Actual Magnetometer Data (blue)

measurements. In order to maintain confidence in the ability of the EKF to estimate the states, 1000 Monte-Carlo simulations were performed for a projectile in flight. At each run, the initial conditions for the gun orientation and noise seed on the sensors were varied. The variance of the gun orientation was ± 1 degree for θ, ϕ, ψ using a normal distribution. Figure 4.6 shows the mean error of each of the Euler angles throughout the flight. The plots show the mean error is always near zero degrees for each of the Euler angles. It has been demonstrated that the Quaternion Discrete Time Extended Kalman Filter tracks the quaternions/Euler angles for the projectile during flight. It is noted that the reliance on sensor measurement allows this system to track even during a maneuver. This simplified filter can be easily implemented on a DSP alongside the controller algorithm and does not require an extensive model of the entire projectile and its associated dynamics. Therefore, it can be concluded that the attitude can be tracked in real time at an update rate of 10kHz. Since the error magnitude is so small, the conclusion can be made that the tracking regulator will
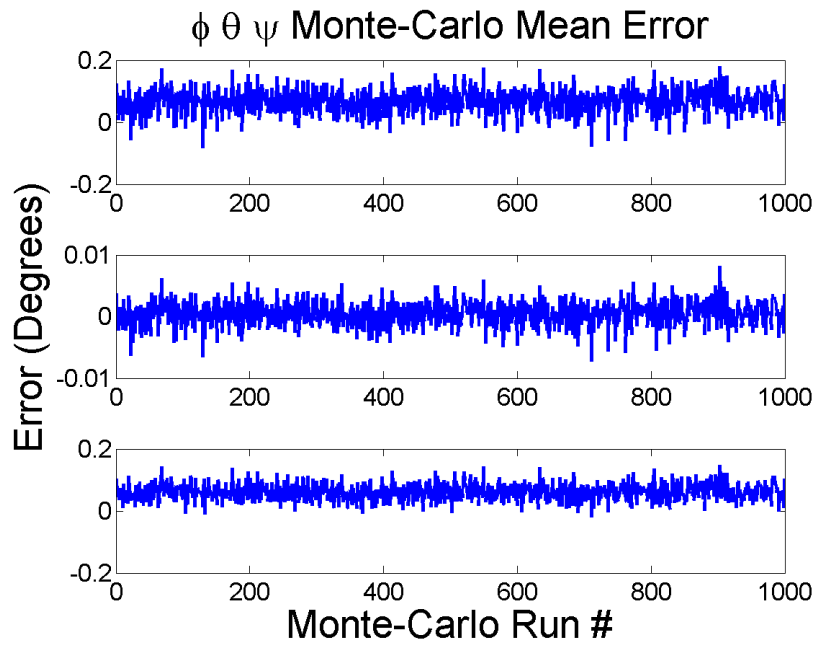
Figure 4.6: Mean Euler Estimation Error, 1000 Monte Carlo Simulations

perform well with the reference signal generated by the Quaternion EKF (QEKF).

Chapter 5: Projectile Guidance

Now that a method has been developed to determine the attitude of the projectile and we have a controller to determine the canard position, a guidance controller must be designed to guide the projectile to engage the target. In order to predict the onboard states that are not determined by the attitude, $\{X_e, Y_e, Z_e\}$, and corresponding earth fixed velocities, $\{V_{xe}, V_{ye}, V_{ze}\}$, a GPS module is utilized. The GPS system provides the state information at a 10Hz update rate and requires approximately 5 seconds to acquire the satellites.

In this chapter, we will present the two methods for guidance; Impact Point Prediction (IPP) and Modified Proportional Navigation (MPN). We will demonstrate the effectiveness of hitting a target when the canard perfectly tracks the commanded guidance signals, the regulator with ideal state estimation, and finally a fully integrated system with estimated states and multivariable regulator and H_2 control system.

5.1   Impact Point Prediction

Though Impact Point Prediction has been studied using linear projectile theory, [30, 29, 28], an alternative method of using a simple point mass model / vacuum trajectory will be utilized to integrate the states forward in time and calculate the impact point. Though this method is fairly simple, it should provide enough fidelity to prove a successful Circular Error Probable (CEP). The equations of motion for the projectile

in the vacuum / point mass are given by:

$$X_e = X_0 + V_{x0}t + \frac{1}{2}\left(-\frac{\frac{1}{2}\rho V^2 A C_X}{m}c_\theta c_\psi\right)t^2$$
$$Y_e = Y_0 + V_{y0}t + \frac{1}{2}\left(-\frac{\frac{1}{2}\rho V^2 A C_X}{m}c_\theta s_\psi\right)t^2 \quad\quad (5.1.1)$$
$$Z_e = Z_0 + V_{z0}t + \frac{1}{2}\left(-g - \frac{\frac{1}{2}\rho V^2 A C_X}{m}s_\theta\right)t^2$$

We can solve the above set of equations at each GPS update to determine the estimated impact point. For each time that we solve the equations, we will utilize the latest values of ρ, θ, V, and initialize $\{V_{x0}, V_{y0}, V_{z0}, X_0, Y_0, Z_0, \}$ with the GPS updates. We will assume for simplicity that $c_\psi = 1$. The unguided projectile will have a small component ψ and the errors from this substitution would be negligible. The drag coefficient C_X is evaluated each iteration of the impact point prediction. The mach number is evaluated using lookup tables which contain the meteorological information.

Since we have a target location, $\{X_t, Y_t, Z_t\}$, the equations of Equation (5.1.1) can be solved to find a the time to impact, t_i. This impact time can then be used in the equations for cross-range impact, Y_i, and down-range impact, X_i. Because the system is only affected by drag, it is assumed that the impact point prediction should be off and progressively improve as the projectile flies. The following plot is an example of impact point prediction with no guidance utilizing the same 6DOF model and initial conditions as Section 2.5.

The plots in Figure 5.2 show the impact point calculations, in blue, will eventually converge on the correct impact point solution of 4448.0m for Xe and 28.8404m for Ye. The oscillations shown in Figure 5.1b can be attributed to the s_ψ term in Equation (5.1.1). Figure 5.1a shows the impact point prediction is predicting the projectile will land further than the true impact point until apogee, at 9.8 seconds. If the projectile attempted to maneuver prior to apogee, the projectile would potentially fall short of

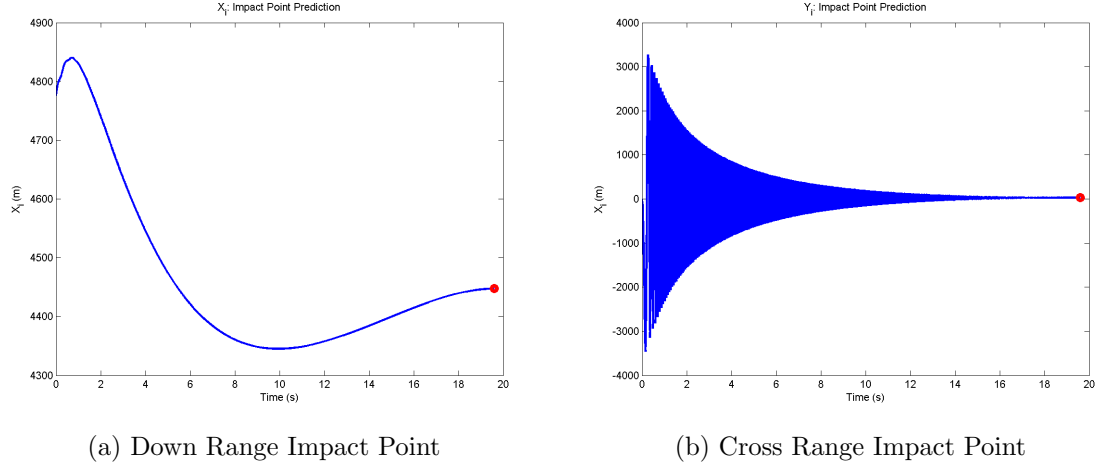(a) Down Range Impact Point .... (b) Cross Range Impact Point

Figure 5.1: Impact Point Prediction (blue), True Impact Point (red)

the target because of IPP prediction errors. To ensure the proper IPP is obtained, the projectile would not begin guidance until apogee.

5.2 Guidance Definitions for Impact Point

Now that we can effectively determine the impact point, we can calculate the error between the impact point and the target.

$$
\begin{aligned}
e_x &= X_i - X_t \\
e_y &= Y_i - Y_t
\end{aligned}
\tag{5.2.1}
$$

It is not necessary to correct for the altitude because the solution is already determined in the IPP equations. The error between the impact point and the target is evaluated to determine the direction and magnitude the canard controller must operate to successfully navigate to the target. Figure 5.2 shows the $X_e Y_e$ plane, the location of the target is located at the origin of this frame. The error between the impact point, shown in red, and the target can be related in polar coordinates. By mapping the polar coordinates to a commanded phase/amplitude relationship for the canard
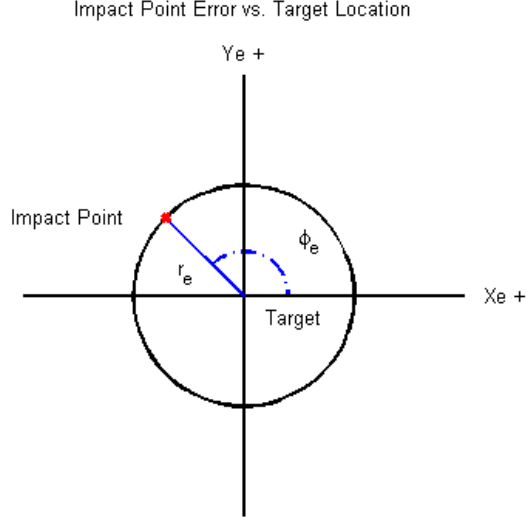
Figure 5.2: Impact Point Error Definition

tracking signal, we can develop a navigation routine to hit the target. Where,

$$\phi_e = a\tan 2\left(\frac{e_x}{e_y}\right)$$
$$\|r_e\| = \sqrt{\left(e_x^2 + e_y^2\right)} \tag{5.2.2}$$

where the error angle, ϕ_e, can be mapped to the canard tracking angle, ϕ_r, by adding $\frac{3\pi}{2}$ and the error magnitude is $\|r_e\|$. The mapping from the polar coordinates to the canard tracking signal can be visualized with the following example:

Using the impact point (red) in Figure 5.2, the IPP predicts the projectile will miss the target, short and to the left. In order for the projectile to hit the target, the projectile must guide up and to the right. Using the above definitions and Figure 3.13, the phase error, $\phi_e \in \{\frac{\pi}{2}, \pi\}$, can be mapped to the canard tracking phase $\phi_r \in \{0, \frac{\pi}{2}\}$.

To provide the necessary mapping of the miss distance, $\|r_e\|$, to the commanded

canard deflection amplitude, δ_c, a simple PI controller is used:

$$\delta_c = K_p \|r_e\| + K_i \int_0^t \|r_e\| dT \qquad (5.2.3)$$

Where the constants K_p and K_i are chosen experimentally.

5.3 Guidance Method using Modified Proportional Navigation

As an alternative method for guidance, we wish to choose the target location and the current state of the projectile as the primary variables and not the impact points. We will use the same notation for the current velocity and position as $\{V_{xe}, V_{ye}, V_{ze}, X_e, Y_e, Z_e\}$ which are defined in the earth fixed reference frame. The target, which is also in the body fixed reference frame is $\{V_{xe_t}, V_{ye_t}, V_{ze_t}, X_{e_t}, Y_{e_t}, Z_{e_t}\}$. Since we have control of the acceleration of the projectile through the canards, a control law can be realized using the accelerations. Using the standard Kinematic equations of motion for a rigid body:

$$\vec{r} = \vec{r_0} + \vec{v} * t_{go} + \frac{1}{2}\vec{a}t_{go}^2 \qquad (5.3.1)$$

Where t_{go} is the time-to-go in flight, which is related to $t_{go} = t_f - t_c$, r is the relative displacement, v is the relative velocity, and a is the relative acceleration. Therefore, the velocities and the position are related to the acceleration using Equation (5.3.4).

$$\vec{a_p} = \frac{(\vec{r_t} - \vec{r_p}) + (\vec{v_t} - \vec{v_p}) * t_{go} + \frac{1}{2}\vec{a_t}t_{go}^2}{t_{go}^2} \qquad (5.3.2)$$

The subscript p denotes the projectile and the subscript t denotes the target. Each of the vectors are described in the earth frame. We will make the following assumptions:

- The projectile will be mostly under the influence of gravity.

- The target is stationary i.e. no velocity or acceleration.

- The projectile has no thrust.

From the first two assumptions, we can state that the time-to-go, t_{go} is the positive solution to the quadratic equation.

$$0 = z_t - z_p - v_{pz}t_{go} - \frac{1}{2}gt_{go}^2 \tag{5.3.3}$$

The solution for t_{go} can be visualized by assuming a vacuum flat fire trajectory at each computation point. One can assume that without the effect of body lift, the impact time will be proportional to the height. For example, if a bullet was fired with 0 degree quadrant elevation and at the exact same time a bullet was dropped, they would both hit the ground at the same time.

$$\begin{bmatrix} a_{px} \\ a_{py} \\ a_{pz} \end{bmatrix} = \vec{K}_p \frac{\begin{bmatrix} x_t - x_p \\ y_t - y_p \\ z_t - z_p \end{bmatrix} - \begin{bmatrix} v_{px} \\ v_{py} \\ v_{pz} \end{bmatrix} t_{go}}{t_{go}^2} \tag{5.3.4}$$

We now have a vector notation for the earth fixed acceleration required to hit the target with a proportional gain term, $\vec{K}_p$. This acceleration can be mapped into the body fixed coordination, or more simply into the canard actuation system as a phase angle and an amplitude. The mapping is similar to section 5.2 with the angle defined by:

$$\phi_r = atan2(a_{py}, a_{px}) + \frac{\pi}{2}$$
$$\delta_c = \|\{a_{px}, a_{py}\}\| \tag{5.3.5}$$

5.4   Guidance Results Ideal Controller

In this section, the two separate guidance techniques will be compared, the Impact Point Prediction Method and the Modified Proportional Navigation Method with an ideal canard tracking system. The 6DOF projectile simulation with the initial conditions from Chapter 2 will be used for comparison for conformity. The GPS errors are assumed to be zero for this simulation. The unguided projectile, under nominal trajectory, would impact at $\approx \{4448, 29, 0\}m$. The unguided trajectory results of Chapter 2 will be used as a reference for the unguided case. As a measure of performance, the CEP of an unguided round is approximately 100+m, whereas the guided round must have a CEP of 10m. This implies 50% of the projectiles will land in a 10m radius. The canard regulator will be assumed ideal for this section, i.e. the regulator tracks the canard command angle perfectly.

5.4.1   Using Impact Point Prediction

The IPP based controller will begin guidance at 10 seconds into the flight. The reason for the delay is due to the assumption that the GPS might not acquire until this point and also to minimize the effect of impact point prediction error earlier on in the flight. Figures 5.3 and 5.4 show the results of the guidance controller on the trajectory. The target location is set at $\{X_t, Y_t, Z_t\} = \{6000, -200, 0\}$. The error in the final impact is 1.045 meters in down range impact and .701 meters in the cross range impact.

We can take a look at δ_c in Figure 5.5 and see the amount of burden on the controller is minimal as the angle stays below ± 6 degrees near the end of the flight. Figures 5.6 and 5.7 show impact point predictor will eventually converge on the target location as the flight progresses. The impact point prediction is plotted in in blue and
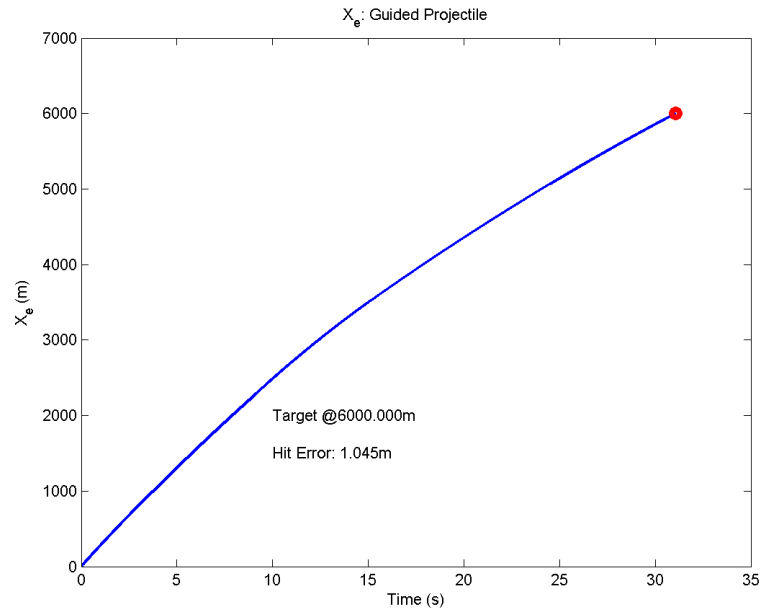
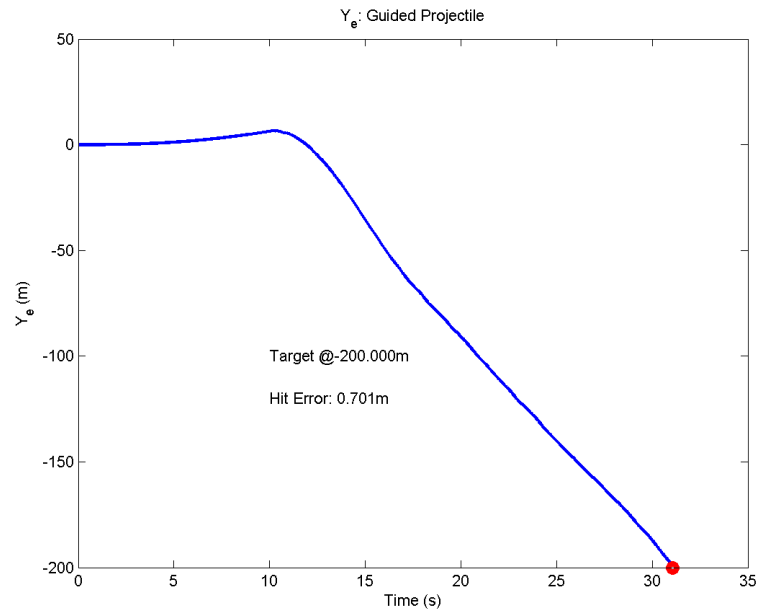Figure 5.3: Down Range Flight of Projectile (blue), Target Location (red)

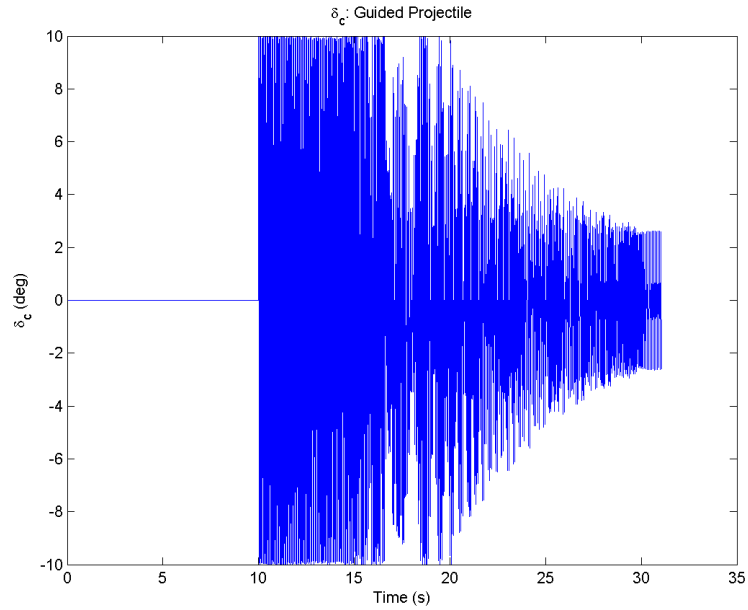Figure 5.4: Cross Range Flight of Projectile (blue), Target Location (red)

Figure 5.5: Canard Amplitude, δ_c

the target location in red. Figure 5.6 shows the down range impact point prediction vs. time. At approximately 10 seconds, the impact point error is acceptable for prediction of the down range impact point and will converge as guidance is initiated. The cross range impact point in Figure 5.6 shows the impact point prediction will oscillate continuously around the true impact point. This is due to the yawing motion of the projectile. The projectile's overall dynamics when guided will "low-pass" this effect and guide to the correct location. Figure 5.8 shows the impact point prediction as the flight progresses. The plot demonstrates how the IPP will converge in an oscillatory motion onto target. It has been shown that the impact point prediction method, though simplified provides sufficient results for the purpose of guidance with the ideal controller.
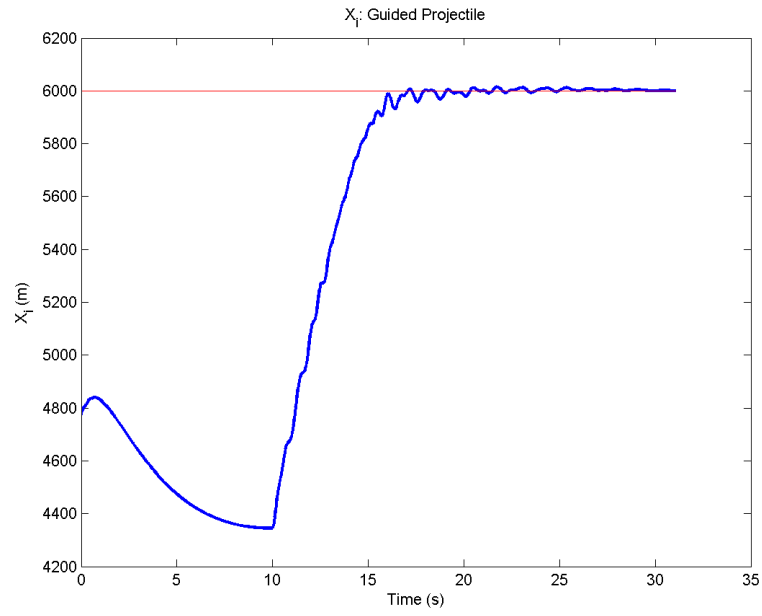
Figure 5.6: Down Range Impact Point Prediction (blue), True Impact Point (red)
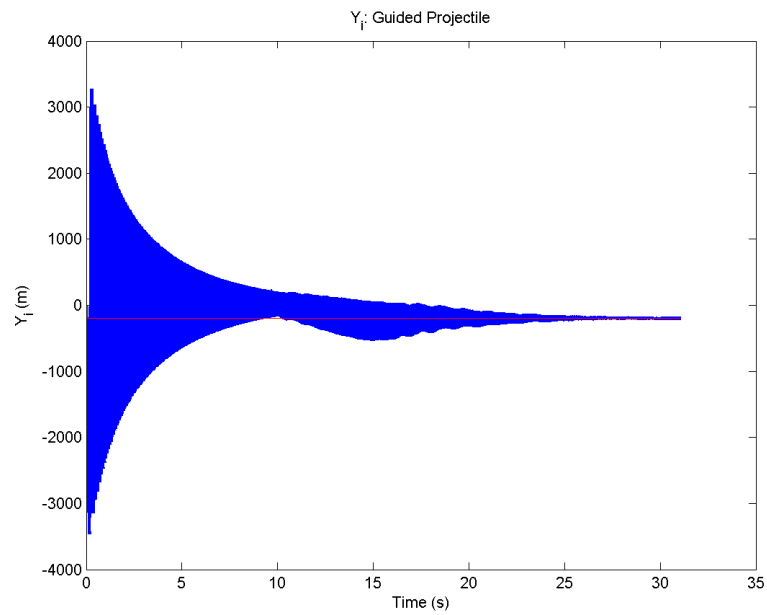

Figure 5.7: Cross Range Impact Point Prediction (blue), True Impact Point (red)
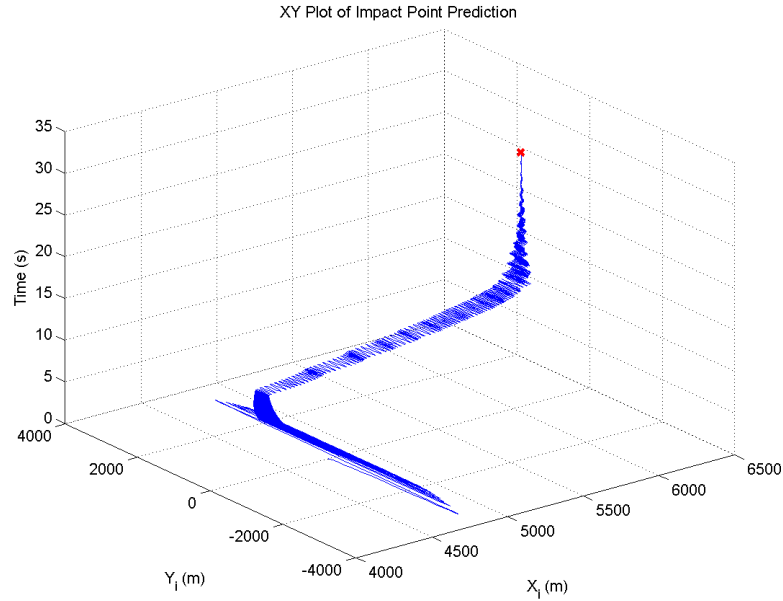
Figure 5.8: Cross Range Impact Point Prediction (blue), True Impact Point (red)

5.4.2 Using Modified Proportional Navigation Guidance

The proportional navigation controller will begin guidance once apogee is achieved. Again, this will assume the GPS has acquired and locked. Also, since the algorithm requires a flat fire trajectory model, the projectile must have hit apogee for proper time-to-go calculations.

Figures 5.9 and 5.10 show the results of the guidance controller on the trajectory. The target location is set at $\{X_t, Y_t, Z_t\} = \{6000, -200, 0\}$. The error in the final impact is 0.897 meters in down range impact and 0.099 meters in the cross range impact. Figure 5.9 shows that the system will guide well in down range towards the target. The cross range plot, Figure 5.10, shows the projectile will first begin navigating toward the left and then converge towards the solution. In comparison to the results of Figure 5.4, the projectile diverts more in the wrong direction in the
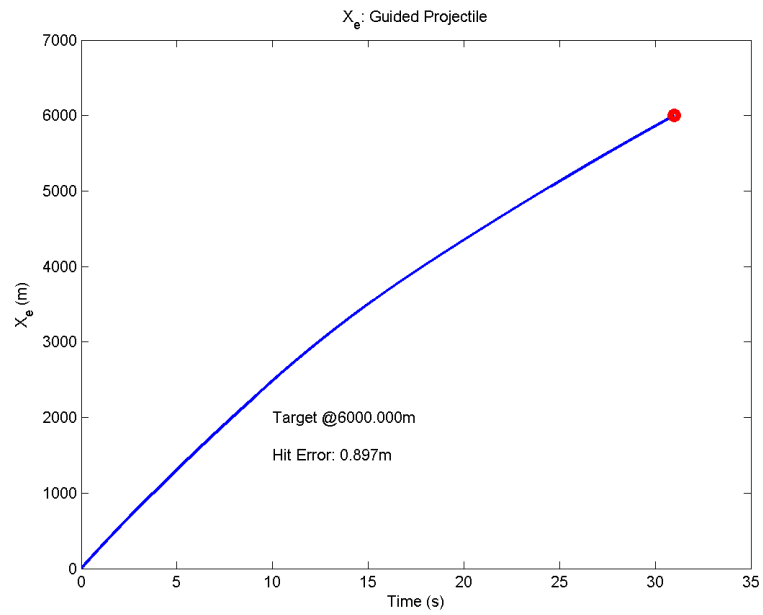
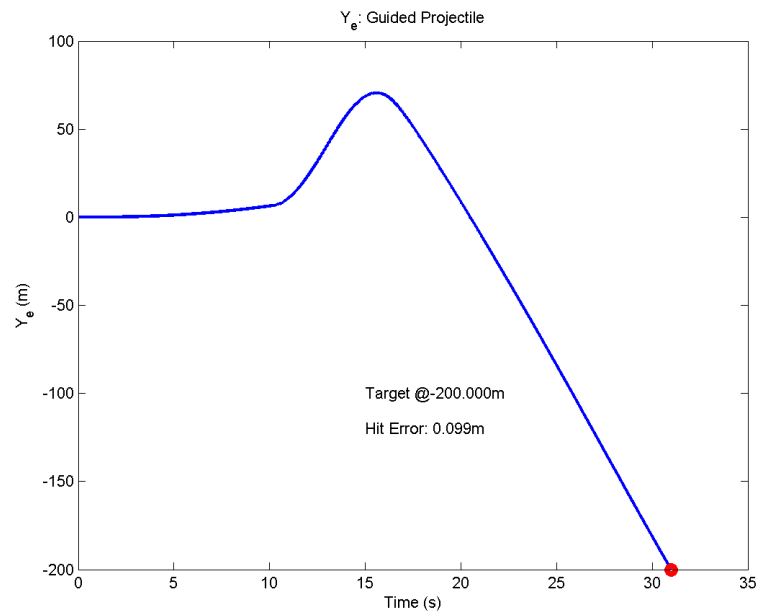Figure 5.9: Down Range Flight of Projectile (blue), Target Location (red)

Figure 5.10: Cross Range Flight of Projectile (blue), Target Location (red)
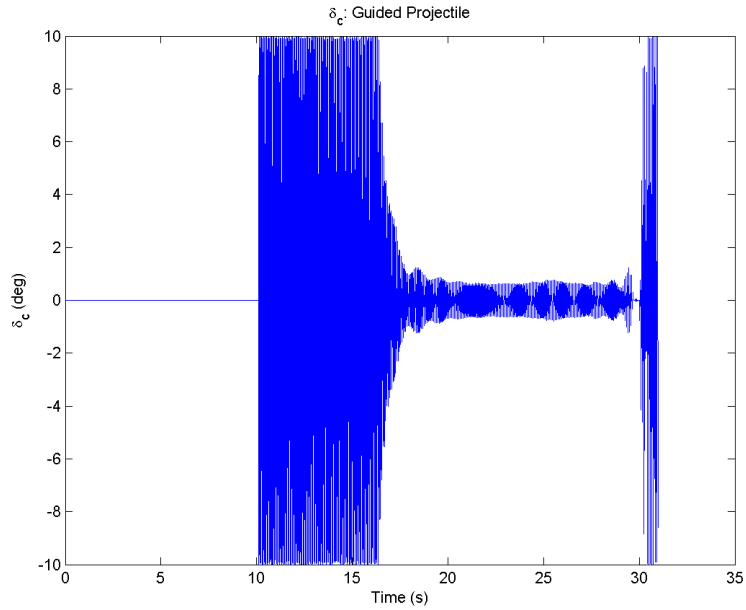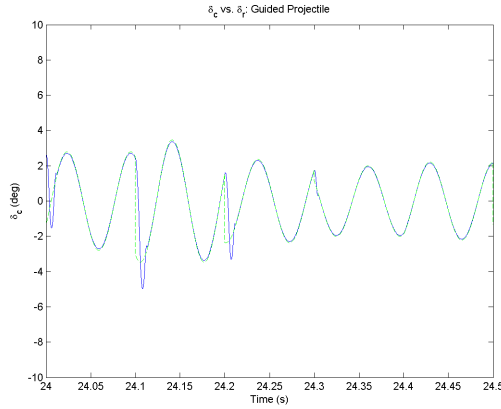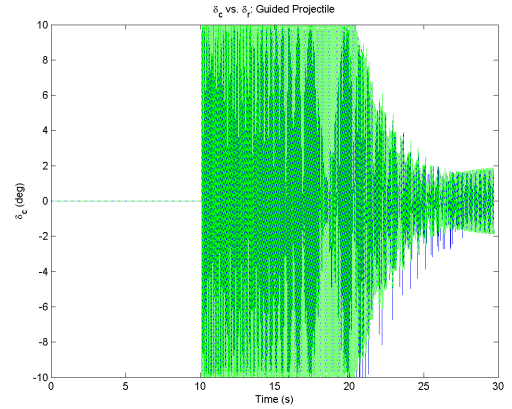
Figure 5.11: Canard Amplitude, δ_c

beginning. Figure 5.11 shows the canard displacement as the projectile flies. When the guidance first turns on at approximately 10 seconds, then the projectile begins to give larger acceleration commands which slowly damp out. The maneuvers become more aggressive closer to impact as one would expect. The conclusion can be made that both techniques are relatively good at hitting the target.

5.5   Guidance Results Multivariable Regulator Controller

Now, we will again run the simulation with the controller from Chapter 3 assuming that the state measurements for the attitude are ideal and correct. Again, the GPS errors are assumed zero and updated at 10Hz after 10 seconds into the flight. The target location will again remain at $\{X_t, Y_t, Z_t\} = \{6000, -200, 0\}$.

(a) Canard Amplitude, δ_r (blue), δ_c (green): Full Flight

(b) Canard Amplitude, δ_r (blue), δ_c (green): Zoomed In

Figure 5.12: Canard Response

5.5.1   Using Impact Point Prediction

Figure 5.12a shows the canard displacement as a function of time vs. the commanded canard displacement. The zoomed-in plot of Figure 5.12b shows how close the canard angle, δ_c, is to the commanded canard angle δ_c. The canard angle does not ideally track the guidance system commands, but this is expected. The instantaneous changes in displacement shown in Figure 5.12b are due to the GPS sampling and corresponding controller update rate. The instantaneous phase changes give rise to large spikes in error shown in Figure 5.13, which is a plot of the difference between the ideal phase and canard phase, $\delta_r - \delta_c$. Figure 5.14 shows the impact point prediction will eventually converge on cross range impact point and Figure 5.15 shows the convergence of the cross range impact point. These plots correlate nicely to the ideal controller case of Section 5.4.   The cross range and down range plots of the projectile vs. time are shown in Figures 5.16 and 5.17, respectively. The projectile falls short of the target by 15.135; an error most likely caused by added drag to early
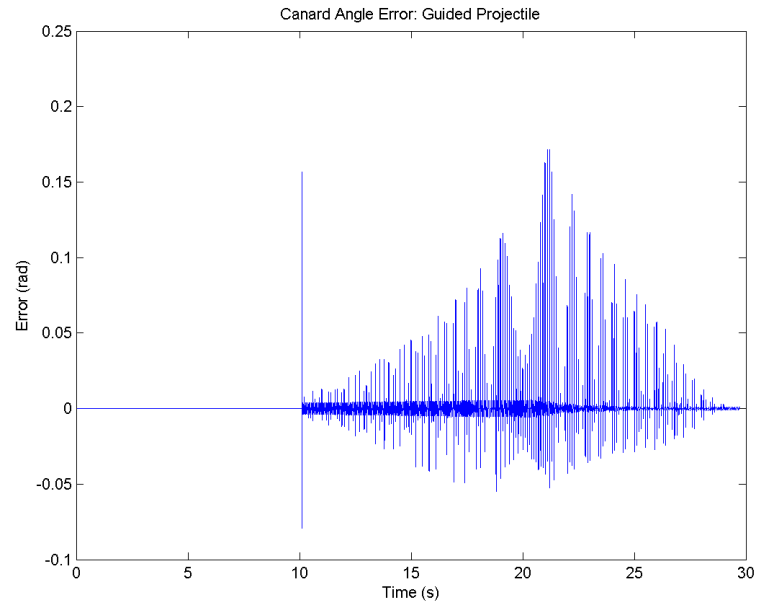
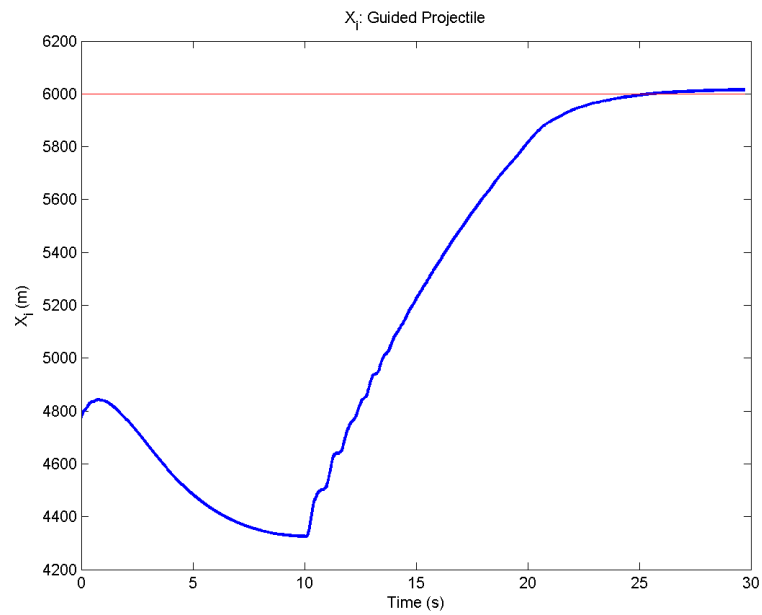Figure 5.13: Canard Error, $\delta_r - \delta_c$

Figure 5.14: Down Range Impact Point Prediction (blue), True Impact Point (red)
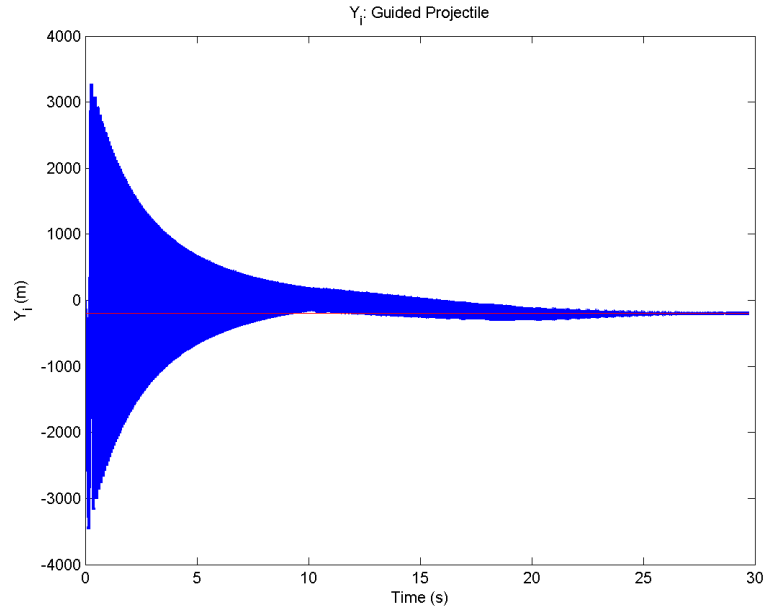
Figure 5.15: Cross Range Impact Point Prediction (blue), True Impact Point (red)

canard maneuvers. The cross range plot shows the projectile hits within .043m of the target cross range location. Though these errors are substantially larger than the ideal case of section 5.4, we can state with some confidence that the resultant CEP still outperforms an unguided round.

5.5.2 Using Modified Proportional Navigation Guidance

It is necessary to analyze the MPN guidance method to see how much of an impact the canard regulator would have on the target miss distance. First, the canard tracking error is analyzed to show how much the guidance law affects the regulator. Figure 5.18a shows the canard displacement as a function of time vs. the commanded canard displacement. The zoomed-in plot of Figure 5.18b shows how close the canard angle, δ_c, is to the commanded canard angle δ_c. Though it might seem like the canard angle perfectly tracks the command angle, there is some slight error. The small error is

Figure 5.16: Down Range Flight of Projectile (blue), Target Location (red)

Figure 5.17: Cross Range Flight of Projectile (blue), Target Location (red)
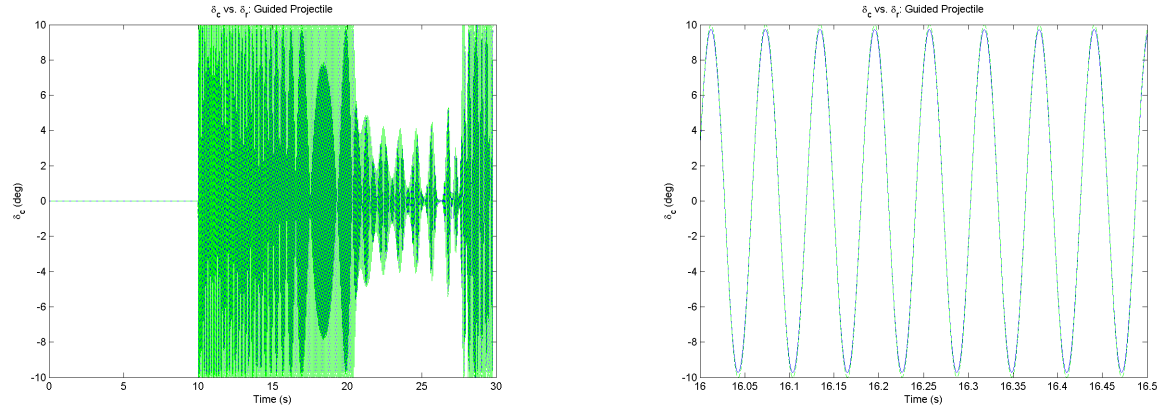
(a) Canard Amplitude, δ_r (blue), δ_c (green): Full Flight

(b) Canard Amplitude, δ_r (blue), δ_c (green): Zoomed In

Figure 5.18: Canard Response

shown in Figure 5.19. A comparison of Figure 5.19 to Figure 5.13 shows that the IPP Method has many more large phase angle changes, which are harder for the regulator to track. Therefore, even though an IPP will work well with the ideal system, when the regulator and body dynamics are added, the MPN method outperforms the IPP method. The small changes in angles are evident for the phase angle commands in Figure 5.20. As the controller turns on at 10 seconds into the flight, the phase angle is nearly 90 degrees until near impact. The 90 degree phase will give the body lift until close to the impact when the system will begin to narrow in on the target.

The results for the down range and cross range impacts for the target vs. time are shown in Figures 5.21 and 5.21. This demonstrates that the MPN method works better than the IPP method. The error for the impact is 0.43m for the down range and -1.26m for the cross range. Again, we can state with some confidence that the resultant CEP is a great improvement over an unguided round.

Using both methods, a simplified guidance law can be combined with the complex

Figure 5.19: Canard Error, $\delta_r - \delta_c$
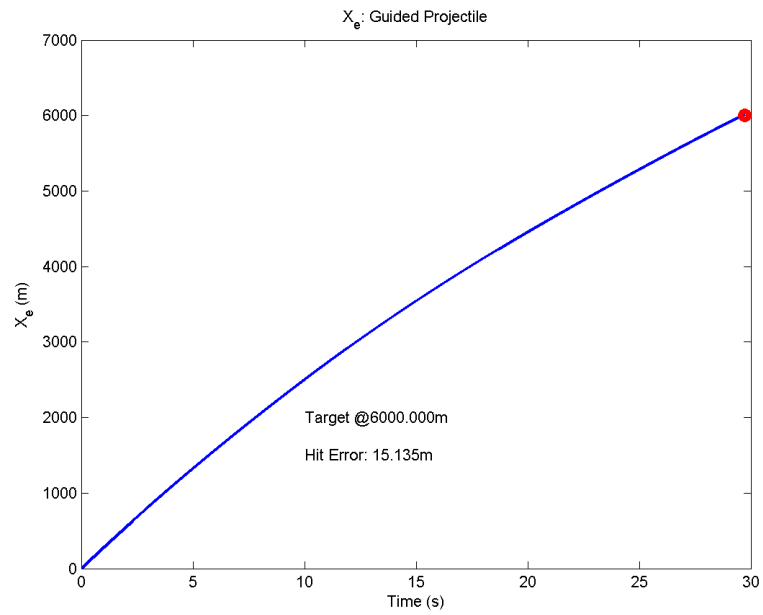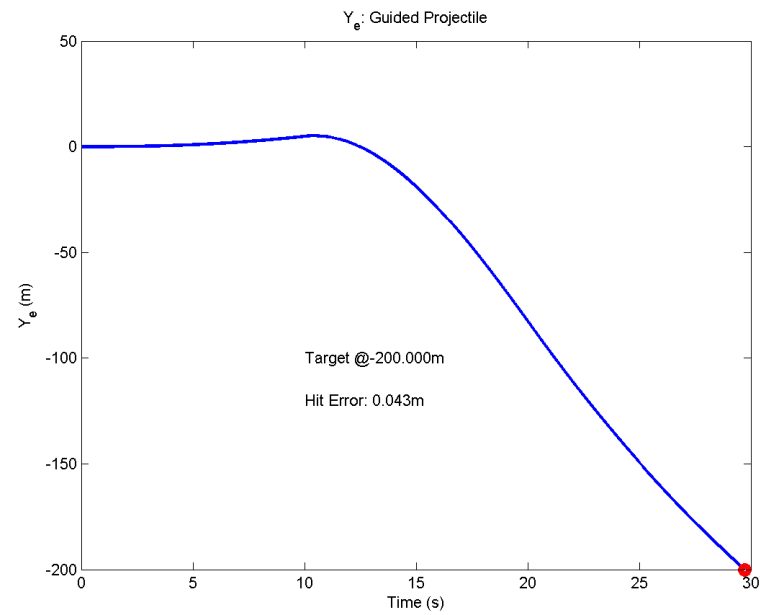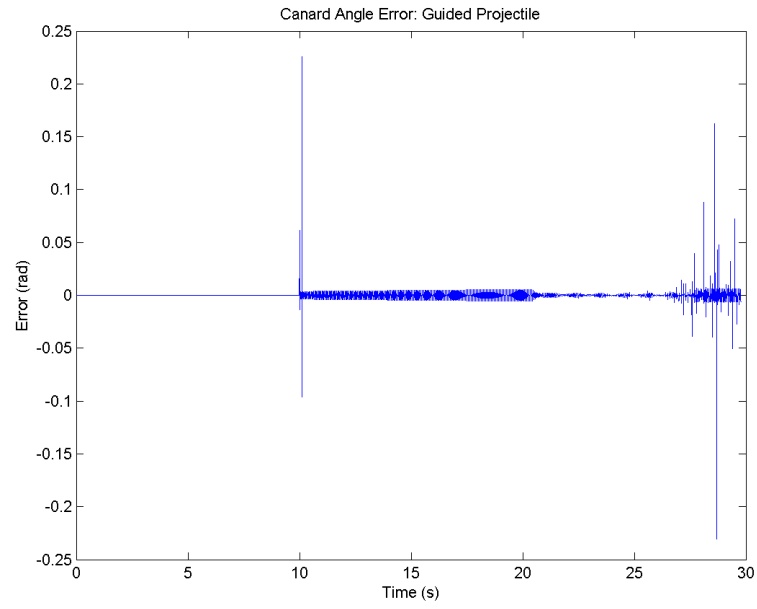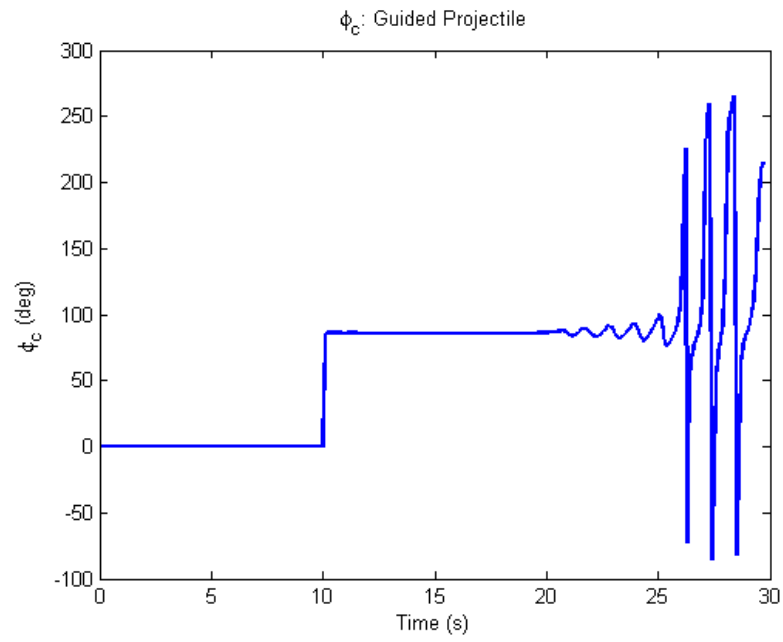

Figure 5.20: Canard Phase Angle, ϕ_c

Figure 5.21: Down Range Flight of Projectile (blue), Target Location (red)
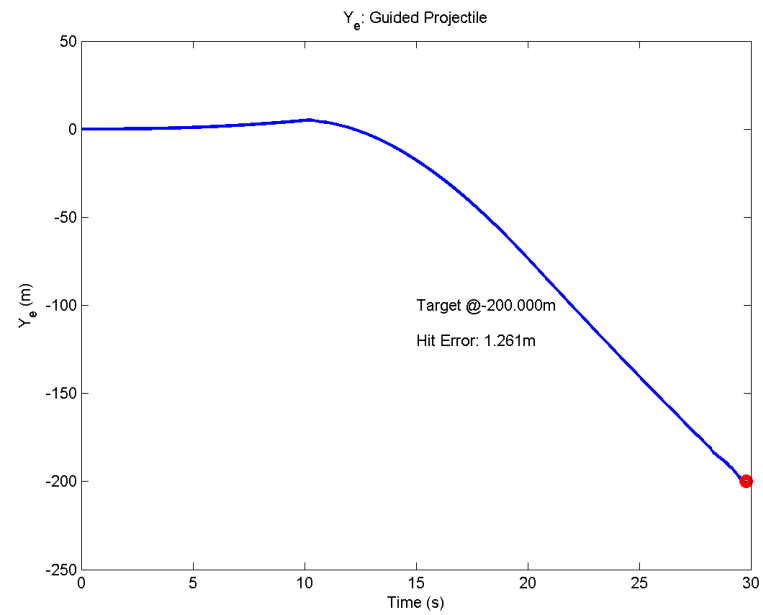
Figure 5.22: Cross Range Flight of Projectile (blue), Target Location (red)
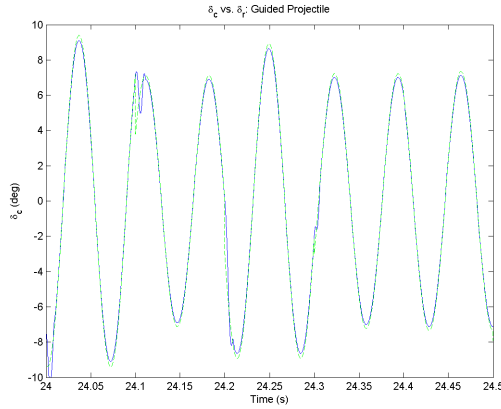
(a) Canard Amplitude, δ_r (blue), δ_c (green): Full Flight
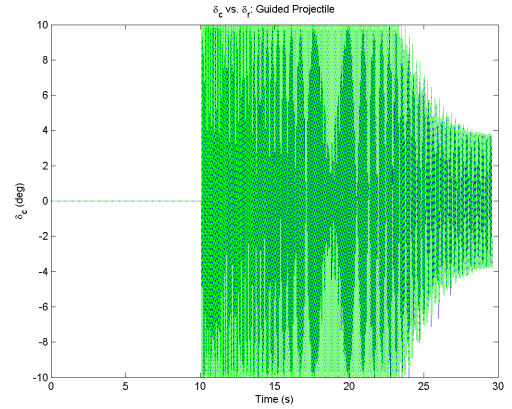
(b) Canard Amplitude, δ_r (blue), δ_c (green): Zoomed In

Figure 5.23: Canard Response

controller to drive the projectile to a target with minimal error.

5.6   Guidance Results Full System

Now that the system will accurately guide utilizing the regulator, we wish to know if the system will guide with the estimated attitude using the QEKF of Chapter 4. Another simulation of the same target for consistency will show the effect of the error of the state estimates and the controller can affect the performance of the guidance.

5.6.1   Using Impact Point Prediction

Using the IPP method, we will use the estimated states and the regulator to show how the system will perform to the same initial conditions as the previous simulations for uniformity. The GPS is updated at 10Hz and the guidance begins at 10s. Figures 5.23a and 5.23b show the instantaneous effect due to the IPP updating with GPS updates. With this simulation the regulators error is compounded by the state
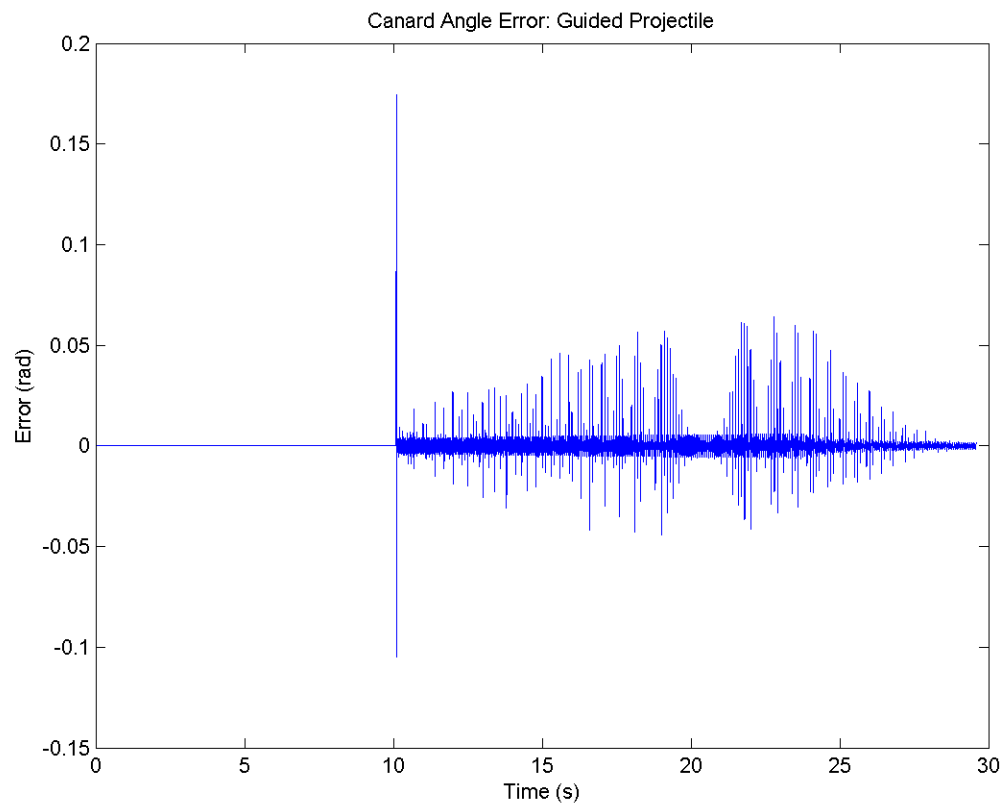
Figure 5.24: Canard Error, $\delta_r - \delta_c$
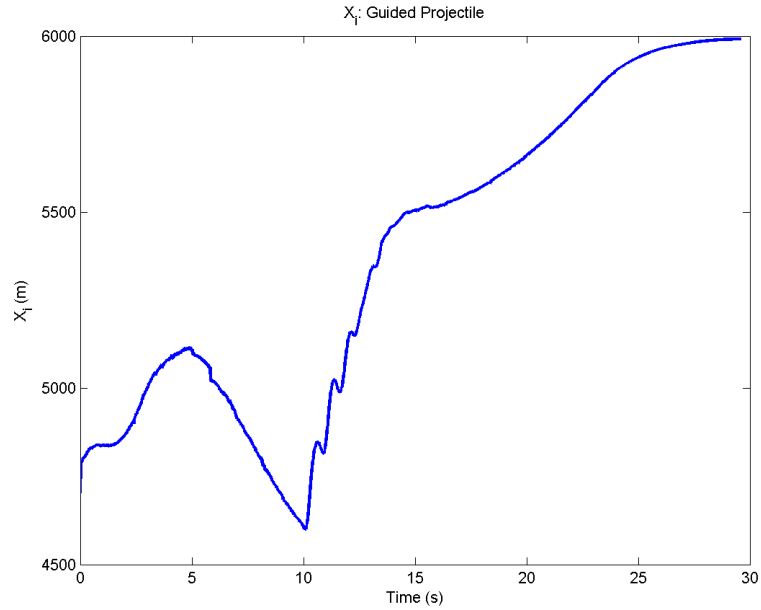
Figure 5.25: Down Range Impact Point Prediction (blue), True Impact Point (red)

estimate error and instantaneous phase shift updates. The impact point predictor, though it does converge, is not 100% effective. The IPP error could be attributed to drag associated with canard maneuvers and attitude estimates feeding into the IPP Equations 5.1.1. The impact point errors from Figures 5.25 and 5.26 propagate to the final impact of the projectile as a biased error. The error in the cross-range impact is shown in Figure 5.30. Figures 5.29 and 5.30 show that the system will hit the target with errors of $\{8.856, 49.308\}$. It has been shown that combining a simplified guidance law, the complex controller, and the QEKF state estimator, the system can be driven close to the target, but would probably be insufficient to justify the guidance system. It also should be noted that the case presented is extreme and there is a lot of burden on the controller and hence the impact point prediction may be off due to the added lift / drag of the canard system. Typically, the fire
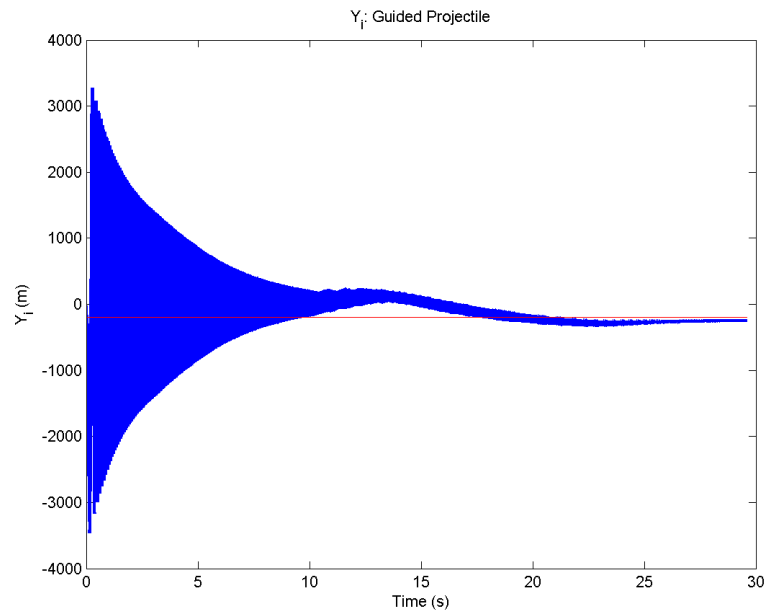
Figure 5.26: Cross Range Impact Point Prediction (blue), True Impact Point (red)
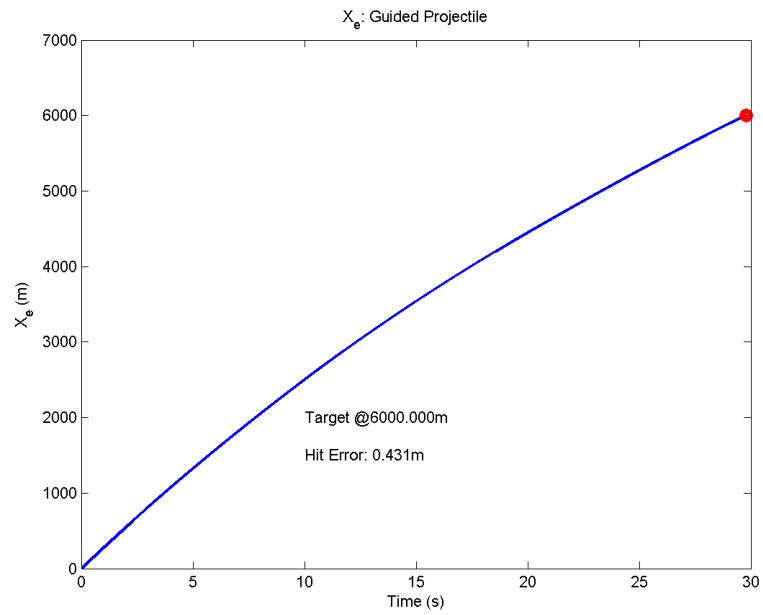

Figure 5.27: Down Range Flight of Projectile (blue), Target Location (red)
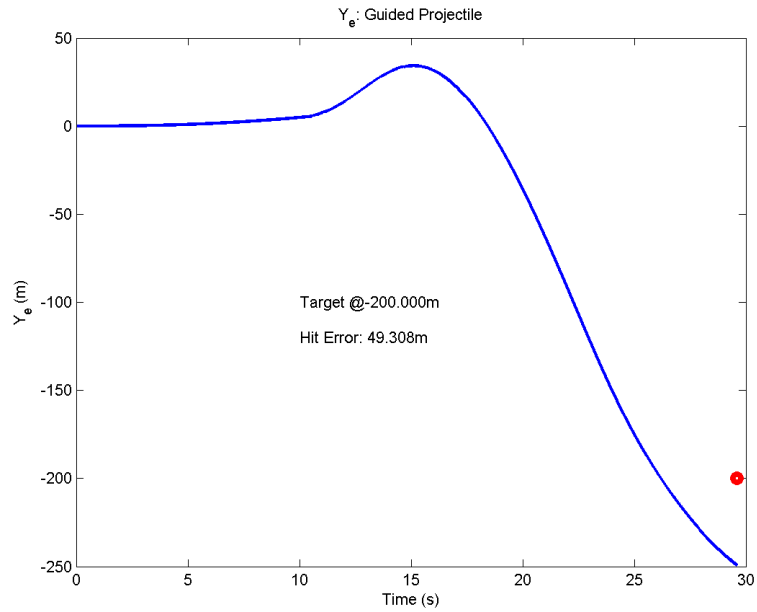
Figure 5.28: Cross Range Flight of Projectile (blue), Target Location (red)

control system will come up with a more practical trajectory which would require less maneuver authority. The error between the target and nominal impact point would most likely be bounded within the hundreds of meters and not thousands and thus the impact point prediction would maintain its accuracy. As an example, we will pick a target that is closer to the ballistic trajectory, $\{4600, 10\}$

The trajectory down range and cross range plots are shown in Figures 5.29 and 5.30. The figures show that with the new target location, the projectile can hit the target with an error of $\{7.318, 1.392\}$. This error is much smaller than the previous simulation, but there is room for improvement.

5.6.2 Using Modified Proportional Navigation Guidance

The previous section shows to hit the target with accuracy and confidence, a simulation of the entire system is necessary. To show the effect of estimation errors on

Figure 5.29: Down Range Flight of Projectile (blue), Target Location (red)
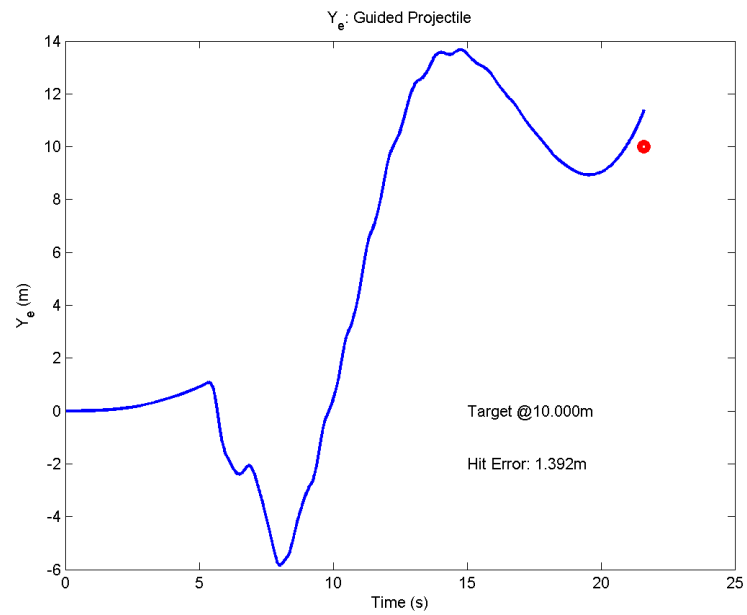
Figure 5.30: Cross Range Flight of Projectile (blue), Target Location (red)

(a) Canard Amplitude, δ_r (blue), δ_c (green): Full Flight

(b) Canard Amplitude, δ_r (blue), δ_c (green): Zoomed In

Figure 5.31: Canard Response

the MPN method of guidance, a simulation similar to the previous section 5.6.1 is performed using the initial conditions. The GPS updates at 10Hz and the guidance begins at 10s.

We will first look at the regulator output to ensure that the canard is tracking the commanded signals correctly. Figures 5.31a and 5.31b show the canard angle vs. time. The plots show the guidance controller requires the canard to actuate for a good portion of the flight and how well the regulator tracks the commanded signal in the zoomed in portion of Figure 5.31b. The canard error is plotted in Figure 5.32, showing that the the canard will track very well throughout the flight and the error is minimal. Figures 5.33 and 5.37 show that the system will hit the target with errors of $\{-0.744321, -0.140927\}$. The combination of the MPN guidance law, the regulator, and the QEKF state estimator, accurately guides the projectile to the target.

Figure 5.35 shows the projectile's effective maneuver to the target from and overhead view (cross range vs. down range). The overhead view provides insight to the
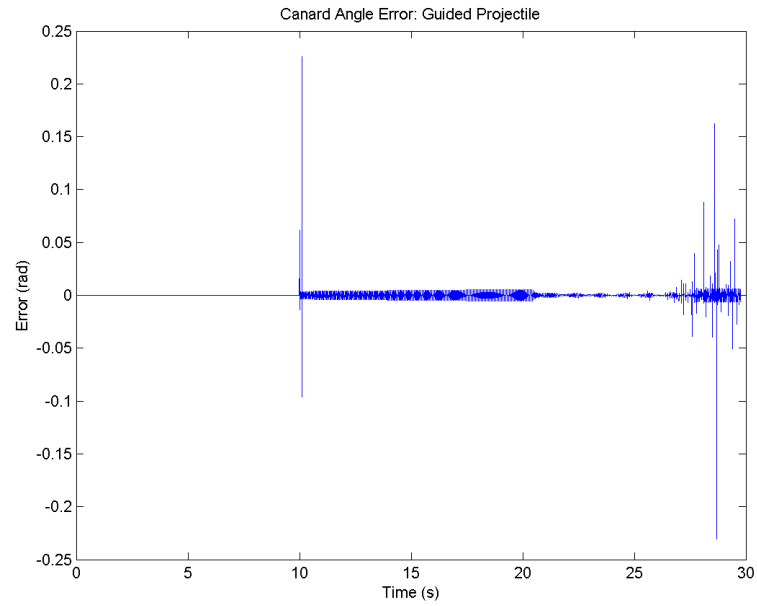
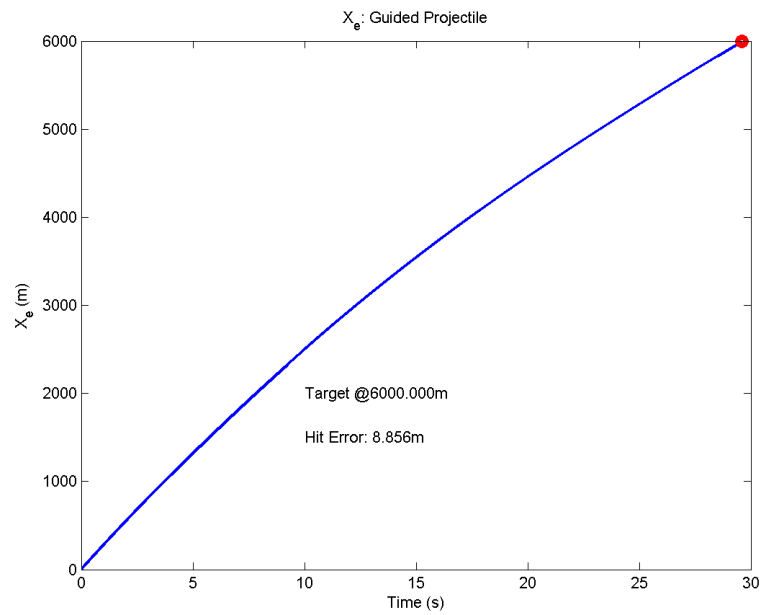Figure 5.32: Canard Error, $\delta_r - \delta_c$
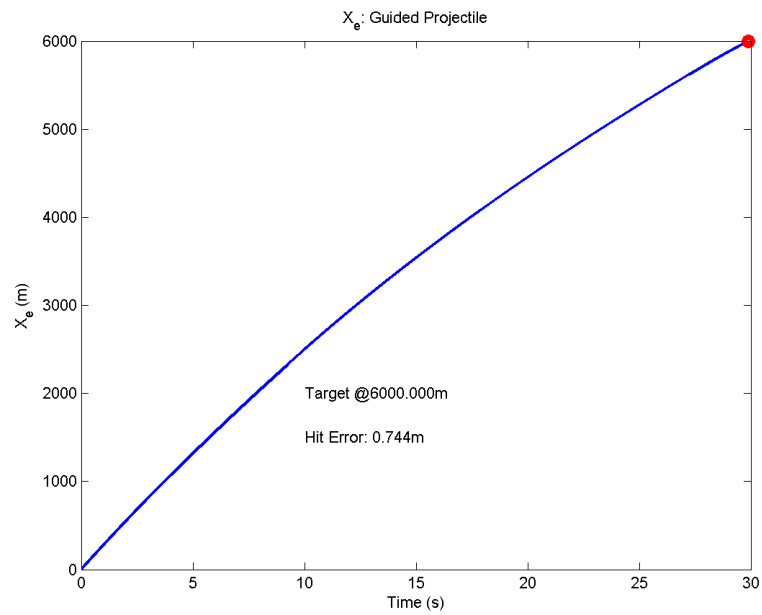
Figure 5.33: Down Range Flight of Projectile (blue), Target Location (red)
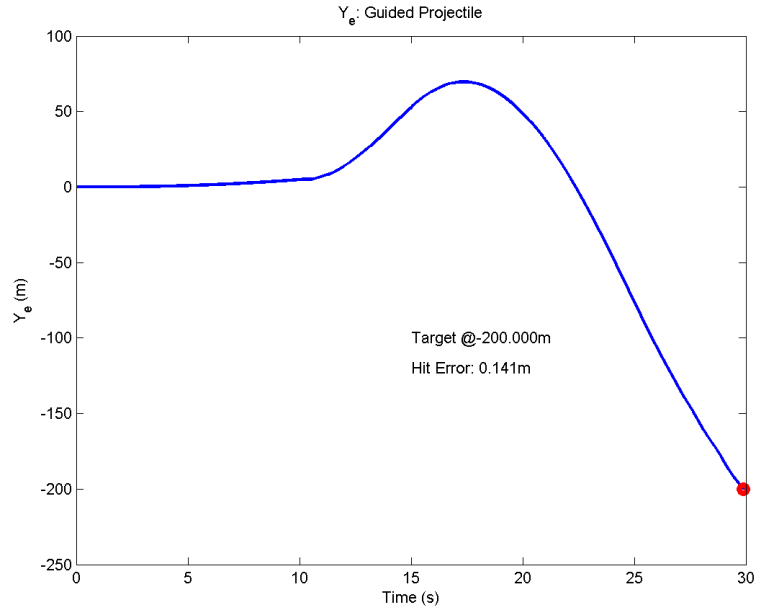
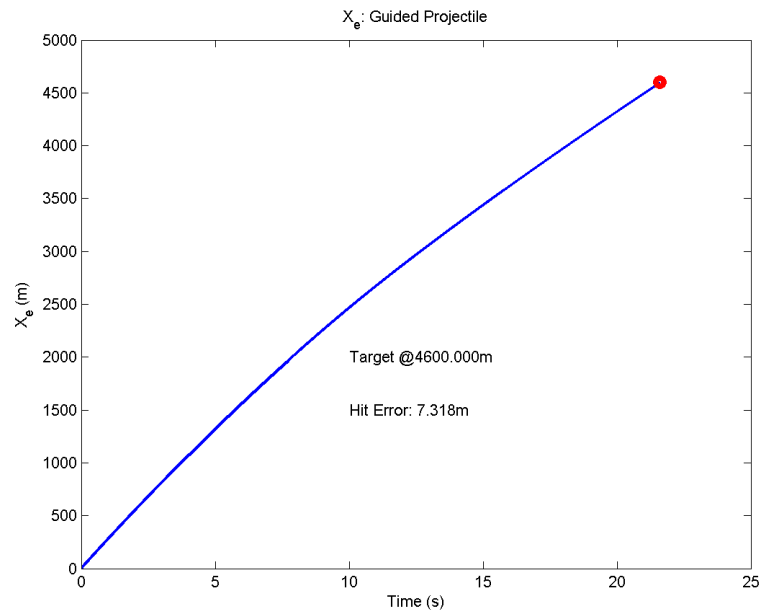Figure 5.34: Cross Range Flight of Projectile (blue), Target Location (red)

proportional law. Earlier in the guidance, the projectile puts a higher demand on the down-range location which causes the projectile to slightly drift to the left. This effect is also shown in Figure 5.36 which shows the canard phase angle command throughout flight. In the commanded phase plot, the phase is close to $\frac{pi}{2}$. and slight errors about this location will cause the side motion as seen in the open loop divert tests. The projectile guidance will eventually correct for this error in the cross range. As in previous cases with this guidance law, the projectile performs aggressive maneuvers close to impact. This can be explained by the high gain associated with $t_{go} \rightarrow 0$ term in Equation (5.3.4). The lift portion of the flight can also be seen in the altitude plot of the projectile as it flies through the air, shown in Figure 5.37. This section shows how a simple MPN guidance law out performs the IPP method when coupled with the regulator and the attitude estimate of the QEKF. The target has been hit with
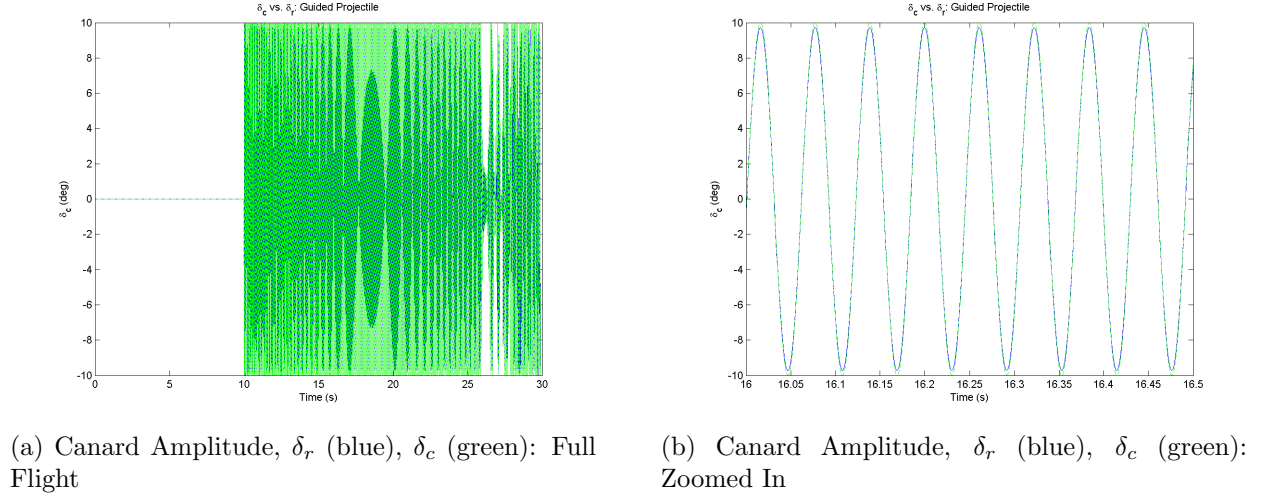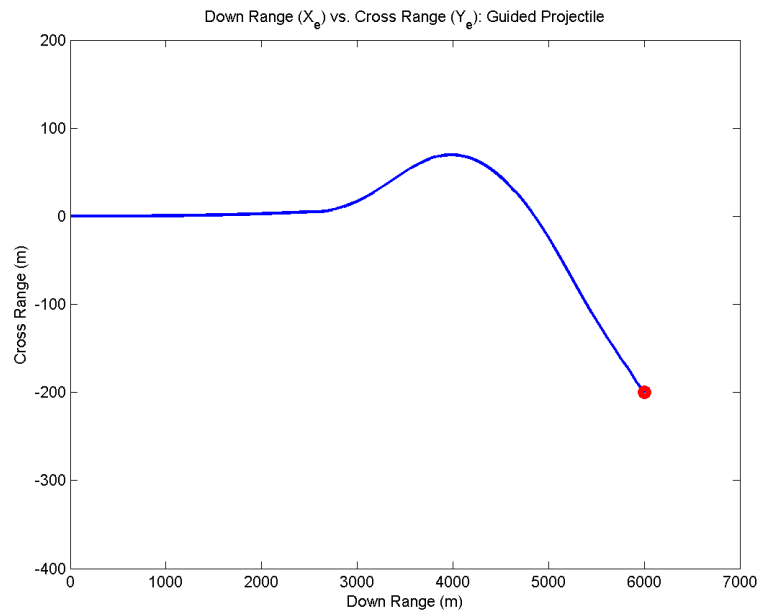
Figure 5.35: Flight of Projectile (blue), Target Location (red)
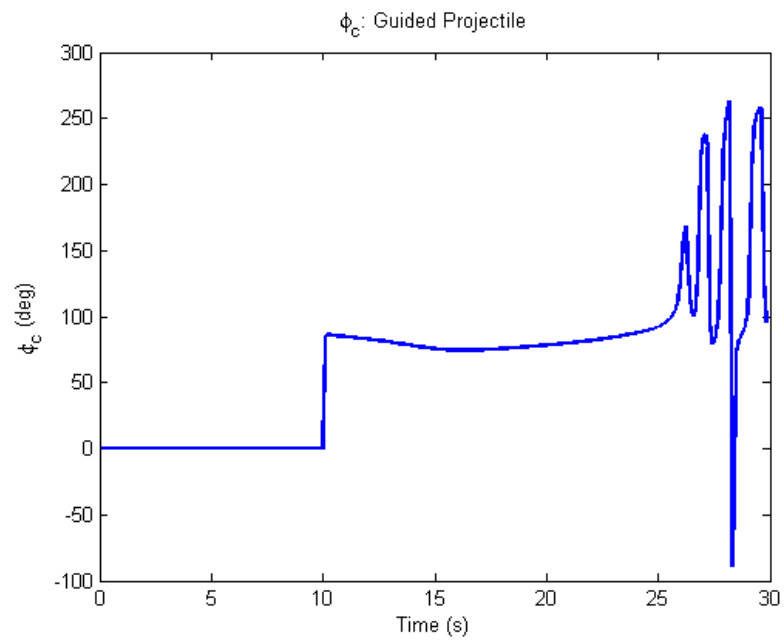
Figure 5.36: Canard Error, $\delta_r - \delta_c$
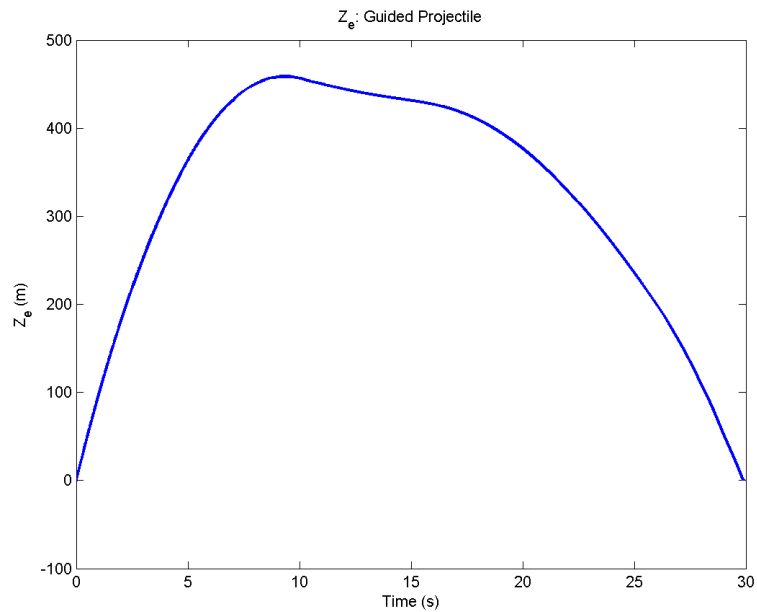
Figure 5.37: Cross Range Flight of Projectile (blue), Target Location (red)

minimal error and we can conclude that the CEP would be dramatically improved.

5.7 Effective Range Area of MPN

Since the MPN has been shown to impact the target in all three cases, we would like to know the effective controller range for the projectile. Since the full system behaves similarly to the ideal case for the MPN, we will simulate several runs, moving the target at each run. The target will vary from 3km to 10km in down range and -3km to 3km in the cross range. Figure 5.38 shows a plot of the effective range of the projectile when fired with the initial conditions used through

The color bar on the right of Figure 5.38 shows the guidance controller effective range. The region is bounded by 3km, 7.8km down range and -2.8km,2.8km cross range. These limits are caused by a combination of the guidance controller,
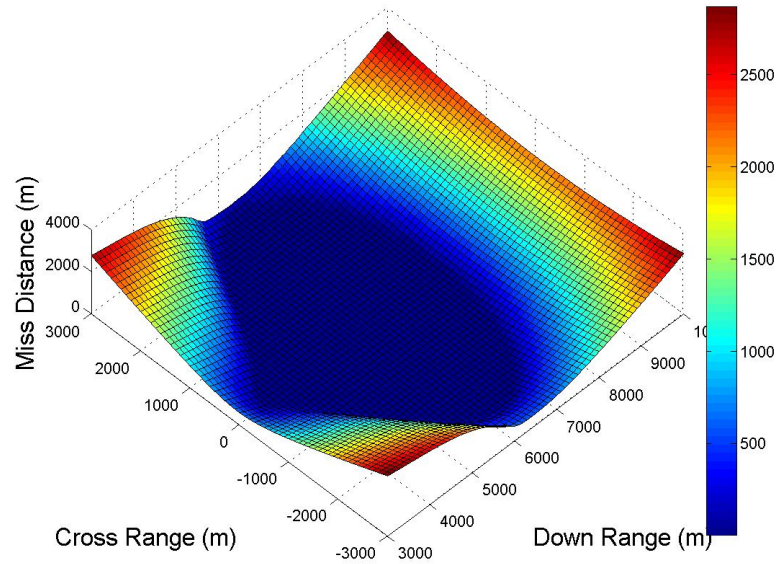
Figure 5.38: Effective Range of the Projectile

the available canard forces, and the projectile aerodynamics. Figure 5.39 shows the relationship between the effective range and the original ballistic impact point. The ballistic impact point is shown as a Red X at ≈ 4.5km down range and ≈ 30m cross range. The area highlighted in Green are the regions where the target miss distance is less than 10m.

In conclusion, the guided projectile has a much larger effective range and is more accurate than a ballistic projectile. The above plots only relate to one set of initial conditions and only represent range improvements over the ballistic trajectory.
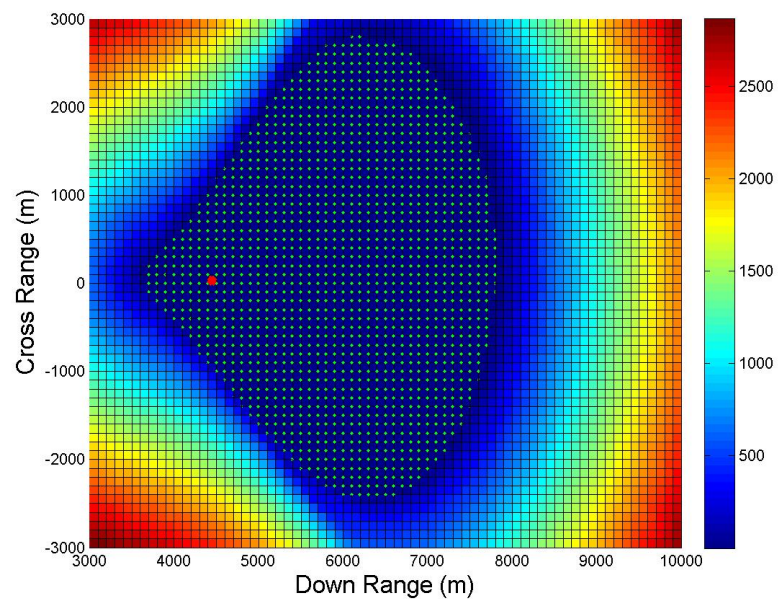
Figure 5.39: Effective Range of the Projectile Overhead View with Target

Chapter 6: Conclusion and Future Work

6.1 Conclusions

In this thesis, an innovative canard control system design approach has been developed for gun-launched spinning flying munitions to compute an optimal flight path, control the canard position to maneuver the flight, and eventually hit the target. A new single-axis canard assembly was built and installed in the fuse located at the front end of the projectile, and the multivariable regulator and H_2 control theory has been successfully employed to accurately control the canard movement and therefore the flight of the projectile regardless of the difficulties caused by the persistent spin and the lack of propulsion thrust.

The persistent spin issue is resolved by oscillating canards according to the spin rate of the projectile. The phase of the oscillation is controlled to reflect the desire deflection angle of the canards, which determines the heading direction of the projectile. The solution involves the construction of a flight dynamics model for the projectile with the proposed canard assembly, the design and implementation of the multivariable regulator and H_2 controller, and the attitude estimation using magnetometers, rate gyros, quaternions, and extended Kalman filtering. Due to the lack of propulsion thrust, the guidance and control law for projectiles is required to be more sophisticated and robust.

The aerodynamics equations presented in Chapter 2 explain how the canard system interacts with the body of the projectile. In the case of missile or airplane, the

equations of motion can be simplified and linearized around nominal states, whereas with the spinning projectiles, these simplifications cannot be made due to the complex aerodynamic behavior. The aerodynamics is crucial in determining the effect of the canards on the projectile flight path and in understanding how the nonlinear torques on the canard actuator will pose design constraints. The aerodynamics model is used in the computer flight simulation of the projectile, and in a hardware-in-the-loop system to test and evaluate the tracking regulator with the canard actuation systems hardware.

In Chapter 3, it has been made clear that by oscillating the canards in a sinusoidal motion, with a phase offset from projectiles roll angle, a net force can be imparted on the body of the projectile. The tracking regulator has demonstrated that by using the proposed control system, the single-axis canard actuation can be used to move the projectile in any direction on the y-z plane of the projectile. Implementation of the regulator and H_2 controller in a Hardware-in-the-Loop experiment has shown that not only was the method theoretically feasible, but that the system can be realized experimentally on a digital processor in a realistic environment.

Traditional methods of state estimation rely costly on inertial measurement units and linearized equations of motion, but in a spinning projectile, these traditional methods will not work. In this thesis, it has been proposed a method of estimating the attitude of the projectile through the use of extended Kalman filtering that utilizes the quaternions rather than the Euler angles in the state vector. This method is more promising because the quaternion is computationally more efficient and impervious to asymptotic divergence. The results of Chapter 4 show how the extended Kalman filtering based on quaternions is both effective and robust.

To engage the target, two guidance laws were compared, Impact Point Prediction and Modified Proportional Navigation. The comparison showed that even though the IPP will work in an ideal situation with perfect canard tracking and no state estimation errors, the method will not work in realistic situations that are not ideal. This thesis shows that by using basic kinematic equations and properly accounting for the lack of propulsion thrust, the MPN method performs better guidance even in the presence of error from both the state estimations and the regulator tracking.

6.2 Future Work

All the work presented in this thesis relies on some fundamental assumptions for a projectile system. These assumptions include rate sensors that do not have bias drift and the canard system will perform under the aerodynamic loading properly. In order to improve on the design, bias estimation techniques should be studied to ensure the QEKF will not diverge with rate sensor drift. Several techniques exist to estimate the angular orientation using magnetometers, [53, 24, 23, 22]. These techniques could be used to estimate the bias of the rate sensors, but we must ensure that the bias drift is observable. There are many papers on this topic, and investigation further would be necessary to conclude that the aforementioned techniques would be sufficient for all cases. To verify that the QEKF will work in practice, I plan to implement the QEKF on a DSP and integrate into a HIL test and follow up with a flight test. The multivariable regulator controller will be verified in an upcoming wind tunnel test to ensure the controller works under aerodynamic load.

The guidance laws proposed in this thesis are not robust, so in practice, it may be necessary to develop more modern control techniques to the guidance problem. The

ideal guidance law would minimize the control effort from the projectile and improve the accuracy over the current design. We would also like to add constraints on the guidance system such as angle of fall or terminal impact velocities, which could be accomplished with modern control methods.

Another topic that warrants more discussion is GPS. The assumption was made in this thesis that there are no GPS errors, where in reality, the GPS will have error in the position and velocity measurements. Future research should include methods for resolving the position and velocity of the projectile in the presence of these GPS errors. A possible method to minimize the estimation error due to GPS errors is to use Differential GPS or inertial measurement techniques to aid in the observations.

Appendix A: Alternative Equations of Motion

A.1   No Roll (Fixed Plane)

The derivation of these equations are based on the 6DOF model of Chapter 2 and have been simplified using the no-roll plane of motion as the body reference frame. Therefore, when computing the equations of motion, the roll angle $\phi = 0$. The roll rate, $\dot{\phi}_{fp}$ is maintained in the euler angle equations.

$$
\begin{aligned}
\begin{bmatrix} \dot{u}_{fp} \\ \dot{v}_{fp} \\ \dot{w}_{fp} \end{bmatrix} &= \frac{1}{m} \begin{bmatrix} F_{fpx} \\ F_{fpy} \\ F_{fpz} \end{bmatrix} + \begin{bmatrix} 0 & -r_{fp} & q_{fp} \\ r_{fp} & 0 & -p_{fp} \\ -q_{fp} & p_{fp} & 0 \end{bmatrix} \begin{bmatrix} u_{fp} \\ v_{fp} \\ w_{fp} \end{bmatrix} \\[2mm]
\begin{bmatrix} \dot{p}_{fp} \\ \dot{q}_{fp} \\ \dot{r}_{fp} \end{bmatrix} &= \begin{bmatrix} \frac{L_{fp}}{I_{xx}} \\ \frac{M_{fp}}{I_{yy}} - \frac{I_{xx}}{I_{yy}} p_{fp} r_{fp} + r_{fp}^2 t_\theta \\ \frac{N_{fp}}{I_{yy}} + \frac{I_{xx}}{I_{yy}} p_{fp} q_{fp} + q_{fp} r_{fp} t_\theta \end{bmatrix} \\[2mm]
\begin{bmatrix} \dot{\phi}_{fp} \\ \dot{\theta}_{fp} \\ \dot{\psi}_{fp} \end{bmatrix} &= \begin{bmatrix} 1 & 0 & t_{\theta_{fp}} \\ 0 & 1 & 0 \\ 0 & 0 & \frac{1}{c_{\theta_{fp}}} \end{bmatrix} \\[2mm]
\begin{bmatrix} \dot{X}_{fpe} \\ \dot{Y}_{fpe} \\ \dot{Z}_{fpe} \end{bmatrix} &= \lambda_{\psi\theta\phi}^{-1} \Big|_{\phi=0} \begin{bmatrix} u_{fp} \\ v_{fp} \\ w_{fp} \end{bmatrix}
\end{aligned}
\tag{A.1.1}
$$

A.2 Quaternion Equations of Motion

The equations below represent the state equations for a quaternion based 6DOF projectile.

$$
\begin{bmatrix} \dot{u} \\ \dot{v} \\ \dot{w} \end{bmatrix} = \frac{1}{m} \begin{bmatrix} F_x \\ F_y \\ F_z \end{bmatrix} - \begin{bmatrix} 0 & -r & q \\ r & 0 & -p \\ -q & p & 0 \end{bmatrix} \begin{bmatrix} u \\ v \\ w \end{bmatrix} \tag{A.2.1}
$$

$$
\begin{bmatrix} \dot{p} \\ \dot{q} \\ \dot{r} \end{bmatrix} = \begin{bmatrix} \frac{L}{I_{xx}} \\ \frac{M}{I_{yy}} + (I_{xx} - I_{yy})\, pr \\ \frac{N}{I_{yy}} + (I_{yy} - I_{xx})\, pq \end{bmatrix} \tag{A.2.2}
$$

$$
\dot{\mathbf{q}} = \Omega \mathbf{q}
$$

$$
\Omega = \begin{bmatrix} 0 & -p & -q & -r \\ p & 0 & r & -q \\ q & -r & 0 & p \\ r & q & -p & 0 \end{bmatrix} \tag{A.2.3}
$$

$$
\begin{bmatrix} \dot{X}_e \\ \dot{Y}_e \\ \dot{Z}_e \end{bmatrix} = R\,(\mathbf{q})^{-1} \begin{bmatrix} u \\ v \\ w \end{bmatrix} \quad R = \begin{bmatrix} q_0^2 + q_1^2 - q_2^2 - q_3^2 & 2(q_1 q_2 - q_0 q_3) & 2(q_1 q_3 - 2q_0 q_2) \\ 2(q_1 q_2 + q_0 q_3) & q_0^2 + q_2^2 - q_1^2 - q_3^2 & 2(q_2 q_3 - q_0 q_1) \\ 2(q_1 q_3 - 2q_0 q_2) & 2(q_2 q_3 + q_0 q_1) & q_0^2 + q_3^2 - q_1^2 - q_2^2 \end{bmatrix} \tag{A.2.4}
$$

Appendix B: Simplified Magnetometer Roll Rate Calculations

The following equations assume the magnetometer measurement are in Gauss and are obtained from a calibrated magnetometer. From chapter 2 equation, 2.1.9, shows the relationship of the DCM to the magnetic field of the Earth B.0.1.

$$
\begin{bmatrix} M_i \\ M_j \\ M_k \end{bmatrix} = \lambda_{\psi\theta\phi} \begin{bmatrix} M_N \\ M_E \\ M_N \end{bmatrix}
\tag{B.0.1}
$$

Where the M_i, M_j, M_k are the body fixed measurements of the magnetic field and M_N, M_N, M_D is the local magnetic field in the NED coordinate system. The expression for M_j and M_k can be grouped in terms of c_ϕ and s_ϕ:

$$
\begin{aligned}
M_j &= c_\theta M_D s_\phi + M_N(c_\psi s_\theta s_\phi - c_\phi s_\psi) + M_E(c_\phi c_\psi + s_\theta s_\phi s_\psi) \\
&= s_\phi \left(c_\theta M_D + c_\psi s_\theta M_N + s_\theta s_\psi M_E \right) + c_\phi \left(-s_\psi M_N + c_\psi M_E \right) \\
&= As_\phi + Bc_\phi \\
M_k &= c_\theta c_\phi M_D + M_E(-c_\psi s_\phi + c_\phi s_\theta s_\psi) + M_N(c_\phi c_\psi s_\theta + s_\phi s_\psi) \\
&= s_\phi \left(s_\psi M_N - c_\psi M_E \right) c_\phi \left(c_\theta M_D + c_\psi s_\theta M_N + s_\theta s_\psi M_E \right) \\
&= -Bs_\phi + Ac_\phi
\end{aligned}
\tag{B.0.2}
$$

Combining the expressions:

$$
\begin{bmatrix} M_j \\ M_k \end{bmatrix} = \begin{bmatrix} A & B \\ -B & A \end{bmatrix} \begin{bmatrix} s_\phi \\ c_\phi \end{bmatrix} \rightarrow \begin{bmatrix} s_\phi \\ c_\phi \end{bmatrix} = \begin{bmatrix} A & B \\ -B & A \end{bmatrix}^{-1} \begin{bmatrix} M_j \\ M_k \end{bmatrix}
\tag{B.0.3}
$$

And making the assumption that $\psi \approx 0$ and $M_E \approx 0$ then $B = 0$ and solving for ϕ:

$$
\begin{bmatrix} s_\phi \\ c_\phi \end{bmatrix} = \begin{bmatrix} A & 0 \\ 0 & A \end{bmatrix}^{-1} \begin{bmatrix} M_j \\ M_k \end{bmatrix} = \begin{bmatrix} A^{-1} & 0 \\ 0 & A^{-1} \end{bmatrix} \begin{bmatrix} M_j \\ M_k \end{bmatrix} \rightarrow t_\phi = \frac{s_\phi}{c_\phi} = \frac{M_j}{M_k}
\tag{B.0.4}
$$

Appendix C: Acronyms

Acronym	Description
6DOF	Six Degree-Of-Freedom
ADC	Analog-to-Digital Converter
AIAA	American Institute of Aeronautics and Astronautics
AMR	Amnisotropic MagnetoResistive
AOA	Angle Of Attack
ARL	Army Research Laboratory
AWGN	Additive White Gaussian Noise
CEP	Circular Error Probable
CFD	Computational Fluid Dynamics
CG	Center of Gravity
COTS	Commercial-Off-The-Shelf
CP	Center of Pressure
DAC	Digital-to-Analog Converter
DCM	Direction Cosine Matrix
DSP	Digital Signal Processor
EKF	Extended Kalman Filter
GN&C	Guidance Navigation & Control
GPS	Global Positioning System
HIL	Hardware-In-the-Loop
IEEE	Institude of Electrical and Electronics Engineers
IMU	Inertial Measurement Unit

Acronym	Description
IPP	Impact Point Prediction
JDAM	Joint Direct Attack Muntion
MEMS	Micro-Electro-Mechancalical Systems
MPN	Modified Proportional Navigation
N4SID	Numerical Algorithms for Subspace State Space System Identification
NED	North East Down
PC	Personal Computer
PCB	Printed Circuit Board
PEM	Prediction Error Method
PGK	Precision Guidance Kit
PGMM	Precision Guided Mortar Munition
PWM	Pulse Width Modulation
QE	Quadrant Elevation
QEKF	Quaternion Extended Kalman Filter
SAL	Semi-Active Laser
YPR	Yaw-Pitch-Roll
ZOH	Zero-Order-Hold

Appendix D: Notations

Variable	Description
λ	Euler Angle Direction Cosine Matrix
$R(\mathbf{q})$	Quaternion Direction Cosine Matrix
$\{\psi, \theta, \phi\}$	Euler Yaw, Pitch, and Roll Angles
$\vec{\omega}$	Body Fixed Angular Rate Vector
$\{p, q, r\}$	Body Fixed Angular Rate Components
$\{X_e, Y_e, Z_e\}$	Projectile Coordinates in Earth Coordinates
$\{X_t, Y_t, Z_t\}$	Target Position in Earth Coordinates
$\{V_{xe}, V_{ye}, V_{ze}\}$	Projectile Velocities in Earth Coordinates
$\vec{V}$	Body Fixed Velocity Vector
$\{u, v, w\}$	Body Fixed Velocity Vector Components
α	Angle of Attack
β	Sideslip Angle
M_a	Mach Number
$\vec{F}_{xyz}$	Force Vector in Body x,y,z Directions
$\vec{M}_{ypr}$	Moment Vector About Yaw-Pitch-Roll Axis
δ_c	Deflection Angle of the Canard
a_r	Canard Tracking Signal Amplitude
ω_r	Canard Tracking Signal Frequency
ϕ_r	Canard Tracking Signal Phase
ϕ_i	Ideal Tracking Signal Phase
$\mathbf{q}$	Quaternion

Bibliography

[1] R. Azor, I.Y. Bar-Itzhack, and R.R. Harman. Satellite angular rate estimation from vector measurements. *Journal of Guidance, Control, and Dynamics*, 21, No 3:450–457, 1998.

[2] I.Y. Bar-Itzhack and Y. Oshman. Attitude determination from vector observations: Quaternion estimation. *IEEE Transactions on Aerospace and Electronic Systems*, AES-21, No 1:128–136, 1985.

[3] J. Bradley. Equations of motion - a prelude to r1216. Technical report, US Ballistics Research Laboratory, December 1992.

[4] I. Celmins. Design and evaluation of an electromechanical actuator for projectile guidance: Arl-mr-0672. Technical report, US Army Research Laboratory, September 2007.

[5] B.C. Chang and C. Hu. Multivariable control and failure accommodation in eye-head-torso target tracking. *Proceedings of the 42nd IEEE Conference on Decision and Control*, pages 981–983, 2003.

[6] B.C. Chang, C. Hu, and M. Ilg. Design and dsp microprocessor implementation of digital sinusoidal tracking controllers. *Proceedings of the 2005 American Control Conference*, 7:4947– 4952, 2005.

[7] D. Choukroun, H. Weiss, I.Y. Bar-Itzhack, and Y. Oshman. Direction cosine matrix estimation from vector observations using a matrix kalman filter. *AIAA Guidance, Navigation, and Control Conference and Exhibit*, 2003.

[8] M. Costello, G. Cooper, J. Powell, C. Hummer, and P. Plostins. Initial projectile state estimation with the use of magnetometers in a spatially varying magnetic field: Arl-tr-4245. Technical report, US Army Research Laboratory, September 2007.

[9] J.L. Crassidis and F.L. Markley. Predictive filtering for attitude estimation without rate sensors. *Journal of Guidance, Control, and Dynamics*, 20, No 3:522–527, 1997.

[10] J.L. Crassidis, F.L. Markley, and Y. Cheng. Survey of nonlinear attitude estimation methods. *Journal of Guidance, Control, and Dynamics*, 30, No 1:12–28, 2007.

[11] B. Davis, R. Hall, T. Harkins, M. Wilson, B. Patton, M. Nair, and M. Ilg. Integral telemetry module development and demonstration on the precision-guided mortar munition: Arl-tr-4151. Technical report, US Army Research Laboratory, June 2007.

[12] B. Davis, T. Harkins, D. Hepner, B. Patton, and R. Hall. Aeroballistic diagnostic fuze (dfuze) measurements for projectile development, test, and evaluation: Arl-tr-3204. Technical report, US Army Research Laboratory, July 2004.

[13] B. Davis, W. Hathaway, A. Hathaway, and A. Thompson. Extending telemetry reduction to aerodynamic coefficients and trajectory reconstruction (extractr): Arl-tr-3563. Technical report, US Army Research Laboratory, August 2005.

[14] B. Davis and K. McMullen. Development and demonstration of a g-hardened inertial sensor suite and mortar diagnostic fuze: Arl-tr-2918. Technical report, US Army Research Laboratory, March 2003.

[15] P.M. DeRusso, R.J. Roy, C.M. Close, and A.A. Desrochers. *State Variables for Engineers*. Wiley-Interscience, 1998.

[16] J.K. Deutschmann and I.Y. Bar-Itzhack. Evaluation of attitude and orbit estimation using actual earth magnetic field data. *Journal of Guidance, Control, and Dynamics*, 24, No 3:616–623, 2001.

[17] J.C. Doyle, K. Glover, P.P. Khargohekar, and B.A. Francis. State-space solutions to standard h-2 and h-infinity control problems. *IEEE Transactions on Automatic Control*, AC-34, No 8:930–933, 1989.

[18] B. Etkin and L.D. Reid. *Dynamics of Flight: Stability and Control.* John Wiley and Sons, 1996.

[19] B. Friedland. *Advanced Control System Design.* Prentice-Hall, 1996.

[20] D. Gebre-Egziabher, G.H. Elkaim, J.D. Powell, and B.W. Parkinson. A gyro-free quaternion-based attitude determination system suitable for implementation using low cost sensors. *IEEE Position Location and Navigation Symposium*, pages 185–192, 2000.

[21] M.S. Grewal and A.P. Andrews. *Kalman Filtering: Theory and Practice Using MATLAB.* John Wiley and Sons, 2001.

[22] T. Harkins. A unique solution for flight body angular histories : Arl-tr-4315. Technical report, US Army Research Laboratory, November 2007.

[23] T. Harkins and M. Wilson. On the viability of magnetometer-based projectile orientation measurements : Arl-tr-4310. Technical report, US Army Research Laboratory, November 2007.

[24] T. Harkins and M. Wilson. Measuring in-flight angular motion with a low-cost magnetometer : Arl-tr-4244. Technical report, US Army Research Laboratory, September 2007.

[25] D. Hepner and T. Harkins. Determining inertial orientation of a spinning body with body-fixed sensors: Arl-tr-2313. Technical report, US Army Research Laboratory, January 2001.

[26] D. Hepner, M. Hollis, and C. Mitchel. Yawsonde technology for the jet propulsion laboratory (jpl) free flying magnetometer (ffm) program: Arl-tr-1610. Technical report, US Army Research Laboratory, July 1998.

[27] S.M. Hill and T.J. McCusker. Real-time optimal attitude estimation using horizon sensor and magnetometer data. *Journal of Spacecraft and Rockets*, 35, No 6:778–784, 1998.

[28] L. C. Hainz III and M. Costello. Linear theory of a dual-spin projectile in atmospheric flight. *Journal of Guidance, Control, and Dynamics, volume=23, No 5, year=2000, pages=789-797,*.

[29] L. C. Hainz III and M. Costello. Modified projectile linear theory for rapid trajectory prediction. *Journal of Guidance, Control, and Dynamics, volume=28, No 5, year=2005, pages=1006-1014,*.

[30] L. C. Hainz III and M. Costello. In flight projectile impact point prediction. *AIAA Atmospheric Flight Mechanics Conference and Exhibit*, AIAA-2004-4711, 2004.

[31] M. Ilg, B. C. Chang, D. Hepner, and A. Thompson. A microcontroller solution for amr magnetic sensing in flying munitions systems. *Proceeding of the 2005 IEEE International Conference on Mechatronics*, July 10-12,2005.

[32] J.B. Kuipers. *Quaternions and Rotation Sequences: A Primer with Applications to Orbits, Aerospace, and Vircual Reality*. Princeton University Press, 1999.

[33] H.G. Kwatney and K.C. Kalnitsky. On alternative methodologies for the design of robust linear multivariable regulators. *IEEE Transactions on Automatic Control*, AC-23, No 5:930–933, 1978.

[34] D.C. Lay. *Linear Algebra and Its Applications*. Addison Wesley Longman, 1998.

[35] T. Lee, A. Sanyal, M. Leok, and N.H. McClamroch. Deterministic global attitude estimation. *Proceedings of the 45th IEEE Conference on Decision and Control*, pages 3174–3179, 2006.

[36] J.L. Marins, X. Yun, E.R. Bachmann, R.B. McGhee, and M.J. Zyda. An extended kalman filter for quaternion-based orientation estimation using marg sensors. *Proceedings of the 2001 IEEE/RSJ International Conference on Intelligent Robots and Systems*, pages 2003–2011, 2001.

[37] F.L Markley, J.L. Crassidis, and Y. Cheng. Nonlinear attitude filtering methods. *AIAA Guidance, Navigation, and Control Conference and Exhibit*, 2005.

[38] R.L. McCoy. *Modern Exterior Ballistics: The Launch and Flight Dynamics of Symmetric Projectiles*. Shiffer Publishing Ltd., 1999.

[39] C. Murphy. Free flight motion of symmetric missiles : Brl-r1216. Technical report, US Ballistics Research Laboratory, July 1963.

[40] A. Papoulis and S.U. Pillai. *Probability, Random Variables and Stochastic Processes*. McGraw-Hill, 2002.

[41] M.L. Psiaki. Global magnetometer-based spacecraft attitude and rate estimation. *Journal of Guidance, Control, and Dynamics*, 27, No 2:2003–2011, 2004.

[42] D. Simon. *Optimal State Estimation: Kalman, H-Infinity, and Nonlinear Approaches*. Wiley-Interscience, 2006.

[43] J.E. Slotine and W. Li. *Applied Non-Linear Control*. Prentice-Hall, 1991.

[44] A.A. Thompson. A proceedure for calibrating magnetic sensors : Arl-mr-524. Technical report, US Army Research Laboratory, January 2002.

[45] A.A. Thompson. A point-wise solution for the magnetic field vector: Arl-tr-2633. Technical report, US Army Research Laboratory, July 2002.

[46] S. T. Thorton and J. B. Marion. *Classical Dynamics of Particles and Systems.* Thomson Brooks/Cole, 2004.

[47] P. Tortora and Y. Oshman. Spacecraft angular rate estimation from magnetometer data only. *AIAA/AAS Astrodynamics Specialist Conference*, pages 304–310, 2000.

[48] H. Weinberg. Modifying the range of the adxrs150 and adxrs300 rate gyros: An-625. Technical report, Analog Devices, 2003.

[49] H. Weiss. Quaternion based rate/attitude tracking system with application to gimbal attitude control. *Proceedings. ICCON '89. IEEE International Conference on Control and Applications*, pages 240–250, 1989.

[50] M. Wilson, R. Hall, and M. Ilg. Onbord (on-board navigation of ballistic ordnance) gun-launched munitions flight controller: Arl-tr-3210. Technical report, US Army Research Laboratory, August 2004.

[51] M. Wilson, P. Peregino II, M. Ilg, and R. Hall. Ogive-borne navigation and telemetry system (obnav) atk's precision guidance kit (pgk) tests 400 and 405: Arl-tr-4226. Technical report, US Army Research Laboratory, August 2007.

[52] M. Wilson, M. Ilg, P. Peregino II, and R. Hall. Ogive-borne navigation and telemetry system (obnav): Arl-tr-3914. Technical report, US Army Research Laboratory, September 2006.

[53] M.J. Wilson. *Projectile Navigation and the Application to Magnetometers.* PhD thesis, University of Deleware, 2007.

[54] M.J. Wilson and A.S. Laroche. Automatic three-axis magnetometer calibration : Arl-tr-3557. Technical report, US Army Research Laboratory, July 2005.

[55] R.D. Yates and D.J. Goodman. *Probability and Stochastic Processes.* John Wiley and Sons, 1999.

[56] K. Zhou and J.C. Doyle. *Essentials of Robust Control.* Prentice-Hall, 1998.

[57] K. Zhou, J.C. Doyle, and K. Glover. *Robust and Optimal Control.* Prentice-Hall, 1996.